
Electronic Thesis and Dissertation Repository

6-30-2022 10:30 AM

Damage in Non-Crimp Fabric carbon fiber reinforced epoxy composites under various mechanical loading conditions

Aaditya Pradeep Suratkar, *The University of Western Ontario*

Supervisor: Wood, Jeff, *The University of Western Ontario*

Co-Supervisor: Montesano, John, *University of Waterloo*

A thesis submitted in partial fulfillment of the requirements for the Doctor of Philosophy degree in Mechanical and Materials Engineering

© Aaditya Pradeep Suratkar 2022

Follow this and additional works at: <https://ir.lib.uwo.ca/etd>



Part of the [Other Materials Science and Engineering Commons](#)

Recommended Citation

Suratkar, Aaditya Pradeep, "Damage in Non-Crimp Fabric carbon fiber reinforced epoxy composites under various mechanical loading conditions" (2022). *Electronic Thesis and Dissertation Repository*. 8731. <https://ir.lib.uwo.ca/etd/8731>

This Dissertation/Thesis is brought to you for free and open access by Scholarship@Western. It has been accepted for inclusion in Electronic Thesis and Dissertation Repository by an authorized administrator of Scholarship@Western. For more information, please contact wlsadmin@uwo.ca.

Abstract

Composite materials have emerged in the recent years as a frontrunning lightweight replacement for metals for structural applications in lightweight automobiles. However, the key adoption criteria for composites in lightweight vehicles is their crashworthiness, i.e., the amount of energy a structure made with composites would absorb in a crash event. The energy is absorbed in composites through various damage modes such as matrix cracks, delamination, fiber breakage, etc. Therefore, adoption of a certain composite material system requires thorough understanding of the initiation and propagation of damage until failure in that system under various mechanical loading conditions, which is also the central theme of this study.

The response of Non-Crimp Fabric (NCF) carbon fiber reinforced epoxy composites under quasi-static mechanical loads was thoroughly investigated in this study. The behavior of unidirectional lamina and multidirectional laminates was characterized in this study. The engineering properties and interlaminar fracture toughness of the lamina and the laminates are first measured using standard test methods. An in-situ damage monitoring technique called as 'edge replication' and post-failure fractography were employed to understand the damage initiation and growth in the materials under quasi-static tension and compression. The role of stitching sites, which are the compliant areas formed due to stitching threads in the NCF architecture, in the initiation of damage was clearly investigated in this study. The damage generally initiated in the form of localized cracks in the stitching sites at low strains, which then nucleated other damage modes in the laminates at higher strains. It was concluded that, although the stacking sequence had negligible influence on the global stress-strain response under tension, the rates and extents of damage were strongly dependent on the stacking sequence. The compression response, measured engineering properties and the observed damage modes showed higher sensitivity to the laminate stacking sequence. Finally, the damage observed in the composites was correlated to the energy dissipated in the creation of damage in this study.

Keywords

Continuous fiber reinforced polymer composites

Non-crimp fabric composites

Carbon fiber reinforced epoxy

Damage

Quasi-static mechanical characterization

Damage evolution

Energy-based approach

Summary for Lay Audience

Non-Crimp Fabric (NCF) composites have emerged as a new class of composite materials in the recent years which combine the advantages of unidirectional prepreg and woven textile materials. They are made by stacking several unidirectional fabrics, made by stitching the fibers together, on each other and impregnating them with the resin material. These materials have limited out-of-plane folding, or crimp, in their architecture, which translates into superior in-plane mechanical properties (like prepreg materials), and are easier to handle (like woven textile materials). The key distinguishing features of NCF composites are the relatively weaker resin-rich zones created due to the stitching fibers pushing two adjacent fibers apart locally and the local fiber misalignment induced by it. The damage behavior, from initiation until failure, in the NCF carbon fiber reinforced epoxy composites under quasi-static tension and compression was thoroughly investigated in this study using in-situ damage monitoring technique called ‘edge replication’ and post-failure microscopic observations.

Damage initiation was found in the form of cracks in the stitching sites in the tested laminates under both, tension and compression. This damage was then found to nucleate other forms of damage such as ply cracks and delamination at higher loads. The rates of multiplication and extents of the distinct damage mechanisms depended on the laminate stacking sequence, geometric factors such as ply thickness and loading conditions. While the influence of stacking sequence on the measured engineering properties was minimal under tensile loads, it had a significant effect on the damage evolution process. For example, higher rates of crack multiplication were observed in the weak transverse plies, which were constrained by adjacent stiff plies. The final failure under tension was, however, governed by the failure of the load-bearing fibers, aligned along the loading direction. Under compression, on the other hand, the effect of laminate stacking sequence was more pronounced on both, the engineering properties and the damage evolution process. The failure of laminates under compression was instantaneous and a combination of different damage mechanisms. Finally, upon connection to energy dissipation, delamination was found to be the most critical damage mechanism under both tension and compression, absorbing maximum energy in its creation.

Acknowledgments

I would like to begin the acknowledgements section by expressing my sincerest gratitude to my supervisors, Dr. Jeffrey Wood and Dr. John Montesano, for providing me with this opportunity to work in this industrially driven project of a collaborative nature. I would also like to thank them for their support, constructive feedback and patience over the last few years.

I thank Honda R&D Americas, Zoltek, Hexion, Laval International, Fraunhofer Project Center at Western University (FPC@Western) and Natural Sciences and Engineering Research Council (NSERC) for their technical and financial support over the last four years.

I would also like to thank Dr. Ying Fan for all her help during the last few years, particularly for all the equipment trainings and guidance in my first year as a PhD student. I would also like to acknowledge the support from Mr. Mesfin Gebreyes, who always went out of his way to make sure I got the facilities and resources I required to finish my experiments on time. Majority of the experiments in this study would have not been possible without the assistance from members of University Machine Services (UMS), especially Mr. Christopher van de Laar at the start, Mr. Clayton Cook through second and third years of my study and Dr. Duane Jacques towards the end.

I also thank Mr. Ivan Barker and Ms. Heather Bloomfield for helping me with taking high quality Scanning Electron Microscopy (SEM) images of many of my specimens. The damage evolution tests conducted in this study would not have been possible without support from Mr. Stephen Wood, who polished the specimen edges for me. I would also like to thank Dr. Joseph Umoh for performing Computer Tomography (CT) scans of some of the tested specimens.

I would like to extend my special thanks to my colleagues from the Composite Research Group (CRG) at University of Waterloo, especially Dr. Mehdi Ghazimoradi and Khizar Rouf, with whom I shared many interesting discussions.

I also would like to recognize the support from administrative staff at Mechanical and Materials Engineering (MME) department, especially Ms. Joanna Blom, and the engineering Information Technology (IT) help desk team.

Finally, I would like to appreciate all the help from my former colleague and best friend, Mingyu Yang, who made my life with regards to specimen preparations and test set-ups in the first two years of my time at Western significantly more efficient. I would also like to thank Dr. Mahdi Bagheripoor and Dr. Eric Mrindi Dusenge for showing me that the grass is greener where you water it, and not always on the other side. I am also grateful to the backing I received at various levels from all the friends I made while at Western, with whom I share many memorable moments.

Dedication

I would like to dedicate this PhD dissertation to my uncle, Mr. Prakash Suratkar, who has always guided me in my scientific pursuits from a very young age, and then, motivated me to pursue the PhD study.

Further, this thesis is also dedicated to my grandfather, (now retired) Prof. Vinod Nand, whose guidance was immensely valuable, especially when it came to writing the dissertation.

Finally, I would like to dedicate this thesis to my parents, younger brother, grandparents, uncles, aunts and cousins, and of course, my late grandfather, Mr. Prabhakar Suratkar. Their blessings, good wishes and support are what have gotten me through this hard, yet immensely rewarding, journey.

Table of Contents

Abstract	ii
Keywords	iii
Summary for Lay Audience	iv
Acknowledgments	v
Dedication	vi
Table of Contents	vii
List of Tables	xii
List of Figures	xiii
List of Appendices	xix
Abbreviations	xx
1 Introduction	1
1.1 Project scope and objectives	3
2 Background and Literature review	5
2.1 Classification of composites	5
2.1.1 Polymer matrix	6
2.1.2 Continuous fiber reinforcements	7
2.1.2.1 Unidirectional prepreg composites	7
2.1.2.2 Textile composites	8
2.1.2.3 Non-crimp fabric composites	9
2.2 Damage in composite materials	11
2.2.1 Loading modes in materials	11

2.2.2	Stress-intensity approach	12
2.2.2.1	Stress concentrations around the crack.....	12
2.2.2.2	Critical stress criterion.....	14
2.2.2.3	Crack tip plasticity.....	15
2.2.2.4	Influence of specimen thickness on crack tip plasticity	16
2.2.3	Energy-based approach.....	17
2.2.3.1	Griffith's theory of brittle fracture	18
2.2.3.2	Orowan's extension and a unified theory of fracture	20
2.2.3.3	Contributions to the work of fracture in composites	21
2.2.4	Damage monitoring techniques for composites.....	23
2.3	Mechanical characterization of and damage in continuous fiber reinforced composites.....	26
2.3.1	Quasi-static mechanical characterization.....	26
2.3.1.1	Tension and compression testing.....	26
2.3.1.2	In-plane shear testing.....	28
2.3.1.3	Interlaminar fracture toughness testing	29
2.3.2	Damage in composites under tension	32
2.3.2.1	Unidirectional lamina	32
2.3.2.2	Multidirectional laminates.....	34
2.3.3	Damage in composites under compression.....	38
2.3.3.1	Unidirectional lamina	38
2.3.3.2	Multidirectional laminates.....	44
3	Research objectives.....	46
3.1	Gaps in the literature.....	46
3.2	Research objectives.....	48

4	Materials and Methods	49
4.1	Material System	49
4.2	Test set-up	51
4.3	Test methods	52
4.3.1	Quasi-static characterization	52
4.3.1.1	Tension, compression and in-plane shear tests	52
4.3.1.2	Interlaminar fracture toughness tests	53
4.3.2	Damage evolution tests	56
4.3.3	Post-failure characterization	57
5	Results: Quasi-static material characterization	58
5.1	Tensile loads	58
5.1.1	Unidirectional lamina	58
5.1.2	Multidirectional laminates	59
5.2	Compressive loads	61
5.2.1	Unidirectional lamina	61
5.2.2	Multidirectional laminates	62
5.3	In-plane shear loads	63
5.4	Interlaminar fracture toughness tests	64
5.4.1	Crack propagation under Mode-I and Mode-II loads	64
5.4.1.1	Mode-I loads	64
5.4.1.2	Mode-II loads	67
5.4.2	Resistance curves and fracture toughness	68
5.4.3	Post-failure characterization	70
5.4.3.1	Mode-I loads	70
5.4.3.2	Mode-II loads	73

6	Results: Tensile damage in non-crimp fabric composites	75
6.1	Post-failure damage characterization of unidirectional composites	75
6.1.1	Failure under axial tension.....	75
6.1.2	Failure under transverse tension	77
6.2	Damage in multidirectional composites.....	78
6.2.1	Virgin specimens	78
6.2.2	Damage evolution under quasi-static tension	79
6.2.2.1	$[0/\pm 45/90]_s$ and $[0/\pm 45/90]_s$ laminates.....	79
6.2.2.2	$[\pm 45/0_2]_s$ and $[\pm 45/90_2]_s$ laminates	81
6.2.2.3	Damage quantification and stiffness degradation.....	83
6.2.3	Post-failure damage characterization.....	85
6.2.4	Energy dissipation in damage	88
7	Results: Compressive damage in non-crimp fabric composites	93
7.1	Post-failure characterization of damage in unidirectional composites	93
7.1.1	Failure under axial compression	93
7.1.2	Failure under transverse compression.....	94
7.2	Damage in multidirectional composites.....	94
7.2.1	Damage evolution under quasi-static compression.....	94
7.2.1.1	$[0/\pm 45/90]_s$ and $[90/\pm 45/0]_s$ laminates.....	95
7.2.1.2	$[\pm 45/0_2]_s$ and $[\pm 45/90_2]_s$ laminates	96
7.2.2	Post-failure damage characterization.....	98
7.2.2.1	$[0/\pm 45/90]_s$ and $[90/\pm 45/0]_s$ laminates.....	98
7.2.2.2	$[\pm 45/0_2]_s$ and $[\pm 45/90_2]_s$ laminates	101
7.2.3	Energy dissipation in damage	103

8	Discussion	109
8.1	Damage under tensile loads	109
8.1.1	Unidirectional composites	109
8.1.2	Multidirectional composites.....	110
8.2	Damage under compressive loads.....	111
8.2.1	Unidirectional composites	111
8.2.2	Multidirectional composites.....	112
8.3	Interlaminar fracture toughness tests	113
8.3.1	Unidirectional composites	113
8.3.2	Cross-ply composites	113
8.4	Energy dissipation in formation of damage	114
8.4.1	Tensile loads	114
8.4.2	Compression loads	114
9	Conclusions and recommendations of future works	115
9.1	Noteworthy conclusions.....	115
9.2	Key novelties	117
9.3	Recommendations for future work	117
9.4	Final word	118
	References	119
	Appendices.....	135
	Scholarly contributions	153
	Curriculum Vitae	154

List of Tables

Table 1: Quasi-static mechanical test parameters. ‘t’ stands for specimen thickness.	52
Table 2: Interlaminar fracture toughness under Mode-I and Mode-II loads in unidirectional and cross-ply laminates. All the values are reported in J/m^2	69
Table 3: Primary damage modes in multidirectional laminates under quasi-static compression	104
Table 4: Total energy dissipated in damage and damage areas in multidirectional laminates under compressive loading	106

List of Figures

Figure 1: Project task-flow.....	3
Figure 2: Classification of composites (Yang, 2019)	6
Figure 3: Structure of a unidirectional prepreg composite (Mattson, 2005).....	8
Figure 4: Examples of textile reinforcement architectures (Vallons, 2009).....	9
Figure 5: Macro-, meso- and micro-structure of NCF composites (Mattson, 2005)	10
Figure 6: Primary loading modes (Zimmermann, Launey, & Ritchie, 2022).....	12
Figure 7: (a) Kirsch's solution (Stress Concentrations at Holes, 2022) (b) Inglis's solution (Stresses At Elliptical Holes, 2022)	13
Figure 8: Fracture Process Zone and Singularity Dominated Zone near crack tip (The Elastic Stress Field around a Crack Tip, 2022)	15
Figure 9: Elasto-plastic distribution for Mode-I loading	16
Figure 10: (a) Influence of thickness on critical stress intensity factor (Roylance, 2001) (b) Conical transition from plane stress to plane strain (Schreurs, 2012)	17
Figure 11: (a) Released strain energy adjacent to the crack (Roylance, 2001) (b) Energy balance (Roylance, 2001).....	19
Figure 12: (a) Matrix cracks and delamination in continuous fiber reinforced carbon fiber epoxy composites (b) Process of hackle formation in composites (Bruce, 2011)	22
Figure 13: Comparison of available shear test methods (Adams, 2009)	28
Figure 14: Sequence of events leading to failure in unidirectional composites under axial tensile loads: (1) Single fiber breaks (2-4) Breaks in neighboring fibers (5) Critical cluster of broken fibers (6) Catastrophic failure (Raz-Ben Aroush, et al., 2006).....	33

Figure 15: (a) Damage initiation in the form of interface debonds (b) Coalescence of debonds into transverse cracks (adapted from Gamstedt & Sjögren, 1999)	34
Figure 16: Types of transverse cracks observed in NCF composites under tensile loads (adapted from Edgren, Mattsson, Asp, & Varna, 2004)	37
Figure 17: Axial compression failure modes (a) Fiber shear failure (Agarwal, Broutman, & Chandrashekhara, 2015) (b) Typical kink-band geometry (Gutkin, Pinho, Robinson, & Curtis, 2010)	39
Figure 18: Stages of fiber displacement in kink-band formation (Wang, et al., 2021)	40
Figure 19: Failure under transverse compressive load (Agarwal, Broutman, & Chandrashekhara, 2015)	43
Figure 20: Coupons failed under transverse compression at (a) quasi-static (b) intermediate (c) high strain rates (Rouf, et al., 2021)	44
Figure 21: Schematic of High-Pressure Resin Transfer Molding (HP-RTM) process (Meirson, 2018).....	50
Figure 22: INSTRON 8804 servo-hydraulic test frame.....	51
Figure 23: Representative test coupon geometry for (a) tensile test (b) compressive test (c) V-Notch in-plane shear test. ‘t’ stands for specimen thickness. All dimensions are in ‘mm’....	53
Figure 24: (a) Schematic for typical Double Cantilever Beam (DCB) test specimen (b) DCB test set-up	54
Figure 25: End Notch Flexure (ENF) test set-up	56
Figure 26: $[0/\pm 45/90]_s$ laminate microstructure on: (a) Actual edge (b) Replicating tape (c) Crack on replicating tape	57
Figure 27: Stress-strain curves for unidirectional lamina under (a) axial tensile loads (b) transverse tensile loads	59

Figure 28: Tensile stress-strain curves for (a) $[0/\pm 45/90]_s$ laminate (b) $[90/\pm 45/0]_s$ laminate (c) $[\pm 45/0_2]_s$ laminate (d) $[\pm 45/90_2]_s$ laminate	60
Figure 29: Stress-strain curves for unidirectional lamina under (a) axial compressive loads (b) transverse compressive loads	62
Figure 30: Compressive stress-strain curves for (a) $[0/\pm 45/90]_s$ laminate (b) $[90/\pm 45/0]_s$ laminate (c) $[\pm 45/0_2]_s$ laminate (d) $[\pm 45/90_2]_s$ laminate	63
Figure 31: (a) Stress-strain curves for unidirectional lamina under in-plane shear loads (b) Notch-root splits observed during the V-Notch rail shear test	64
Figure 32: Filtered Mode-I load-displacement curves for (a) unidirectional lamina (b) cross-ply laminate.....	65
Figure 33: Mode-I interlaminar crack propagation in (a) unidirectional lamina (b) cross-ply laminate (through-thickness views)	65
Figure 34: Representative Mode-I interlaminar crack propagation characteristics in (a) unidirectional lamina (b) cross-ply laminate	66
Figure 35: Top views of tested (a) unidirectional (b) cross-ply test coupons.....	67
Figure 36: Mode-II load-displacement curves for (a) unidirectional lamina (b) cross-ply laminate.....	67
Figure 37: Representative Mode-II interlaminar crack propagation characteristics in (a) unidirectional lamina (b) cross-ply laminate	68
Figure 38: Representative R-curves for (a) unidirectional lamina (b) cross-ply laminates....	69
Figure 39: SEM characterization of the fracture surfaces of unidirectional composites under Mode-I loads	71
Figure 40: SEM characterization of the fracture surfaces of cross-ply laminates under Mode-I loads	72

Figure 41: (a-b) SEM characterization of the fracture surfaces of unidirectional composites under Mode-II loads (c-d) SEM characterization of the fracture surfaces of cross-ply laminates under Mode-II loads	74
Figure 42: (a) Specimen failed under axial tension (b) Image of the edge of failed specimen taken using optical microscope (c, d) Images of the failed surface taken using SEM	76
Figure 43: (a) Specimen failed under transverse tension (b) Image of the edge of failed specimen taken using optical microscope (c, d) Images of the failed surface taken using SEM	77
Figure 44: Edge replicas of virgin (a) $[0/\pm 45/90]_s$ laminate (b) $[90/\pm 45/0]_s$ laminate (c) $[\pm 45/0_2]_s$ laminate (d) $[\pm 45/90_2]_s$ laminate.....	78
Figure 45: Stress-strain curves from interrupted tension tests for (a) $[0/\pm 45/90]_s$ laminate (b) $[90/\pm 45/0]_s$ laminate.....	79
Figure 46: Damage features in the $[0/\pm 45/90]_s$ laminate under tension at (a) 0.29% strain (b) 0.61% strain (c) 0.86% strain (d) 1.29% strain.....	80
Figure 47: Damage features in the $[90/\pm 45/0]_s$ laminate under tension at (a) 0.70% strain (b) 1.10% strain	81
Figure 48: Stress-strain curves from interrupted tension tests for (a) $[\pm 45/0_2]_s$ laminate (b) $[\pm 45/90_2]_s$ laminate	81
Figure 49: Damage features in the $[\pm 45/0_2]_s$ laminate under tension at (a) 0.69% strain (b) 1.23% strain	82
Figure 50: Damage features in the $[\pm 45/90_2]_s$ laminate under tension at (a) 0.37% strain (b) 0.58% strain (c) 0.76% strain (d) 1.25% strain.....	83
Figure 51: Influence of stacking sequence on (a) total damage area (b) laminate stiffness degradation (c) 90/90 delamination crack growth (d) ply crack multiplication in 90° plies (e) +45/-45 delamination growth (f) ply crack multiplication in 45° plies	84

Figure 52: Post failure surfaces of (a) $[0/\pm 45/90]_s$ laminate (b) $[90/\pm 45/0]_s$ laminate (c) $[\pm 45/0_2]_s$ laminate (d) $[\pm 45/90_2]_s$ laminate.....	86
Figure 53: (a-b) Post failure surface of 0° plies (c) Edge image of failed 0° ply (d-e) Post failure surface of 90° plies (f) Edge image of failed 90° ply	87
Figure 54: (a-b) Post failure surface of 45° plies (c) Edge image of failed 45° ply	88
Figure 55: Stress-strain curves from loading-unloading test for (a) $[0/\pm 45/90]_s$ laminate (b) $[90/\pm 45/0]_s$ laminate (c) $[\pm 45/0_2]_s$ laminate (d) $[\pm 45/90_2]_s$ laminate	90
Figure 56: Energy dissipated in and stiffness drops in (a) $[0/\pm 45/90]_s$ laminate (b) $[90/\pm 45/0]_s$ laminate (c) $[\pm 45/0_2]_s$ laminate (d) $[\pm 45/90_2]_s$ laminate	91
Figure 57: (a-c) Failure by out-of-plane kink band formation in unidirectional lamina under axial compression.....	93
Figure 58: (a) Unidirectional lamina failed under transverse compression (b-c) Edge images of the test coupon failed under transverse compression	94
Figure 59: Stress-strain curves from interrupted compression tests for (a) $[0/\pm 45/90]_s$ laminate (b) $[90/\pm 45/0]_s$ laminate	95
Figure 60: Damage in compression loaded (a) $[0/\pm 45/90]_s$ laminate at 0.71% strain (b) $[0/\pm 45/90]_s$ laminate at 0.98% strain (c) $[90/\pm 45/0]_s$ laminate at 0.39% strain (d) $[90/\pm 45/0]_s$ laminate at 0.54% strain.....	96
Figure 61: Stress-strain curves from interrupted compression tests for (a) $[\pm 45/0_2]_s$ laminate (b) $[\pm 45/90_2]_s$ laminate.....	97
Figure 62: Damage in compression loaded (a) $[\pm 45/0_2]_s$ laminate at 0.23% strain (b) $[\pm 45/0_2]_s$ laminate at 0.60% strain (c) $[\pm 45/90_2]_s$ laminate at 0.63% strain (d) $[\pm 45/90_2]_s$ laminate at 0.97% strain	97
Figure 63: (a) $[0/\pm 45/90]_s$ laminate failed under compression (b-e) Edge images of failed $[0/\pm 45/90]_s$ laminate under compression	99

Figure 64: (a) $[90/\pm 45/0]_s$ laminate failed under compression (b-d) Edge images of failed $[90/\pm 45/0]_s$ laminate under compression 100

Figure 65: (a) $[\pm 45/0_2]_s$ laminate failed under compression (b-d) Edge images of failed $[\pm 45/0_2]_s$ laminate under compression 102

Figure 66: (a) $[\pm 45/90_2]_s$ laminate failed under compression (b-d) Edge images of failed $[\pm 45/90_2]_s$ laminate under compression 103

Figure 67: Representative load-displacement curves for (a) $[0/\pm 45/90]_s$ laminate (b) $[90/\pm 45/0]_s$ laminate (c) $[\pm 45/0_2]_s$ laminate (d) $[\pm 45/90_2]_s$ laminate 105

Figure 68: Comparison of predicted delamination lengths and post-failure measurements in $[0/\pm 45/90]_s$ and $[90/\pm 45/0]_s$ laminates under compression 108

List of Appendices

Appendix 1: Stress concentration equations	135
Appendix 2: EPIKOTE™ Resin TRAC 06150 resin data sheet.....	137
Appendix 3: ZOLTEK™ PX35 unidirectional fabric data sheet.....	142
Appendix 4: Plaque of NCF composites manufactured using HP-RTM process with specimen cutting position.....	144
Appendix 5: Alternate data reduction methods for Mode-I fracture toughness	145
Appendix 6: Engineering properties of NCF carbon fiber epoxy composites under quasi-static loads.....	147
Appendix 7: Unfiltered load-displacement curves under Mode-I loads.....	148
Appendix 8: Mode-I crack growth characteristics in unidirectional lamina.....	148
Appendix 9: Mode-I crack growth characteristics in cross-ply laminates.....	148
Appendix 10: Mode-II crack growth characteristics in unidirectional lamina	149
Appendix 11: Mode-II crack growth characteristics in cross-ply laminates	149
Appendix 12: R-curves under Mode-I opening loads.....	149
Appendix 13: R-curves under Mode-II shearing loads.....	150
Appendix 14: Energy balance for damage in composites.....	150
Appendix 15: Energies supplied, stored elastically and dissipated in multidirectional composites under compression	152

Abbreviations

AE – Acoustic Emission

ASTM – American Society for Testing and Materials

BSE – Electron Backscattering

CC – Compliance Calibration

COD – Crack Opening Displacement

CSD – Crack Sliding Displacement

DCB – Double Cantilever Beam

DE – Damage Evolution

DIC – Digital Image Correlation

ENF – End Notch Flexure

ER – Edge Replication

FPC – Fraunhofer Project Center

FPZ – Fracture Process Zone

GLOBLOC – Global-Local Approach

G_c – Critical strain energy release rate

G_{Ic} – Mode-I fracture toughness

G_{IIc} – Mode-II fracture toughness

HP-RTM – High Pressure-Resin Transfer Molding

IMR – Internal Mold Release

L-uL – Loading-unloading

MBT – Modified Beam Theory

MCC – Modified Compliance Calibration

MoC – Materials of Construction

NCF – Non-Crimp Fabric

NDT – Non-Destructive Techniques

NSERC - Natural Sciences and Engineering Research Council

OEM – Original Equipment Manufacturers

R-curve – Resistance curve

RTM – Resin Transfer Molding

SDZ – Stress Dominated Zone

SEM – Scanning Electron Microscopy

UD – Unidirectional

Chapter 1

1 Introduction

Composites are heterogeneous materials made by combining two or more materials with fundamentally different material properties. They consist of an easily available, usually softer ‘matrix’, strengthened by a generally stiffer ‘reinforcement’. The matrix material may be a polymer, metal or ceramic material. The main functions of matrix are to keep the reinforcement phase in its desired phase and shield it from environment. The reinforcing phase could be stiff fibers, either chopped and dispersed into the matrix or present as continuous, straight bars in the matrix, or could be particles dispersed in the matrix. The properties of the composites may easily be tuned by modifying the constituent materials or by changing the arrangement (also referred to as ‘architecture’) of the reinforcement phase. This aspect of the composites enables design of materials tailored to the applications. Furthermore, composites have a higher strength-to-weight ratio than traditional metals and a better chemical resistance while allowing novel design possibilities.

Composites have gained wide acceptance in recent times as a replacement of traditional metallic Materials of Construction (MoC). From the energy sector to sports and recreation, composites are finding applications everywhere. One such sector where there is a high demand for composites is the transportation. The aviation industry has already made giant strides with the use of advanced composites for structural applications in the Boeing 787 Dreamliner and Airbus A350XWB aircraft types.

The use of composites for structural applications in light-weight automotive has also gained momentum in the recent decade. The key driving force behind the shift from steel and aluminum (which have been traditional choices for car components) to lightweight composites is the increasing legislative pressure on the automobile Original Equipment Manufacturers (OEMs) globally to dramatically reduce carbon-di-oxide/greenhouse gas emissions from passenger cars (Lightweight, heavy impact), as an increasing number of countries continue to pledge carbon neutrality by the second half of twenty first century

(Carbon Neutrality Goals by Country, 2021). Reports suggest that a 10% reduction in vehicle weight improves fuel economy of passenger cars by 6-8% and that of electric vehicles by 10% (Global Market Insights, 2020), helping curb the emissions.

Another contributing factor to this shift is the changing outlook of end-user customers. Customer are becoming increasingly more aware and sophisticated in their demands. Henry Ford's axiom "You can have any color, as long as it's black" is steadily losing ground as customers are now demonstrating a willingness to pay more for refined product differentiations, which may also be fulfilled with composites. Therefore, the size of automotive composites market was greater than USD 3.8bn in 2020 and is projected to grow annually at a rate of 6.9% till 2027, with major contribution to their widescale adoption taking place in Asia-Pacific markets (Global Market Insights, 2020).

The adoption barriers to composites have traditionally been higher raw material costs and slow production rates. The drive to offset these barriers has led to the rise of many disruptive technologies in the recent years, like fast curing chemical resins, novel fiber reinforcement architectures, improved production methods, automation technologies, etc. The single-most important criteria in the acceptance and adoption of these novel technologies is, however, the "crashworthiness" of resulting structures. Crashworthiness is the ability of a structure to absorb energy upon impact and, in the case of an automobile, keep the passengers inside safe.

Metallic structures absorb energy in a crash event primarily through plastic deformation, which manifests itself as a "dent" on a car body. The energy absorption in composites structures is, on the other hand, a superposition of multiple events such as cracks in the matrix phase, debonding along matrix-reinforcement interface, reinforcement breakage, etc., whose occurrence may or may not be dependent on each other. The damage events, or damage modes, are strongly dependent on the constituent phases of composites, the reinforcement architecture and processing parameters during manufacturing. It is, hence, very critical to study the mechanical behavior of the material system in question thoroughly and understand the damage in the materials, from its initiation to final failure; which is the central topic of this PhD study.

1.1 Project scope and objectives

The research conducted in this research is industrially driven and funded by Honda R&D Americas, Zoltek, Hexion, Laval International, Fraunhofer Project Center at Western University and Natural Sciences and Engineering Research Council (NSERC). The project, at large, is a collaboration between graduate students, post-doctoral fellows and Professors from Western University and University of Waterloo (Figure 1). The final aim of the project is to collectively generate a robust energy-based model with capabilities to predict the crash behavior of the Non-Crimp Fabric (NCF) carbon fiber reinforced epoxy composites for structural applications in lightweight automobiles.

The research is focused on the damage in NCF composites under quasi-static mechanical loads. A mechanical property data set for calibration of a material constitutive model was generated, followed by an experimental investigation on initiation and propagation of various damage modes in NCF composite materials under tensile and compressive loads. Finally, a connection between the damage modes and energy required in their creation is made.

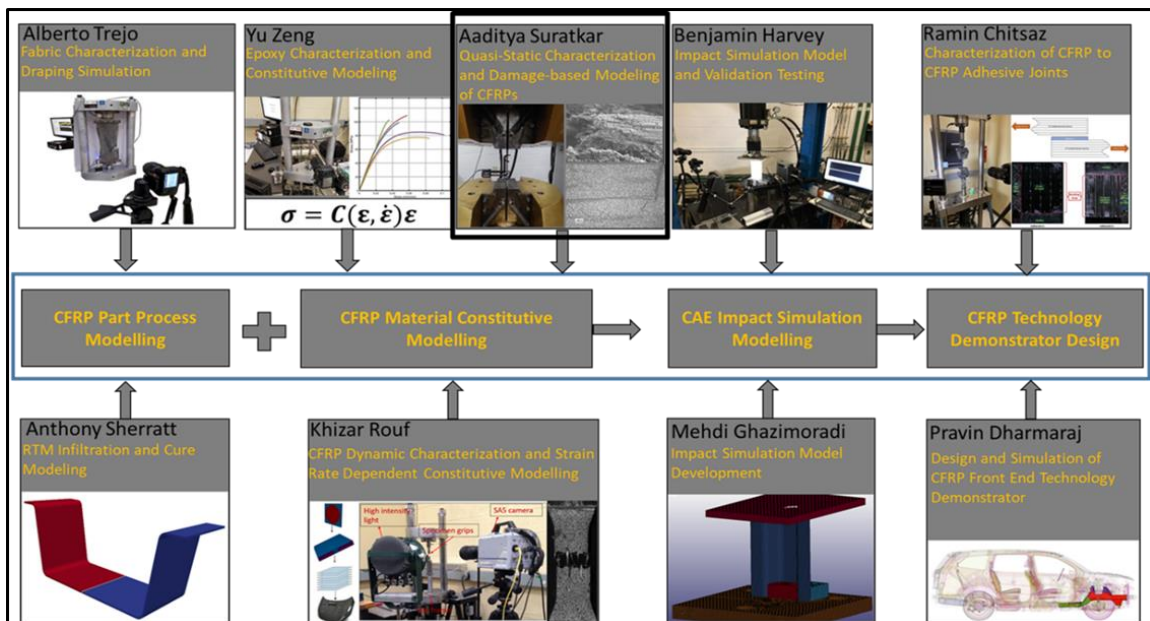


Figure 1: Project task-flow

Description of damage in materials has been a subject of study for over six decades now. Monitoring and describing the damage in composites continues to be a complicated affair, as damage in composites occurs in the form of multiple damage modes. Some of the researchers have developed mathematical expressions to explain the formation and growth of damage, while others have described the damage in terms of the amount of energy required to create a certain form of damage. The theory of damage in composite materials is described in Chapter 2, along with a brief overview of common damage monitoring techniques. Chapter 2 also contains a literature review on the work done in the fields of mechanical testing and damage development in composites. Although there have been numerous studies on damage in composite materials, it was observed that very few of the studies were focused on NCF composite materials. It was also observed that simplifying assumptions were made in many of the numerical studies, but there lacked comparative experimental data for NCF composites. Such specific gaps in the available information are clearly outlined in Chapter 3.

Chapter 4 discusses in detail the specifics of the examined material system, along with the employed test methods, protocols and standards. The results from the mechanical characterization tests are discussed in Chapter 5. The damage, from initiation to final failure, under tensile and compressive loads was examined using in-situ damage monitoring and microscopy techniques. The complete pictures of damage under tensile and compressive loads are provided in Chapter 6 and Chapter 7 respectively. The damage is also connected to the amount of energy dissipated in its creation in these chapters.

A high-level summary of the results is provided in Chapter 8. It discusses the correlations between the results and how they fill the gaps in the state-of-the-art. Finally, the dissertation ends with concluding remarks and key novelties of this work in Chapter 9. Suggestions for possible avenues of future work are also made in Chapter 9.

Chapter 2

2 Background and Literature review

This chapter intends to provide the reader a background of the composite materials and damage occurring in them. As was mentioned in the previous chapter, composite materials are heterogenous materials consisting of fundamentally dissimilar matrix and reinforcement phases. The chapter starts with a broad overview of classification of composites based on matrix and reinforcement types. The chapter then discusses in detail, the descriptions of damage in materials and their extension to composite materials. Commonly employed damage monitoring techniques for composite materials are also discussed. The chapter then provides a comprehensive literature review of the existing work on mechanical characterization of damage in composite materials (on the aspects within scope, as mentioned in Section 1.1), with a focus on NCF composites.

2.1 Classification of composites

Composite materials can broadly be classified as shown in Figure 2 based on the type of matrix and reinforcement materials (Yang, 2019). The materials can be classified by the chemical nature of matrix material, i.e. by if the matrix is either a polymer, metal or a ceramic. The composites are broadly classified further depending on the geometry (if the reinforcing phase is primarily fibers, particles, etc.), size (length of the fibers, diameter of particles, etc.) and arrangement (if the fibers are randomly dispersed, if the reinforcing phase is present as a stack of aligned continuous fibers, etc.) of the reinforcing phase. Although the broad classification in Figure 2 encompasses a wide range of materials, the discussion in this study would be focused on “continuous fiber reinforced polymer composites”.

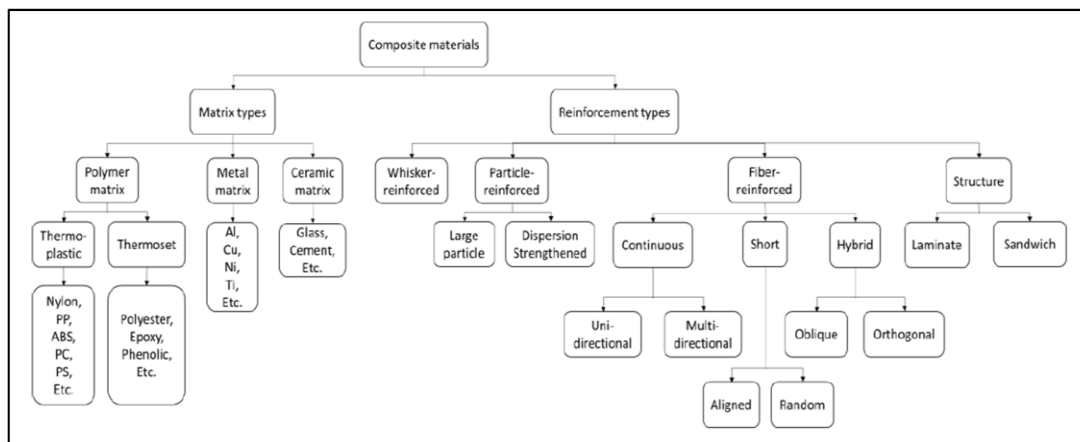


Figure 2: Classification of composites (Yang, 2019)

2.1.1 Polymer matrix

Polymer matrices are classified as thermosets and thermoplastics resins, based on the intermolecular forces between the polymer chains (Yang, 2019). Thermosets are irreversibly cured polymers which are characterized by the presence of covalent cross-links between the polymer chains, leading to a rigid and stable three-dimensional structure. However, they cannot be remolded. Thermoplastics, on the other hand, can be easily melted and reshaped through multiple cycles. The association of polymer chains in thermoplastics is due to weak physical bonds (such as van der Waals forces). Therefore, the polymer chains have a greater freedom to slide past each other at higher temperatures, when the physical forces holding the chains together are weakened. It is, however, very important to accurately characterize the thermal behavior of thermoplastics before they are subjected to heat cycles.

Both, thermosets and thermoplastics, have their own set of advantages and disadvantages. Thermosets offer a higher temperature resistance and a higher dimensional stability. They generally have low viscosity, which makes it easier to process thermosets. They are cost-effective and offer a superior aesthetic appearance but cannot be remolded, as mentioned before. The thermoplastics, on the other hand, offer a greater window for recycling and a higher tunability of properties but are more expensive than the thermosets (Thermoset Vs. Thermoplastics, 2017).

However, an article published in the Composites World magazine (Brosius, 2015) maintained a more neutral stance on the thermoset vs thermoplastic debate. The newer manufacturing technologies in thermoplastics, mainly structure injection overmolding (wherein a continuous fiber backbone is placed in the injection mold and overmolded with a thermoplastic material) and thermoplastic Resin Transfer Molding (RTM; where a low viscosity monomer is mixed with an initiator for in-situ polymerization), are placing them fair and square against the thermosets. The focus of this thesis, however, will be on thermoset composites.

2.1.2 Continuous fiber reinforcements

2.1.2.1 Unidirectional prepreg composites

Unidirectional (UD) prepreg composites are multiple layers of thin sheets, comprising of fibers aligned in a single direction, stacked in desired orientations (Figure 3). The thin sheets, the prepregs, are made of fibers pre-impregnated into partially cured resin material. A prepreg sheet is formed by passing uniformly spaced fibers through a resin melt of a controlled viscosity, which is then partially cured by applying heat. The sheets may then be stored for a certain length of time, varying from days to months, depending on the curing characteristics of the resins and storing conditions. Some polymer materials may continue to cure at room temperature, which severely shortens their shelf lives. The shelf lives of prepreg sheets may be increased by storing them at low temperatures, which increases the overall cost of materials. Composite parts are formed from the prepreg sheets by stacking the sheets in desired orientations. The stack is subjected to vacuum to remove air bubbles and then placed in an autoclave to complete the curing process (Vallons, 2009).

These materials exhibit high in-plane strength and stiffness due to the highly aligned fibers with high fiber volume fractions. However, they are less stable in transverse direction (Vallons, 2009) and are susceptible to delamination (Mattson, 2005). They are also expensive to manufacture due to the associated storage and autoclave costs.

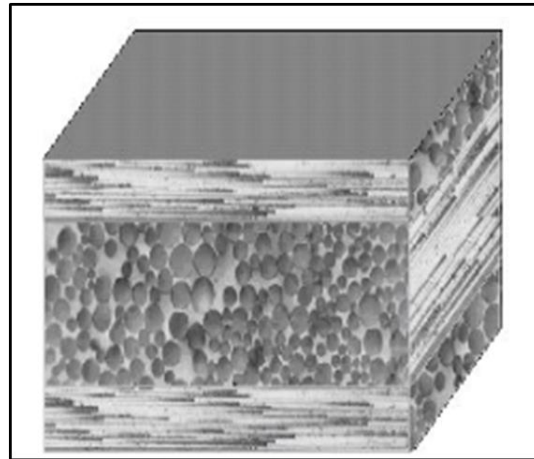


Figure 3: Structure of a unidirectional prepreg composite (Mattson, 2005)

2.1.2.2 Textile composites

The disadvantages associated with unidirectional prepreg composites such as constraints with prepreg shelf life, higher handling cost, etc. could be overcome to a certain degree by the use of textile blankets. The woven textiles are blankets of interlocked fiber bundles or yarns. Some examples of woven reinforcement architectures are shown in Figure 4. The interlocked fibers may be randomly oriented in the plane of fabric, perpendicular to each other or at other angles. As the textile blankets are dry almost till the point of being placed in the mold, they do not have shelf-life limitations, are cheaper to store and are easier to handle than unidirectional prepreg sheets. Furthermore, they offer better draping abilities and higher damage tolerance.

The properties of the textile composites are, however, governed by the amount of crimp or the out-of-plane folding in the materials. If the textiles have a high degree of crimp with respect to the global loading direction, the in-plane properties, especially in-plane compression properties, of the composites may be lower than the corresponding unidirectional prepreg composites, in which the fibers could be considered to be perfectly straight. Therefore, although textile composites offer possibilities for more economic production than unidirectional prepreps, the presence of a certain degree of crimp in virtually all textile architectures causes the textile composites to have comparatively inferior in-plane mechanical properties.

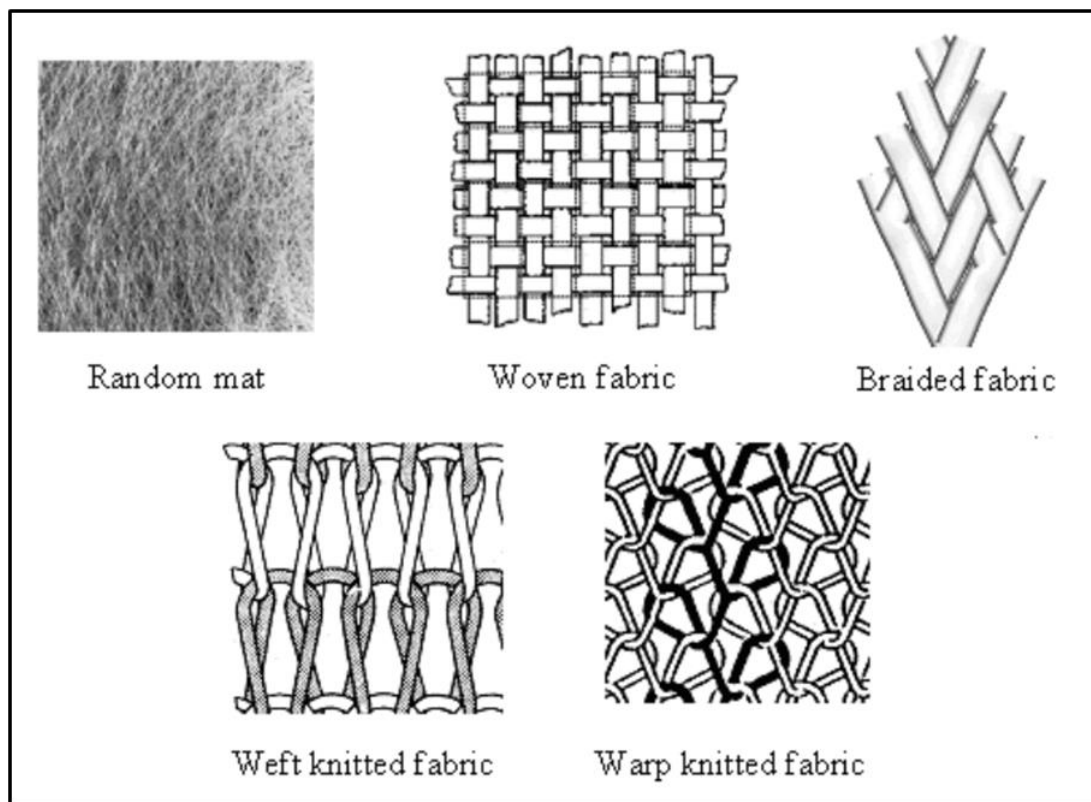


Figure 4: Examples of textile reinforcement architectures (Vallons, 2009)

2.1.2.3 Non-crimp fabric composites

A new class of composite materials, called as ‘Non-Crimp Fabric composites’ has emerged in the recent years, which lies at the intersection of unidirectional prepreg and textile composites. Fiber bundles are first stitched together into a unidirectional fabric in these materials. These unidirectional fabrics are then stacked on top of each other in desired orientations. The fabrics may either be stitched together or held together with a chemical binder. The stack of fabric is then placed in the mold and impregnated with the resin to form the final composite part. The dry fabrics are easier to handle, like in the case of textile reinforcements, but have a very limited degree of crimp, like unidirectional prepreg materials. NCF composites have been reported to have a 35% lower production cost as compared to unidirectional prepreps. Significant material and labor cost savings were also reported for NCF composites (Bibo, Hogg, & Kemp, 1997).

NCF composites are inherently multi-scale materials (Figure 5). At the microscale, NCF composites may be described as unidirectional materials with a certain fiber volume fraction. The distinguishing characteristics of NCF composites are, however, the properties of bundles at mesoscale such as the fiber volume content in the bundle and the localized waviness of bundles. The waviness in the bundles may be introduced by either manufacturing parameters or the stitching threads used to knit the fiber bundles into fabric. The stitching threads push the bundles (and the adjacent fabrics) apart creating resin-rich areas in the materials, creating local weak spots.

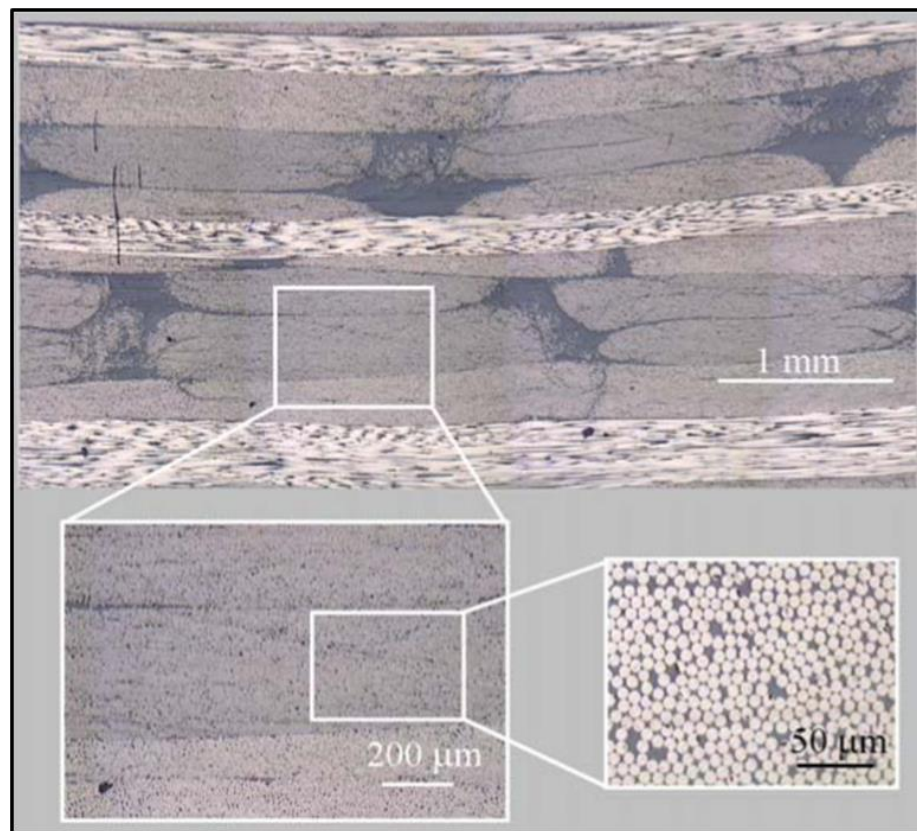


Figure 5: Macro-, meso- and micro-structure of NCF composites (Mattson, 2005)

2.2 Damage in composite materials

As was alluded to in Chapter 1, composites absorb energy in a crash event through multiple damage modes. The occurrence and extents of these modes depend very strongly on the constituent materials and reinforcement architectures. It is, hence, very critical from a design perspective to understand and be able to predict the different damage modes that may occur in the structures made with different types of composites. Several researchers have attempted over the last seven decades to describe the damage through two primary approaches, a stress-based approach and an energy balance approach. This section provides the reader with a background on the descriptions of damage, first in isotropic materials and then the extension to the case of composite materials.

2.2.1 Loading modes in materials

Damage initiates and propagates in materials under three primary loading modes (Figure 6). Depending on the orientation of the crack relative to the loading direction, the crack or flaw may either be subjected to a tensile stress opening up the cracks ('Mode-I') or a shear stress caused by sliding of the cracks parallel to primary crack orientation ('Mode-II'). The crack may also slide perpendicular to their orientation ('Mode-III'). Being loaded in either of the above modes (or mixtures thereof) leads to stress concentrations around defects in the materials, such as voids. The pioneering researchers in the field developed mathematical expressions to explain this stress concentration and its effect on the propagation of flaw. This approach towards description of damage is called as a 'stress intensity' approach. Although the stress intensity approach is useful in engineering practices, an alternative 'energy based' approach was developed by another group of researchers, which was based on energy-balance arguments. Both the approaches are discussed in detail in subsequent sections.

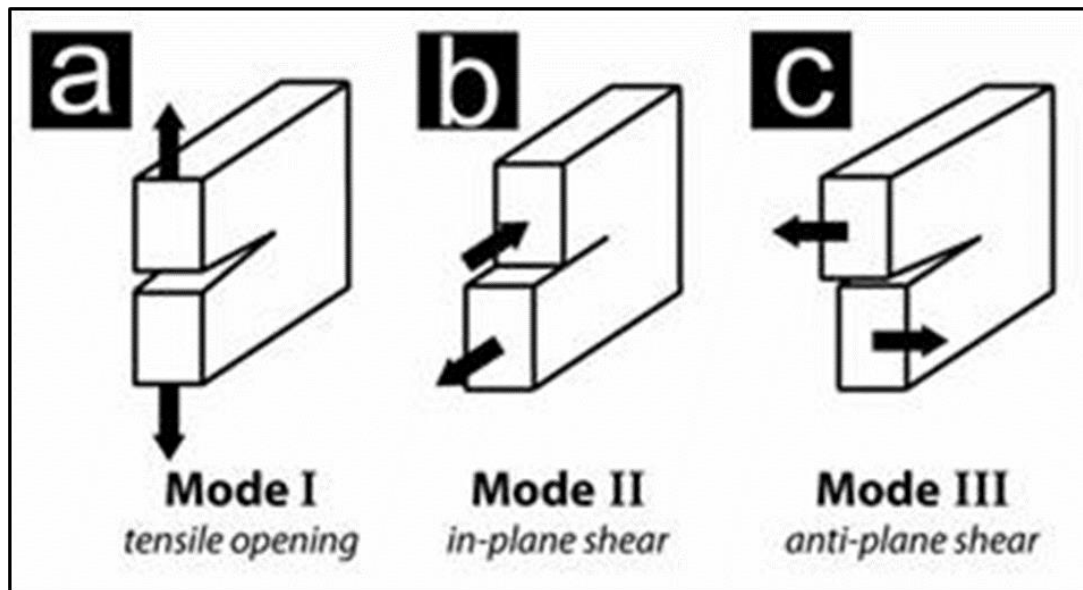


Figure 6: Primary loading modes (Zimmermann, Launey, & Ritchie, 2022)

2.2.2 Stress-intensity approach

2.2.2.1 Stress concentrations around the crack

The stress concentrations were first mathematically expressed by the scientist named Ernst Kirsch (Stress Concentrations at Holes, 2022). Kirsch considered a circular hole in an infinite plate (Figure 7.a.), subjected to uniaxial tension, in his analysis. He developed equations describing the stress state around the hole as a function of applied stress (σ_{app}), radius of hole (a) and distance from hole (r) in polar co-ordinate system. The equations (Equation 1.1-1.3) derived by Kirsch are mentioned in Appendix 1. According to Kirsch's equations, the stress at the edge of hole (i.e., when $r = a$) was three times higher than the applied stress for isotropic materials. The factor of three, though, was independent of the radius of the hole. This was a counter-intuitive result, as in physical realm, it would mean that a small hole would cause as much stress concentration as a large hole. This presented inherent limitations while extending the result to elliptical cracks which had a larger width but smaller height.

The major step, overcoming the limitation in Kirsch's solution, was taken by Inglis (Inglis, 1913). Inglis' approach considered the flaw to be of an elliptical shape in an infinite plate. Hence, by varying the aspect ratio of ellipse, multiple scenarios could be considered. Inglis's mathematical description (Equation 1.4) can be found in Appendix 1. If the major axis dimension is set equal to minor axis dimension, Inglis's solution decomposes to Kirsch's solution. However, by the mathematical equation, if the minor axis ($2b$, as marked in Figure 7.b.) approached zero, the stress at the crack tip would be infinite. This was qualitatively invalid, as it would mean that the structure would fail at the slightest of the applied loads.

A few years later, another scientist, Harold Westergaard, developed equations using Airy function of complex numbers to express the rectangular co-ordinates (Sanford, 2003, Westergaard's Solution for Cracks, n.d.) for a bi-axial tensile loading case. The equations (Equation 1.5-1.7 in Appendix 1) were easier to interpret than Inglis's solution. The solution, however, failed to provide any additional insight into the stress intensifications.

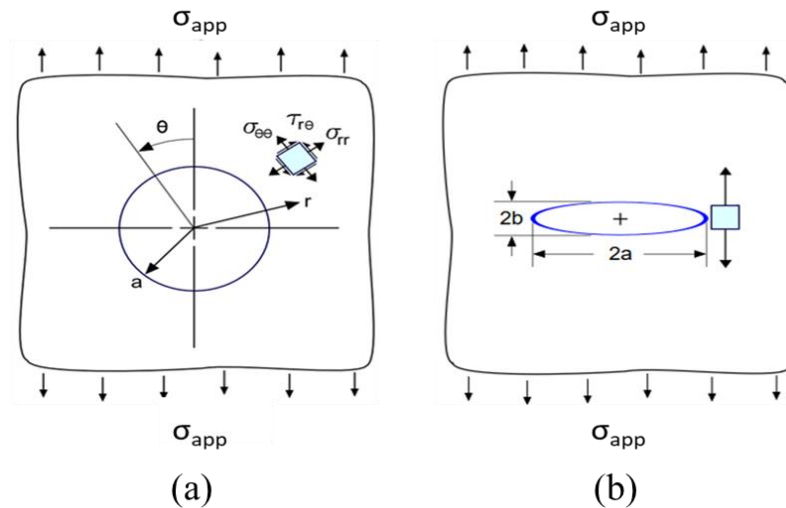


Figure 7: (a) Kirsch's solution (Stress Concentrations at Holes, 2022) (b) Inglis's solution (Stresses At Elliptical Holes, 2022)

One of the most important developments in this field came in the 1950s: Irwin's approximation of Westergaard's solution (Sanford, 2003, Stress Intensity Factor, 2022). Irwin mathematically proved that Westergaard's complete solution could be greatly simplified around the crack tip by defining the Airy function as a set of complex numbers in radial co-ordinate system (Appendix 1, Equation 1.8). On comparing the simplified solution to the complete solution, Irwin defined the variable 'K', called stress intensity factor, and the near-field equations (Appendix 1, Equations 1.8-1.11). 'K' describes the stress state at crack tip and is used to define the critical stress failure criterion. Mathematical expression for 'K' is given below (Equation 1). Irwin's extension in itself however, failed to address the limitation of infinite stresses at crack tip (the so-called 'singularity problem') and failed to give any insight on dependence of fracture behaviour on geometric factors such as thickness and width of the specimen.

$$K = \sigma\sqrt{\pi a} \dots (1)$$

2.2.2.2 Critical stress criterion

As was discussed in Section 2.2.2.1, Irwin represented the stress intensity parameter by inverse square root singular stresses at the crack tip. Irwin expressed his criterion as: $K_{@failure} = K_c$ (Sanford, 2003, The Elastic Stress Field around a Crack Tip). In words, a material body will fail in a brittle fashion when the stress state in the immediate vicinity of the crack tip exceeds a critical value. Irwin defined a singularity stress dominated zone (SDZ) around the crack tip and the area in the immediate vicinity as fracture process zone (FPZ), and FPZ is completely enclosed by SDZ (Figure 8). The $K_{@failure}$ is the applied K, depending on the applied stress and flaw length. The K_c is called 'critical stress intensity factor' and is a material property (measured under plane strain conditions). As will be discussed later in Section 2.2.2.3, non-linear material behavior occur in FPZ, which the criterion ignores. For the criterion to be valid, the FPZ must be sufficiently small (The Elastic Stress Field around a Crack Tip, 2022).

Furthermore, care must be taken while scaling the structures up based on this criterion. A direct scale-up does not account for the fact that larger structures cannot withstand as high stresses as their smaller counterparts. An interdependence of maximum allowable stresses and critical crack lengths must hence be plotted for all relevant components constituting the overall structure, and this failure locus must be referred to for permissible dimensions and factors of safety while scaling the structures up.

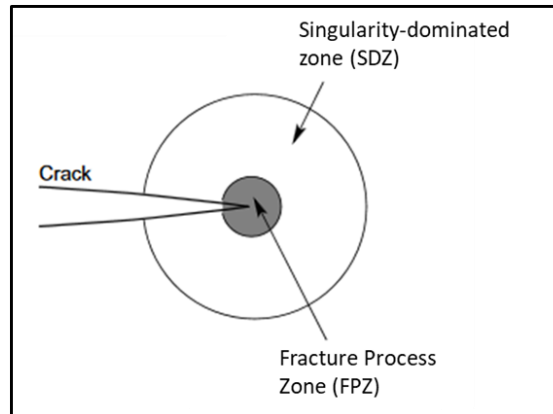


Figure 8: Fracture Process Zone and Singularity Dominated Zone near crack tip
(The Elastic Stress Field around a Crack Tip, 2022)

2.2.2.3 Crack tip plasticity

When subjected to tensile stresses, the crack opens, blunting the crack tip. Mathematical attempt was made to describe the crack tip in terms of its deformed shape rather than undeformed. This mathematical trick did predict finite stresses at the crack tip but failed to qualitatively explain the non-linear deformations occurring in the FPZ. An exact solution for the stress distribution at the crack tip was available under Mode-III stresses (Hult & McClintock, 1956), which was adapted for Mode-I tensile stresses.

The key results suggest that the stress cannot exceed the yield stress near crack tip. Hence as the stress exceeds the yield stress, the stress gets redistributed in front of the crack tip as local plastic deformation. With reference to Figure 9, the physical manifestation of this localized plastic deformation is that the stress distribution (shaded region, labelled as A) gets distributed by an equal amount as the plastic zone (r_y) to the left to give the depth of plastic zone (shaded region, labelled as B), hence restoring equilibrium. Assuming that

the FPZ is completely enclosed within SDZ, the crack length (a), is replaced by an effective notational crack length ($a+r_y$). The stress distribution and elasto-plastic characteristics are still governed by stress intensity factor (Sanford, 2003, Roylance, 2001).

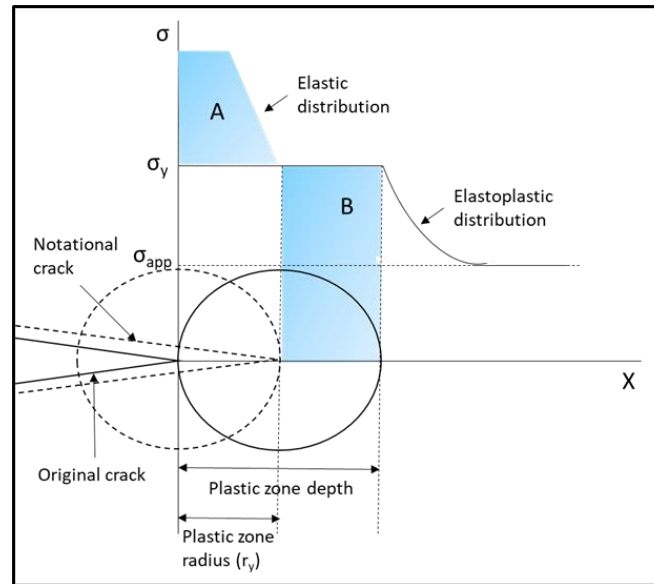


Figure 9: Elasto-plastic distribution for Mode-I loading

2.2.2.4 Influence of specimen thickness on crack tip plasticity

From the above arguments, it is clear that fracture mechanics effectively entails studying the resistance to brittle fracture and involves quantifying the extent of plastic deformation at the crack tip. Intuitively, since the amount of material available for plastic deformation would increase or decrease with thickness, the stress intensity factor would be expected to scale linearly with the thickness. A drop in the K_c has been observed beyond a certain threshold thickness, t^* , as can be seen in Figure 10.a. The material is in a state of plane stress below t^* , where the through-thickness stress (z -direction, $\sigma_z = 0$ MPa) would be zero. The strain, however, would be non-zero, as the material would be free to contract in the z -direction. A bi-axial stress state is set-up, driving the plastic flow towards free surfaces and leading to formation of fracture surfaces inclined at an angle of 45° to free surface. As the thickness increases, the material transitions from being in a state of plane stress to plane strain. The material in plane strain is not free to contract freely anymore

due to the constraint imposed by adjacent material, setting up a high tri-axial constraint (The surfaces would still be free to contract and hence be in plane stress). The transition, resembling a cone, is shown in Figure 10.b. This constraint reduces the drive towards plastic flow, making energy available for a brittle fracture. For K_c to be a material property, it is important to maintain the material in a state of plane strain, as it does not change with increase or decrease in thickness.

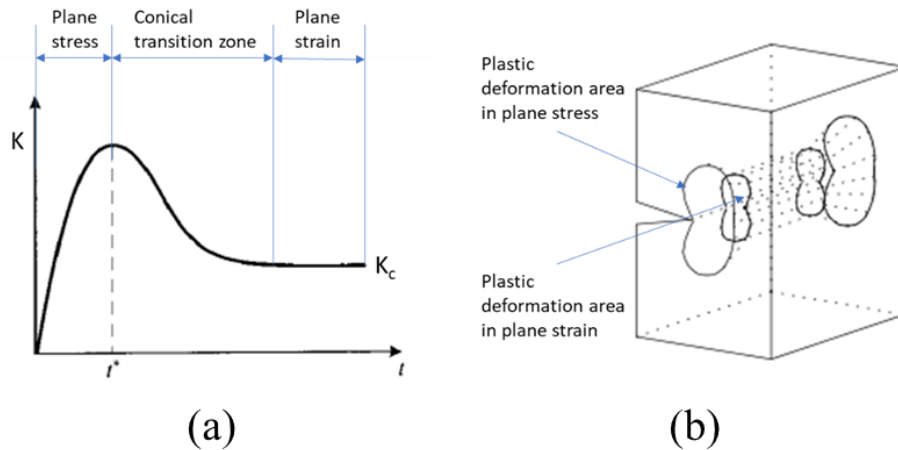


Figure 10: (a) Influence of thickness on critical stress intensity factor (Roylance, 2001) (b) Conical transition from plane stress to plane strain (Schreurs, 2012)

2.2.3 Energy-based approach

While the stress-intensity approach is very useful in engineering practice, it is mathematically very tedious and provides little insight into the actual fracture process. Therefore, rather than focusing on the crack-tip stress concentrations, another group of researchers employed energy-balance arguments. This approach considers the amount of energy absorbed or dissipated in the creation of damage and helped overcome numerous disadvantages of the stress-intensity approach. The same is explained in the next subsections.

2.2.3.1 Griffith's theory of brittle fracture

The energy-based approach was pioneered by Griffith (Sanford, 2003, Roylance, 2001). Numerous simplifying assumptions were made as a starting point. Griffith assumed that all materials contain a finite population of fine cracks and some of these cracks are most unfavorably oriented with respect to the loading direction. This helped Griffith by-pass detailed stress analysis around all arbitrary flaws (provided that the flaws did not interact with each other). Another assumption was that one of the unfavorably oriented cracks grows once the theoretical strength is reached and the crack continues to grow as long as enough strain energy is released for new surfaces to be formed. This assumption conveniently helped Griffith avoid statistical treatment.

Following from the above assumptions, Griffith employed an energy balance approach (Roylance, 2001, Sanford, 2003). When a crack grows by distance 'a', the strain energy of the material adjacent to the crack is released. The now-unloaded material was idealized as triangular flanks (Figure 11.a). This released strain energy (U) was calculated as a product of strain energy per unit volume (assuming linear behavior) and volume of unloaded material (V), as in Equation 2. However, for the crack to propagate, the material must cleave. This implies that the liberated energy must be absorbed by the material to break the bonds and create new surfaces (Equation 3), where γ is the surface energy (J/m^2) and a factor of 2 is needed since two surfaces are formed. The energy balance is expressed in Equation 4. As long as the liberated energy exceeds surface energy, the crack will continue propagating ahead.

$$U = -\left(\frac{1}{2}\sigma\varepsilon\right)V = -\left(\frac{\sigma^2}{2E}\right)\pi a^2 \dots (2)$$

$$S = 2\gamma a \dots (3)$$

$$\Delta U = U + S = -\left(\frac{\sigma^2}{2E}\right)\pi a^2 + 2\gamma a \dots (4)$$

As can be seen in equation 3 and Figure 11.b., over a certain threshold value of crack length (a_c), the strain energy liberated will be much higher than the absorbed surface energy. A fast fracture will then ensue. The stress at which the fast fracture (σ_f) will occur can be determined by setting the first differential of equation 3 to zero (Equation 5). Equation 5 is valid for a plane stress state. Plane strain requires consideration to the resistance to the contraction, and hence inclusion of the $(1-\nu^2)$ term, as in equation 6. Further, it is important to note that increase in crack length is an absolute term and independent of the body it is contained in. The strain energy released is proportional to the increment in crack length. It is also the reason why smaller bodies tend to be stronger, they are too small to contain the critical crack length.

$$\sigma_f = \sqrt{\frac{2E\gamma}{\pi a}} \dots (5)$$

$$\sigma_f = \sqrt{\frac{2E\gamma}{(1-\nu^2)\pi a}} \dots (6)$$

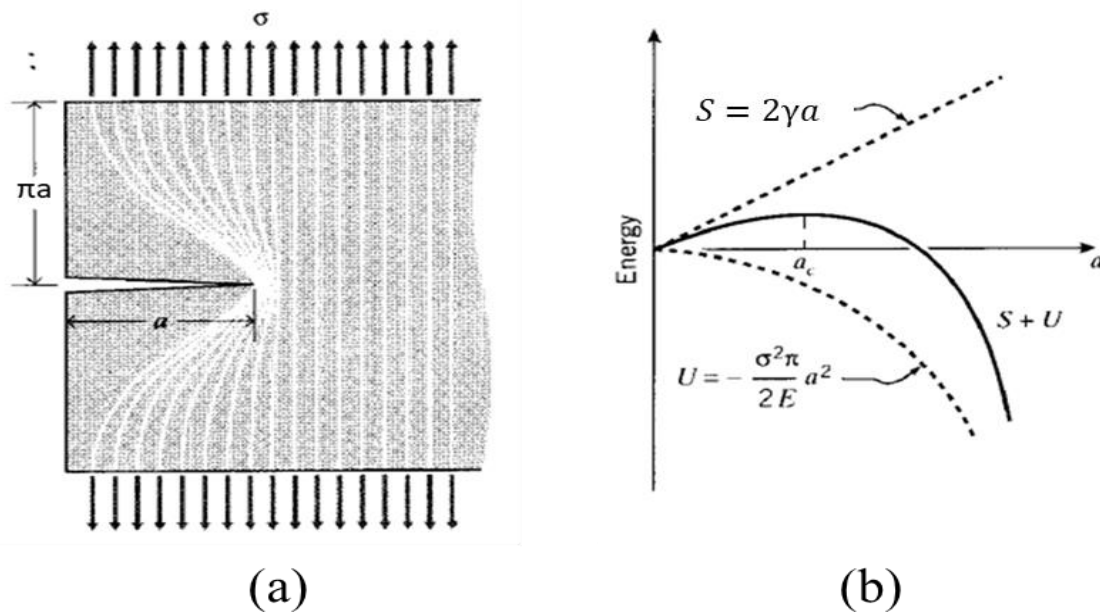


Figure 11: (a) Released strain energy adjacent to the crack (Roylance, 2001) (b) Energy balance (Roylance, 2001)

2.2.3.2 Orowan's extension and a unified theory of fracture

Griffith's theory helped conveniently overcome the singularity stress and mathematical tediousness issues of the stress-intensity approach. His theory, however, was severely restricted to brittle materials, where plastic deformation or other energy absorption mechanisms have a negligible contribution as compared to new surface creation. The theory was hence almost exclusively applicable to ceramics. In mid 1950s, another researcher named Orowan (Sanford, 2003) argued that in highly ductile materials, the contribution of plastic deformation to total energy absorption exceeds surface energy by multiple orders of magnitude. He replaced the ' γ ' term in equations 5 and 6 by ' $\gamma + \gamma_p$ ', where ' γ_p ' is the plastic work.

This extension was further generalized by Irwin to collect all sources of energy absorption into one term ' G_c ', critical strain energy release rate, to give equations 7 and 8 under plane stress and plane strain conditions respectively. The critical strain energy release rate and critical stress intensity factor are hence related as in equations 9 and 10 for plane stress and plane strain conditions respectively.

$$\sigma_f = \sqrt{\frac{EG_c}{\pi a}} \dots (7)$$

$$\sigma_f = \sqrt{\frac{EG_c}{(1 - \nu^2)\pi a}} \dots (8)$$

$$K_c^2 = EG_c \dots (9)$$

$$K_c^2 = \frac{EG_c}{(1 - \nu^2)} \dots (10)$$

2.2.3.3 Contributions to the work of fracture in composites

The concept of critical strain energy release rate (G_c) was introduced in the previous section. The commonly observed sources to the G_c in composites, beyond plastic deformation and energy for surface creation, will be discussed in this section.

Damage in the matrix is often observed at even low levels of loading in composites. The matrix material may either crack or plastically deform depending on the chemical nature of the matrix material and loading condition. Matrix cracks in off-axis plies (Figure 12.a.) are often the first forms of primary damage observed in continuous fiber reinforced composites (including NCF composites) under tensile loads, as the matrix is more compliant than the reinforcing fibers. The resin rich regions caused by the presence of stitching sites have been observed to have an effect on the location of cracks in NCF composites (Mikhaluk, Truong, Borovkov, Lomov, & Verpoest, 2008; Truong, Vettori, Lomov, & Verpoest, 2005). A crack in thermoset matrix with a rigid structure typically span the entire width and thickness of the plies with limited plastic deformation. Depending on the geometric parameters of a composite test coupon, energy is absorbed in creation of multiple cracks in the coupon with a thermoset matrix. Thermoplastics, on the other hand, may exhibit higher degree of energy dissipation in plastic deformation. As the materials fail by yielding of the matrix under compressive loads (explained in greater detail later), energy is dissipated in matrix deformation in composites loaded in compression. The extent of plastic deformation in the matrix depends on both, the chemical nature of the matrix (if it is a thermoset or thermoplastic) and also the reinforcement phase. The presence of stiff reinforcing fibers inhibits the free plastic flow of the matrix, constraining the degree of plastic deformation (Hull & Clyne, 1996).

Another critical damage mode responsible for extensive stiffness losses in composites is delamination. A mismatch between the elastic moduli and Poisson's ratios between different layers in a laminate may lead to out-of-plane interlaminar stresses, which lead to delamination cracks (Figure 12.a.), which assume a critical place in the energy absorption characteristics and design of laminates. Delamination may also be formed when the matrix cracks join, causing reductions in strength. The formation of delamination cracks is strongly influenced by geometric effects, defects and phase constitution (Wisnom M.

R., 2012; Kahla, 2019). The contribution of the delamination crack to overall work of fracture depends strongly on the matrix type and loading mode (Bruce, 2011; Greenhalgh E. S., 2009). The failure surface of a brittle thermoset resin is characterized by a smooth surface under Mode-I loads. A Mode-II failure surface of a thermoset, on the other hand, is characterized by ‘hackles’ and multiple secondary cracks through the resin. Hackles are also the primary energy absorbing mechanisms in thermoplastic matrices with suitable constraints on the plastic flow in the matrix. A surface with hackles has a rough, saw-like appearance. Hackles are formed due to coalescence of multiple inclined microcracks ahead of the crack tip (Figure 12.b.). This increases the effective length of delamination and hence, an increased contribution to the work of fracture.

The catastrophic failure of composites often occurs due to the breakage of stiff reinforcing fibers in composites, as they are the load-bearing components. Although most of the commonly used fibers like carbon fibers, glass fibers, etc. are brittle, the contribution of fiber breakage, especially when multiple fibers break simultaneously, to the overall work of fracture may be significant. Some of the natural fibers and thermoplastic fiber-based fibers may exhibit a higher degree of plastic deformation prior to breakage and absorb a higher amount of energy than the brittle fibers (Hull & Clyne, 1996).

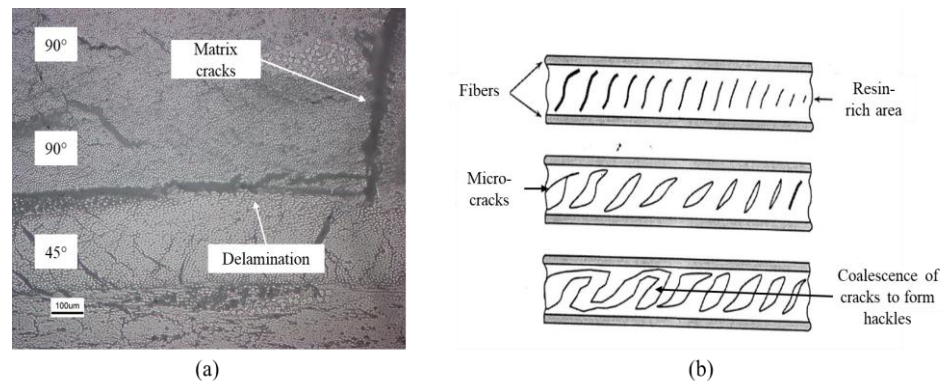


Figure 12: (a) Matrix cracks and delamination in continuous fiber reinforced carbon fiber epoxy composites (b) Process of hackle formation in composites (Bruce, 2011)

Other than the aforementioned three commonly observed primary energy absorbing mechanisms, modes like fiber/matrix debonding and fiber pull-out may also make substantial contributions to the work of fracture (Hull & Clyne, 1996). A debonding crack occurs when a crack front propagating normal to the reinforcing fibers gets deflected at the fiber/matrix interface. Fiber pull-out refers to the ‘pull-out’ of fibers from their resin sockets. The amount of energy absorbed in these modes depends on various factors such as aspect ratio of fibers, fiber/matrix adhesion, contact pressure at interface, roughness of fibers, etc. The prediction of fracture energies associated with these modes also requires taking into account the probabilistic effects, primarily the variabilities in fiber strengths and locations of fiber breaks.

2.2.4 Damage monitoring techniques for composites

As was outlined in the previous section (Section 2.2.3.3), damage may exist in the form of several different modes in composite materials, which may be a result of the manufacturing processes, or the loads experienced during service. The growth of damage can result in severe degradation of mechanical performance of materials, and at times, complete failure of the commissioned structures. It is therefore important to monitor the presence and growth of damage, and many Non-Destructive Technologies (NDT) have been developed for the purpose. The goal of these technologies is to provide economical and cost-effective possibilities for continuous, in-situ damage assessment. They should be sensitive to even minor levels of damage and capable of detecting different damage modes, while being resistant to external noise.

Despite all the advancements, damage detection and monitoring in composites is still one of the biggest challenges in the composites field and has also been receiving increased attention over the last few years. This is evidenced by the fact that over 60% of the reviewed papers in the field have been published between 2015 and early 2022 (Hassani, Mousavi, & Gandomi, 2022). Some of the common techniques employed for damage monitoring are summarized in this section. A detailed review of the history, development and the state of the art of damage monitoring techniques can be found in a recently published article by Hassani et al (Hassani, Mousavi, & Gandomi, 2022).

Two of the earliest and most commonly employed techniques in damage detection are X-Ray radiography and ultrasonic scanning. Radiography involves injection of a liquid penetrant inside the material, which is subjected to electromagnetic radiations of short wavelengths produced using an appropriate radioactive isotope to obtain the X-Ray image. However, if the liquid penetrant does not sufficiently penetrate through the internal cavities in the material, damage may go undetected. Furthermore, as the technique involves exposure to radiation and toxic chemicals, it poses a potential hazard to the human health and can hence be performed only by trained personnel wearing appropriate protection equipment.

Ultrasonic scanning, on the other hand, entails creating a profile of the material interior by passing ultrasonic impulses through the material. The signals on the receiving side are used to detect internal flaws in the materials. It can, however, be difficult to distinguish different damage modes due to the restrictions on the resolution, governed by limitations on the computing power. Furthermore, while both X-Ray radiography and ultrasonic scanning have been useful in the detection of damage to varying degrees, neither of these can be optimally employed in-situ (Hassani, Mousavi, & Gandomi, 2022; Montesano, 2012).

Numerous in-situ NDTs have been developed over the years to overcome the drawbacks of X-Ray radiography and ultrasonic scanning like light microscopy, infrared thermography, acoustic emission, edge replication, etc. Light microscopy technique involves illuminating one surface of the specimen and capturing the images of the light penetrating through the specimen at the opposite surface. Although this technique is simple, does not require specialized equipment and is effective in visualization of cracks in the materials, its usage is limited to sufficiently transparent material systems (Montesano, 2012). Digital Image Correlation (DIC) has also been utilized as a NDE technique for damage monitoring, wherein the changes in local strains due to crack formation are used to gauge the damage (Tessema, Ravindran, Wohlford, & Kidane, 2018). While the results from this technique are relatively immune to environmental effects, they are strongly dependent on the quality of the speckle pattern.

One of the well-established NDT is Acoustic Emission (AE), which operates on the principle of passively monitoring the sounds of damage formation. The formation of a fracture surface is coupled with the release of elastic energy as a stress wave. The motion of this wave is detected using piezoelectric sensors coupled to the specimen surface and is indicative of damage formation and evolution in the materials. However, in the cases where multiple interacting failure modes occur simultaneously in the material, it is difficult to isolate the acoustic signals and make direct correspondences between different damage events (Black, 2008).

Infrared thermography is another popular non-contact NDT. The specimen surface is heated with a brief, spatially uniform light pulse in this technique. An infrared camera is used to create a time-dependent temperature profile of the specimen with respect to the incident thermal impulse. As the incident heat wave travels through the material, deviations occur when the wave encounters cracks, which are recorded by the infrared camera. The time delay associated with the deviations allows measurement of the depth at which the flaws are present (Shepard, 2007). Alternatively, the thermography technique may also be used passively to monitor the release of heat energy upon damage formation in the materials (Montesano, 2012). The quality of the results from this technique may, however, be dependent on the ambient conditions.

Edge Replication (ER) is another well established in-situ NDT (Montesano, 2012). This technique involves taking a local imprint of the microstructure of the specimen at various levels of loading using a replicating tape. The imprint of the microstructure is then observed using a microscope. This technique provides a fast and cost-effective possibility for in-situ assessment of damage. Specimen interior, however, cannot be investigated with this technique. This NDT was employed for damage assessment in this study and is discussed in greater detail in Section 4.3.2.

2.3 Mechanical characterization of and damage in continuous fiber reinforced composites

Previous section (Section 2.2) was focused on providing a background of damage in materials. This section provides a literature review of the aspects relevant to the central investigation in this study – characterization of engineering properties and damage in the NCF composites under quasi-static loads. Firstly, a review of studies characterizing the mechanical response of NCF composites and comparing the NCF composites to prepregs is provided. Next, studies related to initiation and propagation of damage in both, unidirectional lamina and multidirectional laminates, until failure under quasi-static tension and compression are reviewed, with a focus on experimental investigations on NCF composites.

2.3.1 Quasi-static mechanical characterization

2.3.1.1 Tension and compression testing

Numerous experimental studies (Bru, Hellström, Gutkin, Ramantani, & Peterson, 2016; Vallons, 2009; Mattson, 2005) have been conducted over the past decades which characterize the mechanical response of NCF composites under quasi-static loads. Several studies have also been conducted to compare the properties of the NCF composites to their competitor materials such as UD prepreg materials (Bibo, Hogg, & Kemp, 1997; Godbehere, Mills, & Irving, 1994; Dexter & Hasko, 1996; Backhouse, 1995). The tensile and compression properties were not influenced by the stitching patterns in the NCF composites (Asp, Edgren, & Sjögren, 2004). The absence of major difference between classical laminate theory predictions, which exclude the effect of stitching fibers, and experimental results further confirm the negligible effect of stitching threads on mechanical properties (Truong, Vettori, Lomov, & Verpoest, 2005). The tensile strengths, however, were almost twice that of the compression strengths (Asp, Edgren, & Sjögren, 2004; Vallons, 2009) and the tensile stiffness was reported to be about 10% higher than the compressive stiffness (Vallons, 2009).

The tensile and compressive properties of NCF composites were found to be generally lower than equivalent UD prepreg composites. There was, however, an inconsistency in the degrees to which the strengths and stiffnesses of the NCF composites are lower than the preregs. A 1%-35% (Bibo, Hogg, & Kemp, 1997; Godbehere, Mills, & Irving, 1994) drop in the tensile strength and a drop in the range of 3%-10% in the tensile stiffness (Godbehere, Mills, & Irving, 1994) of NCF composites has been reported.

The influence of architecture was more pronounced on the measured compressive properties than the tensile response. The compressive strengths and stiffnesses of NCF composites are generally lower, reportedly 6%-38% (Backhouse, 1995; Dexter & Hasko, 1996), than the equivalent preregs due to the local bundle waviness induced by stitching sites in the NCF composites. A contradictory increase in the compressive stiffness of NCF composites was reported by Godbehere et al (Godbehere, Mills, & Irving, 1994). No significant difference, however, was reported between the measured axial compression strengths of NCF composites and woven fabric composites (Vallons, 2009).

Quasi-static tensile tests on NCF carbon fiber/epoxy composites at room temperature and elevated temperatures were conducted by Vallons (Vallons, 2009). It was concluded in the study that only the stiffness of the composites in the matrix dominated transverse loading direction degraded at elevated temperatures. Damage initiation was also found to be at higher strains at higher temperatures. The effect of temperature on fiber dominated directions was negligible. The effect of voids is also pronounced in the matrix dominated testing directions (Sisodia, Gamstedt, Edgren, & Varna, 2015).

Furthermore, experimental investigation of NCF angle-ply composites revealed a non-linear “S-shape” stress-strain response. The tangent modulus increased until a certain value of strain and then decreased monotonically until failure. This was attributed to carbon fiber stiffening, fiber straightening and gradual damage development. Mechanisms like matrix damage and tow scissoring at fiber/matrix interface were found to come into play at lower strains under ± 45 bias loading which caused an abrupt drop in modulus (Bogdanovich, Karahan, Lomov, & Verpoest, 2013).

The compression strengths of the NCF composites in the fiber-dominated directions are highly sensitive to the fiber misalignments (Wisnom M. R., 1993; Wilhelmsson D. , 2019). It was shown through Finite Element Analysis that an increase in the misalignment from 0.75° to 8° reduced the compression strength from 1949 MPa to 400 MPa. The stacking sequence, unlike in tension, also has a noticeable influence on the compression strength of the laminate. Higher strengths are reported for specimens containing central load-bearing plies supported by weaker off-axis plies (Leopold, et al., 2017).

2.3.1.2 In-plane shear testing

There has been a great variety of test methods developed and in use for in-plane shear characterization of composites over the last few decades. The key reasons for the development of multiple test methods are the difficulty in obtaining a pure and uniform shear stress state in the test specimen and testing of high strain-to-failure materials (Crossan, 2018; Adams, 2009). The different test methods commonly in use are summarized in Figure 13 and are discussed in detail in a dissertation by Crossan (Crossan, 2018). The two most promising shear test methods, Iosipescu test and V-Notched Rail Shear test, were evaluated in detail by Crossan (Crossan, 2018). It was concluded that both the test methods can deliver accurate results for composites and the choice of shear test depends on the end constraints of the specimens, depending on if matrix- or fiber-failure is expected in the application.

Test Method (with ASTM Std. No., if applicable)	Uniform Shear Stress State	All Three Stress States Practical	Shear Strength Obtained	Shear Stiffness Obtained
Short Beam Shear (D 2344)				
Iosipescu Shear (D 5379)				
$\pm 45^\circ$ Tensile Shear (D 3518)				
Two-Rail Shear (D 4255)				
Three-Rail Shear (D 4255)				
Double-Notched Shear (D 3846)				
Torsion of a Thin Tube (D 5448)				
Cross-Beam Sandwich				
Torsion of a Solid Rod				
Four-Point Shear				
Picture Frame Shear				
Plate Twist				
10° Off-Axis (Tensile)				
V-Notched Rail Shear (D 7078)				

Figure 13: Comparison of available shear test methods (Adams, 2009)

Very limited number of studies could be found in the literature related to characterization of in-plane shear of NCF composites. The in-plane shear response of NCF composites during an Iosipescu test is characterized by failure at the roots of the notches by splitting, followed by failure in the gauge section (Bru, Hellström, Gutkin, Ramantani, & Peterson, 2016).

2.3.1.3 Interlaminar fracture toughness testing

Several studies have been conducted on experimental measurement of Mode-I fracture toughness of composites over past few decades. The Mode-I fracture toughness (G_{Ic}) of unidirectional composites has typically been measured in the range of 150-500 J/m² (Bru, Hellström, Gutkin, Ramantani, & Peterson, 2016; Vallons, 2009; Alfred Franklin & Christopher, 2013; Bruce, 2011; Reis, Ferreira, Antunes, Costa, & Capela; Ferrarese, 2020; Robinson & Song, 1991). The measured G_{Ic} values have been reported to be influenced by various parameters such as test coupon geometry, stacking sequence, reinforcement architecture, loading rate, etc.

Specimen geometry is a prominent factor in the measurement of the Mode-I fracture toughness. First and foremost, the two arms in a Double Cantilever Beam (DCB) test must be equally stiff to assure pure Mode-I conditions. Deviation of the crack from the mid-plane or matrix cracking, as is commonly observed with multidirectional specimens due to the stress-state at the tip of crack front (Greenhalgh, Rogers, & Robinson, 2009), may induce a local Mode-II component (Gong, Hurez, & Verchery, 2010). Robinson et al. (Robinson & Song, 1991) proposed a modified DCB specimen containing a non-adhesive Teflon insert along the entire edge to suppress crack jumping. A wide enough edge crack insert was found to be effective in confining the delamination crack front on the mid-plane.

The influence of initial crack length in woven carbon fiber-epoxy laminates was numerically studied by Reis et al (Reis, Ferreira, Antunes, Costa, & Capela). An increase in the initial crack length was found to decrease the stiffness of the specimen, but no prominent influence on the nature of damage progression was reported.

Data reduction methods for G_{Ic} calculations assume a quasi-uniform distribution of G_I across the width of the specimen. However, the distribution of the G_I values across the width of the specimen have been reported to be dependent on the laminate coupling terms and aspect ratio, defined as the ratio of crack length to width (Davidson, 1990; Sun & Zheng, 1996). The G_I values are reported to be the lowest at the free edges of the specimen and highest at the centre. The non-uniformity of the toughness can be attributed to the change of stress-state across the specimen width from plane stress to plane strain. This is governed by non-dimensional ratios $D_c (= (D_{12})^2/D_{11}D_{22})$ and $B_t (=D_{16}/D_{11})$, as defined by classical laminate theory. Additionally, the maximum G_I was found to shift from the center to edges with an increasing specimen width (Gong, Hurez, & Verchery, 2010). Further, as the crack initiates from the non-adhesive insert into matrix-rich zone and propagates primarily through resin along fiber-matrix interface, the toughness of the matrix may also affect the measured fracture toughness of the composites (Bradley, 1989; Bradley, 1991).

Shokrieh et al (Shokrieh, Salamat-talab, & Heidari-Rarani, 2016) investigated the role of interface angle on the fracture properties of composites by conducting DCB tests. Interface angles of 0//0, 0//30, 0//45 and 0//90 were investigated in this study. An increase of about 18%, 13% and 12% in measured G_{Ic} was reported for 0//30, 0//45 and 0//90 interface angles respectively as compared to 0//0 interface. The fiber bridging length was found to decrease with an increase in fiber interface angle.

The reinforcement architecture also has a pronounced effect on the measured G_{Ic} . The toughness of the woven fabric composites was reported to be 50% more than the NCF composites, based on the same material system (Vallons, 2009). The reason was attributed to the path followed by crack. The nesting of fibers in woven composites forces the crack to take a wavy path against a largely linear path in unidirectional NCF composites, and requires higher amount of energy.

In a NCF architecture, the presence of nesting is associated with the characteristics of stitching patterns and stitching threads, which lead to larger or smaller resin rich pockets (Bibo & Hogg, 1998). Further, effect of loading rate on fracture toughness of NCF composites was investigated experimentally by (Ferrarese, 2020). The Mode-I interlaminar fracture toughness was reported to decrease with an increase in testing rate.

The Mode-II fracture toughness (G_{IIc}) is usually measured to be 2-3 times higher than the corresponding G_{Ic} for a particular composites system (Bru, Hellström, Gutkin, Ramantani, & Peterson, 2016; Bruce, 2011; Vallons, 2009; Arai, Noro, Sugimoto, & Endo, 2008). The higher fracture toughnesses under Mode-II loads are primarily attributed to the formation of so-called “cusps”.

Brambleby et al (Brambleby, Louca, & Mouring, 2017) investigated the influence of loading rate on the Mode-II response of glass fiber/vinyl ester composites. While the initiation G_{IIc} values increased as the loading rate was raised from 1 mm/min to 6000 mm/min, the propagation values did not exhibit a significant dependence on loading rate. It was further discovered that the interaction between rough fracture surfaces and possible surface debris cause the crack to open slightly at large displacements. This induces a local Mode-I component and makes a contribution in the measured Mode-II fracture toughness values. The tendency of the cracks to open was not apparent at smaller displacements.

The Mode-II fracture toughness is found to increase with a higher interface angle in multidirectional composites (Pereira & de Morais, 2004; Pereira, de Morais, Marques, & de Castro, 2004). However, presence of elastic couplings may lead to non-uniform G_{II} distribution across the width leading to a skewed delamination front. The presence of bending-extension and bending-twisting elastic couplings was confirmed by the presence of Mode-I and Mode-III features in fractographic observations (Rzeczowski, 2021).

2.3.2 Damage in composites under tension

2.3.2.1 Unidirectional lamina

Failure of the unidirectional composites under axial tension has been the focus of the scientific community for several years owing to the significance of this failure mode on the final catastrophic failure. Observation techniques such as scanning electron microscopy, fractography and high-resolution computed tomography reveal a failure process of localized nature in fiber clusters. Single fiber breaks have been reported at low loads, followed by breakage of neighboring fibers as load increases till the cluster of broken fibers reaches a certain threshold (N^*) close to failure. The formation and unstable growth of this “critical fracture plane” leads to the failure of the composite. The sequence of events is shown in Figure 14.

The fiber breaks were found to occur independently of each other (Raz-Ben Aroush, et al., 2006; Talreja, 2016). Numerous models have been developed to describe the statistical nature of the fiber breakage process, which are neatly summarized by Zhuang (Zhuang, 2018).

The role of matrix cracks between the fiber breaks was investigated by Zhuang et al (Zhuang, Talreja, & Varna, 2016) using a 2-D finite element model. A matrix crack was found to grow perpendicular to the fiber axis, in a case where the broken fiber was a result of the manufacturing process. On the other hand, fibers were found to debond over a length, and the cracks were found to kink out in the matrix towards the neighboring fibers, when the fiber break was a resultant of applied load. Highest stress magnification was reported where the matrix crack front reached the fibers.

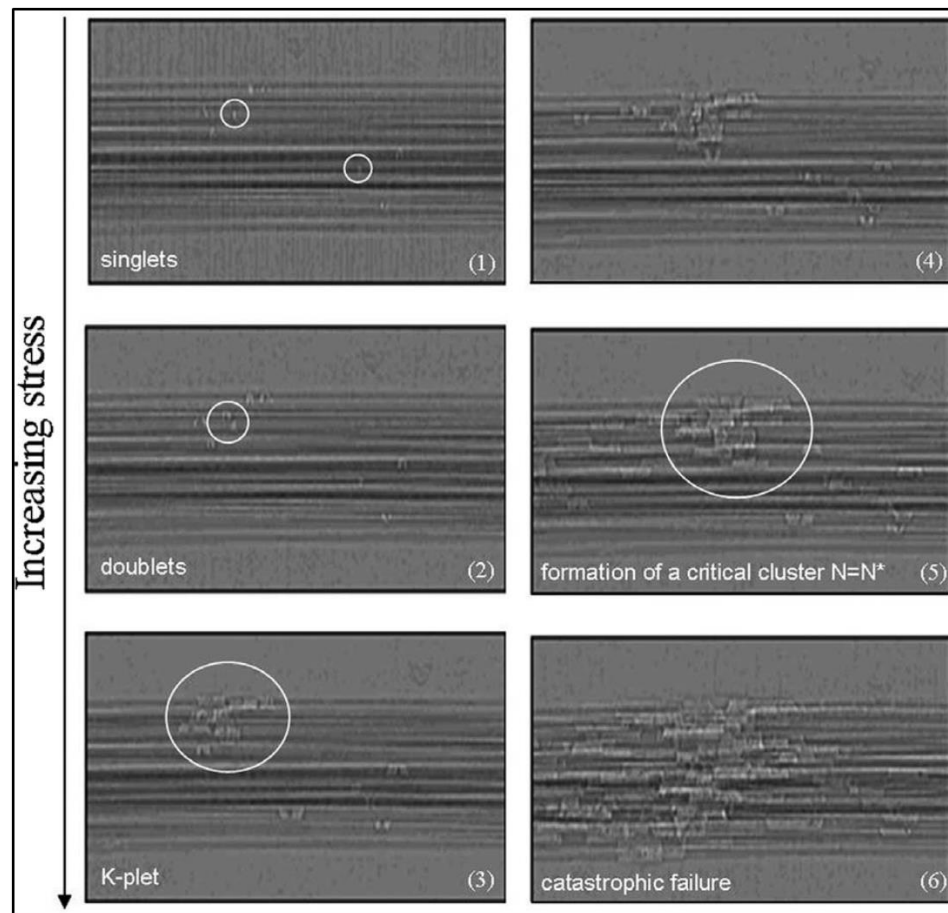


Figure 14: Sequence of events leading to failure in unidirectional composites under axial tensile loads: (1) Single fiber breaks (2-4) Breaks in neighboring fibers (5) Critical cluster of broken fibers (6) Catastrophic failure (Raz-Ben Aroush, et al., 2006)

Transversely loaded unidirectional lamina fail either by tensile failure of the matrix or fiber-matrix debonding (Agarwal, Broutman, & Chandrashekhara, 2015). Similar to the axial loading case, the unstable nature of the failure makes it challenging to understand the failure process in this loading case. It is, therefore, common to study them in a constrained environment, like in a cross-ply laminate.

The micro-mechanisms leading to failure in a transverse ply were studied experimentally by Gamstedt et al (Gamstedt & Sjögren, 1999). In-situ microscopy images (Figure 15) revealed damage initiation in the form of fiber-matrix debonding. As the material was further loaded, the debonds coalesced to form a transverse crack.

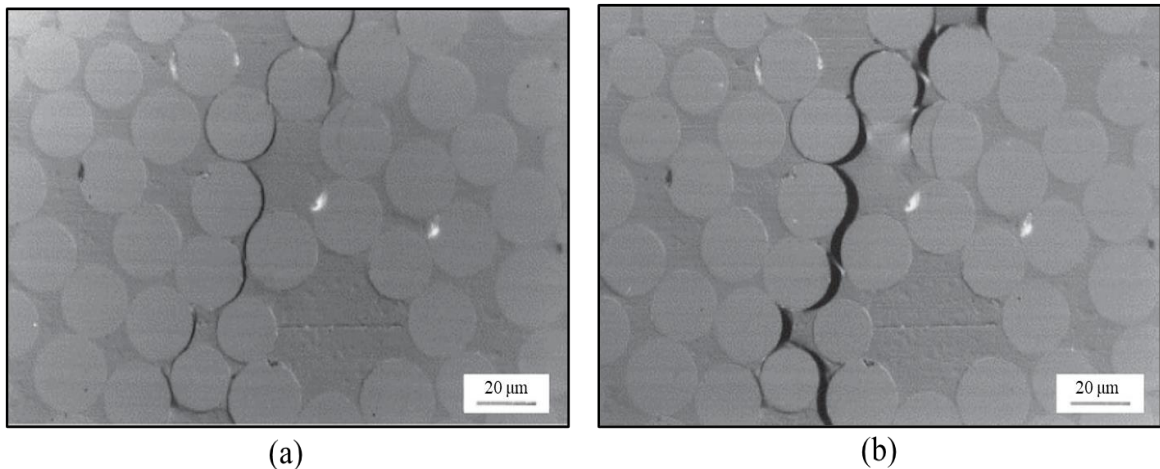


Figure 15: (a) Damage initiation in the form of interface debonds (b) Coalescence of debonds into transverse cracks (adapted from Gamstedt & Sjögren, 1999)

2.3.2.2 Multidirectional laminates

The studies on multidirectional laminates are focused on predicting the initiation and propagation of damage, primarily the cracking in transverse and/or off-axis plies and delamination, on application of a progressive tensile load.

Cracking in transverse plies under uniaxial tensile loads has extensively been studied numerically in the literature, right from 1980s (Boniface, Smith, Bader, & Rezaifard, 1997; Llobet, Maimí, Essa, & Martín de la Escalera, 2019; Talreja, 1985). Earlier models predicting the degradation in stiffness after the onset of ply cracking involved developing analytical expressions for ply-level stresses. These models were based on shear-lag approach (Ogihara & Takeda, 1995), variational approach (Liu & Nairn, 1992) or on other stress-transfer methods (McCartney, 1998). These analytical models, though, had some drawbacks. They were all based on and highly focused on cracking in cross-ply laminates, and hence failed to consider simultaneous cracking in multiple plies. They also demonstrated a limited accuracy with regards to the ply constraining effects. Their adaptation was also further constrained by their complexity and limitations with respect to their implementation in Finite Element Software.

Continuum models (Varna, 2015) are an improvement over the previous approaches in this regard. They involve development of models based on defining local stresses between ply cracks as damage parameters, predicting the degradation of stiffness with evolution of cracks in the composites. A strong link exists between local stresses between the cracks and the crack-opening and crack-sliding displacements (CODs and CSDs).

A micromechanical approach was employed by Montesano et al (Montesano, McCleave, & Singh, 2018; Montesano & Singh, 2015) to develop general expressions for COD and CSD for different plies. Normalized average COD and CSD expressions were obtained by fitting average COD and CSD (may be determined using Finite Element schemes or shear-lag or variational approaches) vs crack density data. Failure mode specific coefficients, which accounted for stacking sequences and ply properties, were then integrated into the expressions. Damage-stiffness relation was then used, in which damage parameters (containing the COD/CSD expressions) were subtracted from stiffness properties of undamaged laminate, to relate stiffness degradation to ply cracks.

It is often beneficial to combine the developed COD/CSD expressions with an energy-based approach to predict evolution of damage with increased stress. The presence of a flaw and the growth of it forms the crux of this approach. It accounts for variations in ply cracking strains at different ply thicknesses, as opposed to the strength-based approach. An energy-based assessment of crack multiplication process in multidirectional composites subjected to axial tensile loads was performed by Singh et al (Singh & Talreja, 2010). The constraint applied on CODs of off-axis plies by surrounding plies and total thickness of the off-axis plies was found critical in damage evolution process.

A global-local (GLOBLOC) approach could also predict the stiffness degradation in composites. The degradation of laminate properties is predicted by determining the crack density and the microdamage parameters (COD and CSD). A strength-based approach was used for thicker layers and fracture toughness approach for thinner layers. Exact expressions were used for thermal and stiffness components, while empirical approximations were used for COD and CSD expressions (Varna, 2013).

In-situ experimental observations using DIC (Tessema, Ravindran, & Kidane, 2018; Tessema, Ravindran, Wohlford, & Kidane, 2018) confirm that the first form of damage in quasi-isotropic laminates is in the form of matrix cracks in the transverse plies. New cracks continue to form in the transverse and off-axis plies as the material is loaded. The new crack was observed to form usually between two pre-existing cracks in a particular ply. The damage initiation was delayed in the thinner plies owing to an enhanced in-situ strength. Furthermore, the cracks were found to multiply slower in thicker plies. The cracking characteristics were also reported to be influenced by the stitching threads (Sakai, Wakayama, Pérez-Pacheco, Rodriguez-Laviada, & Rios-Soberanis, 2013), resin-rich zones (Mikhaluk, Truong, Borovkov, Lomov, & Verpoest, 2008) and void content (Carraro, Maragoni, & Quaresimin, 2015) in the NCF composites.

Four types of transverse cracks were found to occur in NCF cross-ply laminated composites by Edgren et al (Edgren, Mattsson, Asp, & Varna, 2004), the distinguishing features of which are shown in Figure 16. The “half cracks” were found to occur first. They initiated at strains of about 0.4%, whereas the other types of cracks initiated at strains higher than 0.5%. The cracks extending in the loading direction along the tow boundaries, namely the “longitudinal cracks” and the branches of “double cracks”, are very specific to NCF composites. Finite element studies revealed that the longitudinal cracks occur due to stress concentrations caused by the straightening of the fibers in the adjacent 0° layers.

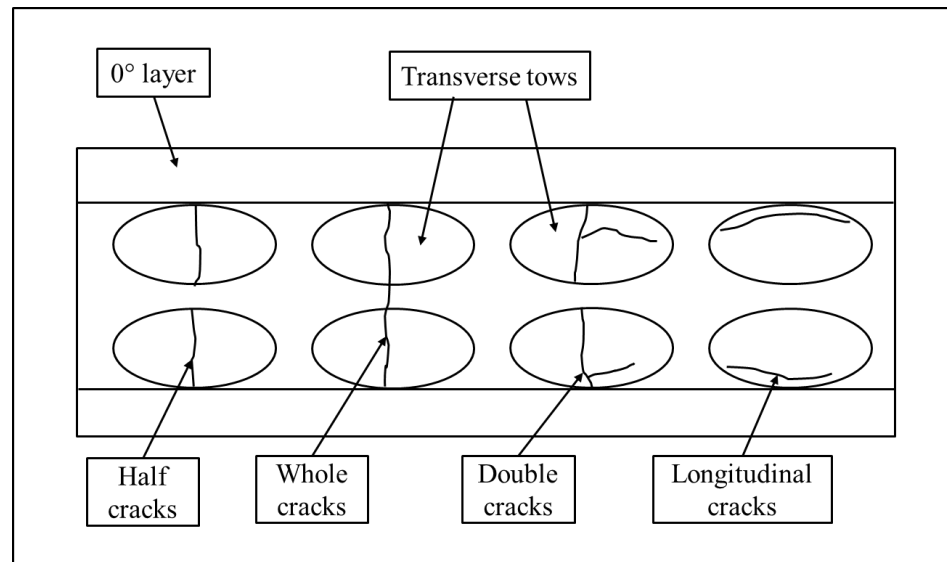


Figure 16: Types of transverse cracks observed in NCF composites under tensile loads (adapted from Edgren, Mattsson, Asp, & Varna, 2004)

It was further observed by Tessema et al (Tessema, Ravindran, & Kidane, 2018) that the transverse cracks have a tendency to propagate in the adjacent plies. The transverse cracks induce cracks in the adjacent plies, if the adjacent plies and the interface between the plies are compliant too. In case the adjacent plies were stiff, like 0° plies, a delamination growth was observed at the interface between plies.

Furthermore, the crack density and the rate of crack multiplication was found to be dependent on the stacking sequence in other studies (Shen, Yao, Qi, & Zong, 2017; Guillamet, Turon, Costa, & Renart, 2014; Mattsson, Joffe, & Varna, 2008). Mattsson et al (Mattsson, Joffe, & Varna, 2008) compared the drop in stiffness due to tensile loads in two cross-ply layups: [0/90/0/90]_s (lay-up A) and [90/0/90/0]_s (lay-up B). A much more significant drop in the modulus in lay-up A (about 40%) than in lay-up B (about 5%). The steeper drop was attributed to the extensive delamination along 0/90 interface and fiber breaks in the 0° plies, in addition to transverse cracks, in lay-up A. It was hypothesized in the study that a greater degree of 0° fiber breaks were observed in lay-up A due to reduced constraints on the surface and the separation of two possibly imperfect 0° plies by 90° plies on the midplane. Although their findings were supported by finite element simulations, the underlying mechanics were unclear.

2.3.3 Damage in composites under compression

2.3.3.1 Unidirectional lamina

Unlike in the case of tensile loading in unidirectional composites, where the failure in unidirectional composites under axial loading is primarily governed by the tensile strength of the fibers, the failure under axial compression is a function of fiber misalignment and shear failure in the matrix (Wilhelmsson, 2019; Wisnom, 1990; Argon, 1972).

At very low fiber misalignment angles (i.e., less than 2°), the composites fail by failure of the reinforcing fibers in shear mode at an angle of 45° to the loading axis, which is referred to as fiber shear failure mode (Figure 17.a.) or fiber crushing (Gutkin, Pinho, Robinson, & Curtis, 2010; Gutkin, Pinho, Robinson, & Curtis, 2010; Agarwal, Broutman, & Chandrashekhara, 2015). The lateral support provided by the fibers is very high in case of low misalignment angles, and the composite approaches the theoretical compressive strength. In-situ microscopic observations on notched specimens confirmed minimal effect of shear stresses in the matrix in the composite failure. Significant debris and abrasion has been reported on the surfaces of the shear driven compressive failure surfaces of carbon fiber reinforced epoxy composites (Ewins & Potter, 1980). This is due to the friction arising from the sliding of the failure surfaces over one another post-failure. In an alternate scenario, the fiber shear mode may also be observed in the composites with a large fiber volume fraction where the interfiber distances are small (Agarwal, Broutman, & Chandrashekhara, 2015) or in composites with large fiber diameters (Wilhelmsson, 2019).

The most commonly observed failure mechanism in a wide range of materials under axial compression, however, is “fiber kinking” (Rosen, 1964; Argon, 1972; Budiansky, Fleck, & Amazigo, 1998). A typical fiber kinking geometry, along with its distinguishing characteristics (width of the kink-band (w), kink-band propagation angle (β) and fiber rotation angle (α)), is shown in Figure 17.b.

The formation of kink bands is mainly governed by the initial fiber misalignment or an initial local fiber imperfection and local shear instability of the matrix material (Gutkin, Pinho, Robinson, & Curtis, 2010; Sun, Guan, Li, Zhang, & Huang, 2017; Wilhelmsson, 2019). Although the unstable nature of the failure makes it challenging to understand the kink-band formation, numerous experimental (Moran, Liu, & Shih, 1995; Soutis, 1991; Edgren, Asp, & Joffe, 2006; Pimenta, Gutkin, Pinho, & Robinson, 2009; Vogler & Kyriakides, 2001) and numerical studies (Pinho, Darvizeh, Robinson, Schuecker, & Camanho, 2012; Prabhakar & Waas, 2013; Pimenta S., Gutkin, Pinho, & Robinson, 2009; Allix, Feld, Baranger, Guimard, & Ha-Minh, 2014; Edgren, Asp, & Joffe, 2006) have been performed over the last decades to understand and simulate the sequence of events in the growth of kink bands.

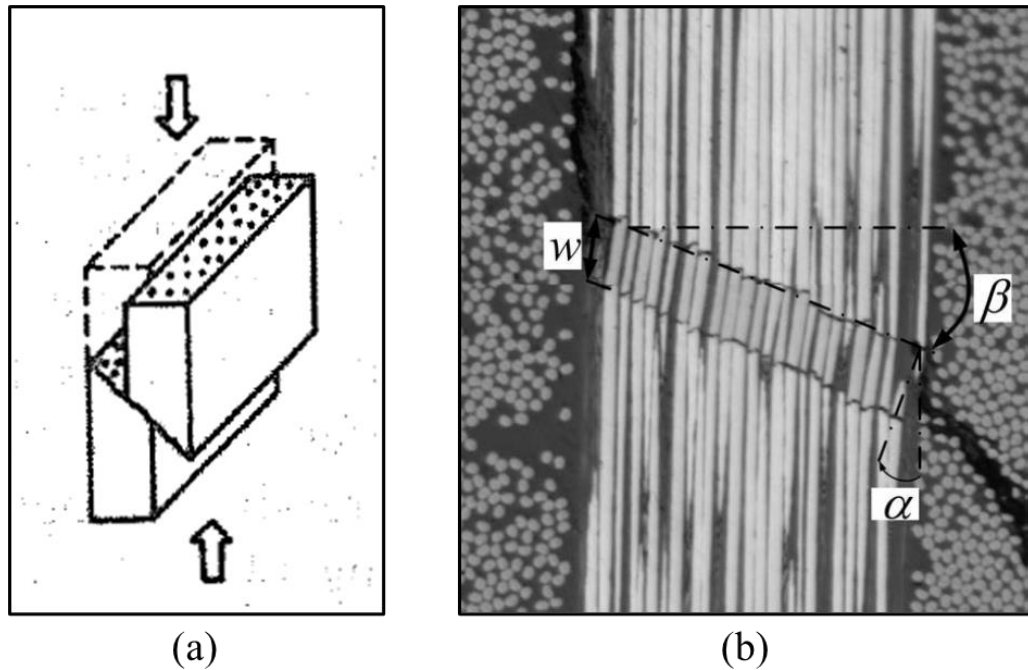


Figure 17: Axial compression failure modes (a) Fiber shear failure (Agarwal, Broutman, & Chandrashekhara, 2015) (b) Typical kink-band geometry (Gutkin, Pinho, Robinson, & Curtis, 2010)

The video tape recordings made by Moran et al (Moran, Liu, & Shih, 1995) revealed the events associated with initiation and propagation of kink bands in composites. Thick notched unidirectional specimens were used in this study. Following the initial linear-elastic response regime, matrix yielding was observed around the notch, which serves as the initiation point for the instability. Along with shear damage in the matrix, axial splits and micro-cracks have also been observed in recent observations using computer tomographs (Wang, et al., 2017). It was also observed that the kink-band propagation angle (β) remains shallow in the initial stages of propagation and reaches its final value (typical $\beta \approx 11-40^\circ$) only after the locally destabilized fibers have undergone an unstable rotation ($\alpha \approx 18-52^\circ$). The sequence of events was confirmed through micromechanical modelling by Pimenta et al (Pimenta S. , Gutkin, Pinho, & Robinson, 2009; Pimenta S. , Gutkin, Pinho, & Robinson, 2009).

Recent real-time X-Ray CT observations of kink-band formation revealed three distinct stages (Figure 18) in fiber displacement leading up to kink-band formation. The observations showed that the fiber displacement starts with an overall tilt of fibers, followed by formation of a knee and eventually a micro-buckle (Wang, et al., 2021).

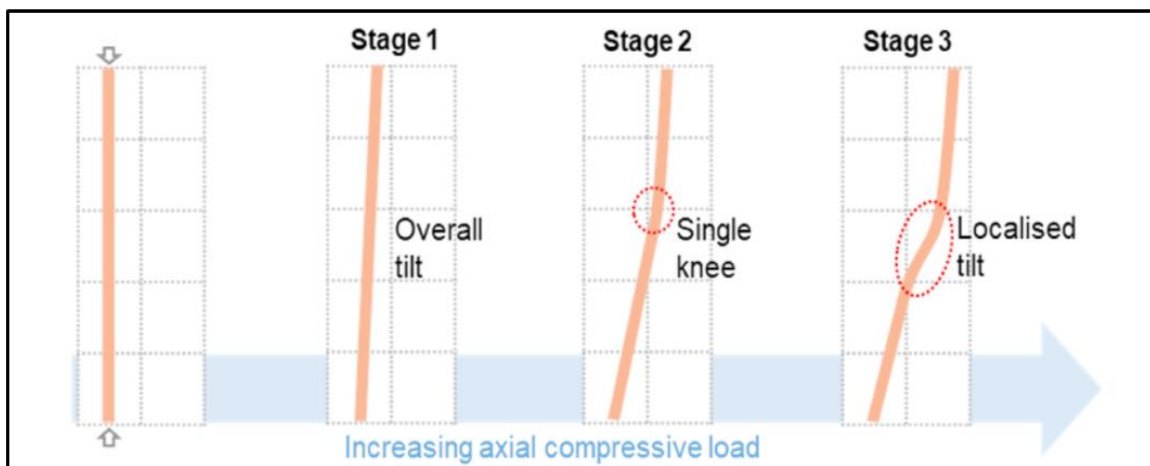


Figure 18: Stages of fiber displacement in kink-band formation (Wang, et al., 2021)

Stable, almost in-plane kink bands were also achieved in other experimental studies (Vogler & Kyriakides, 2001; Pimenta S. , Gutkin, Pinho, & Robinson, 2009; Soutis & Fleck, 1990). The studies confirmed that kink-band formation relies primarily on matrix yielding due to shear stresses and not fiber failure. The peak load is hence governed by local softening due to matrix yielding and not any other type of failure or instability. It was further confirmed that fiber failure, when it occurs, starts in compression first.

The effect of multi-axial loading on the kink-band formation was studied by Basu et al (Basu, Waas, & Ambur, 2006). As compared to the strength measured under pure uniaxial compression, a combined compression-shear loading was found to noticeably affect the composite compressive strength. Depending on the direction of applied shear with respect to the fiber rotation angle, the shear component may either increase or decrease the fiber rotation, effectively either decreasing or increasing the compression strength. Similarly, under biaxial loading, the compressive strength increases with a transverse compression component obstructing the fiber rotation.

Fiber kinking was also found to be the primary failure mode in NCF composites. Several primarily modelling studies have aimed at understanding the influence of the mesoscale heterogeneities on the kink-band formation in this architecture (Edgren, Asp, & Joffe, 2006; Shipsha, Burman, & Ekh, 2018; Joffe, Mattsson, Modniks, & Varna, 2005; Wilhelmsson, 2019; Zrida, Marklund, Ayadi, & Varna, 2014; Cox & Dadkhah, 1995; Olsson, Marklund, & Jansson, 2012).

A finite element modelling analysis was conducted by Joffe et al (Joffe, Mattsson, Modniks, & Varna, 2005) to analyze the influence of out-of-plane tow waviness, tow fiber volume fraction and tow fraction in the composite on initiation of kink-band in NCF composites. The initiation strain was found to decrease with an increase in the out-of-plane tow waviness. The damage was also found to have initiated at a lower strain with an increase in the fiber volume fraction inside a tow from 0.5 to 0.6. However, a change in tow volume fraction (at a constant fiber volume fraction inside the tow) from 0.5 to 0.7 caused the failure to initiate at a significantly lower strain, but the initiation strain value stabilized for volume fractions above 0.7.

The effect of in-plane shear stress on the kink-plane angle in UD NCF composites tested at off-axis angles was studied by Wilhelmsson et al (Wilhelmsson, Mikkelsen, Fæster, & Asp, 2019) using X-Ray Computer Tomography. The kink-plane angle was found to be aligned more in-plane at the free edges where in-plane shear stress was dominant. Further, the kink-plane was oriented out-of-plane when the fibers were oriented along the loading direction. The kink-plane angle increased linearly with a change in off-axis angle from 0° to 20° due to an increasingly prominent in-plane shear stress component.

However, for larger off-axis angles (or large fiber misalignments), two competing failure modes, axial splitting between fiber and matrix and fiber kinking, have been reported. For the axial splitting damage mode, the compression strength is governed by in-plane shear due to sliding between adjacent fiber planes. The threshold off-axis or misalignment angle based on the studies in literature is between 15° and 30° for NCF carbon fiber/epoxy composite systems (Prabhakar & Waas, 2013; Gutkin, Pinho, Robinson, & Curtis, 2010; Shipsha, Burman, & Ekh, 2018).

The unidirectional lamina have been found to fail parallel to fibers, inclined at a plane with respect to the loading direction under transverse compression (Figure 19). The failure is a combination of yielding in the matrix due to in-plane shear, friction between the two failure surfaces and fiber-matrix debonding (Agarwal, Broutman, & Chandrashekhara, 2015; Talreja, 2016; Lowe, 1996). A fracture plane angle of $53^\circ (\pm 3^\circ)$ has been reported for carbon fiber epoxy systems (Totry, González, & Llorca, 2009; Rouf, et al., 2021; Tsampas, Greenhalgh, Ankersen, & Curtis, 2012). Several studies (Hu, Kar, & Nutt, 2015; Totry, González, & Llorca, 2009; González & Llorca, 2007; Gutkin, 2013) have been conducted over the last decades to study and predict the influence of various factors affecting the angle of fracture plane in various composite material systems.

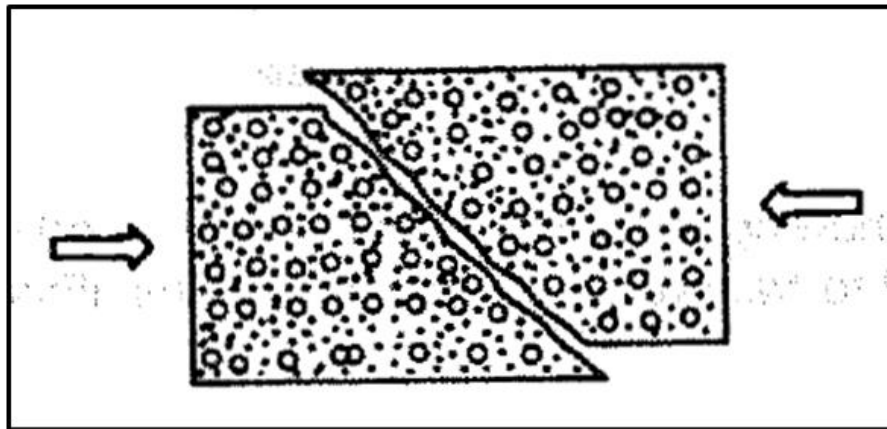


Figure 19: Failure under transverse compressive load (Agarwal, Broutman, & Chandrashekhara, 2015)

Hu et al (Hu, Kar, & Nutt, 2015) investigated the effect of fiber volume fraction on the fracture plane angle. The angle for composites was higher than neat matrix due to the distortion of shear bands in matrix owing to the presence of stiff fibers and found to increase till the fiber volume fraction approached a hexagonal packing of fibers (fiber volume fraction $\geq 68\%$), the densest possible arrangement.

Further, fiber/matrix adhesion also has a pronounced effect on the mechanisms leading to failure (González & Llorca, 2007; Hu, Kar, & Nutt, 2015; Totry, González, & Llorca, 2009). Simulation studies have shown the decohesion between the fibers and the matrix as dominating mechanism leading to final failure in the case of weak fiber/matrix interface. Cracks were formed at weak interfaces at low stresses, even when the material was in elastic regime. These cracks linked at increasing levels of stress to form the final fracture plane. On the other hand, continuous and smooth shear bands were formed in the matrix in the case of strong fiber/matrix interface, which resulted into the failure plane.

A prominent effect of strain rate on the transverse compression behavior of NCF carbon fiber/epoxy composites was recently observed by Rouf et al (Rouf, et al., 2021). The fracture plane angle was found to increase from 53° to 60° when the strain rate was increased from a quasi-static rate to high rate. Also, while the failure at quasi-static rate was characterized by a single crack, multiple cracks were observed at higher rates (Figure 20).

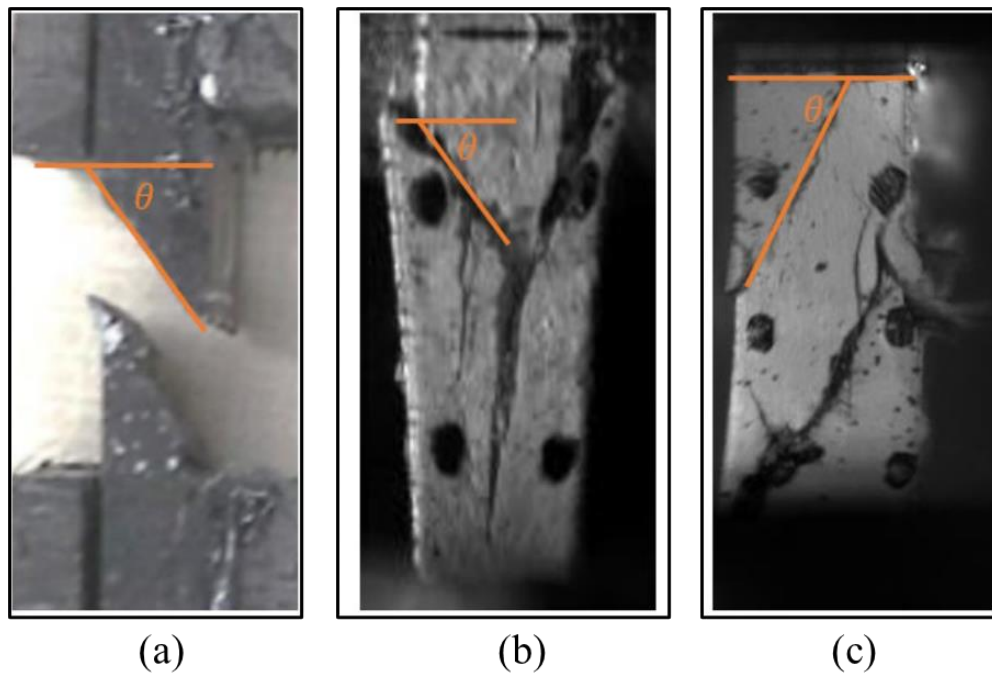


Figure 20: Coupons failed under transverse compression at (a) quasi-static (b) intermediate (c) high strain rates (Rouf, et al., 2021)

2.3.3.2 Multidirectional laminates

Majority of the studies (Shipsha, Burman, & Ekh, 2018; Gutkin, Pinho, Robinson, & Curtis, 2010; Pinho, Darvizeh, Robinson, Schuecker, & Camanho, 2012) found in the open literature on multidirectional laminates were aimed at understanding the influence of neighbouring plies on the kink-band formation in the load bearing plies.

Studies on cross-ply laminates have revealed that kink-band formation in the 0° plies is delayed in the cases where the 0° plies were sandwiched between 90° plies. This was due to the obstruction to the rotation of fibers in 0° plies offered by the 90° plies (Gutkin, Pinho, Robinson, & Curtis, 2010). The location of the kink-band was also found to be dependent on the location of damage in the 90° plies (Pinho, Darvizeh, Robinson, Schuecker, & Camanho, 2012).

Fractographic studies by Shipsha et al (Shipsha, Burman, & Ekh, 2018) on biaxial $[(90+\theta/0+\theta/90+\theta/0+\theta)]_s$; where θ is the off-axis angle ranging from 0° to 90°) NCF composite specimens at various off-axis angles revealed that the failure occurred primarily parallel to the fibers upto an off-axis 20° angle and perpendicular to the fibers above 60° angle. Although fiber-kinking was the governing failure mode in all the specimens (except at an off-axis angle of 45°), the failure was a combination of matrix cracks, cracks within the tows, cracks along tow boundaries, axial splits and fiber kinking.

The influence of stacking sequence and ply thickness on the failure process in quasi-isotropic CFRP prepreg laminates under compression was studied by Leopold et al (Leopold, et al., 2017). Unnotched specimens and coupons with an open hole were investigated in this study. Damage was found to initiate at a lower strain with increasing ply thickness in the specimens. Thinner specimens have statistically a lower number of defects which effectively delays damage initiation. While a pronounced effect of the position of load bearing 0° plies on the stability of the unnotched test coupons was observed, failure in open hole test coupons was only dependent on the ply thickness. The material failed due to fiber buckling in the drilled hole.

Microscopy techniques were employed in another study (Tsampas, Greenhalgh, Ankersen, & Curtis, 2012) to understand the effect of stacking sequence damage mechanisms in cross-ply and multidirectional laminates through post-failure observations. Depending on the laminate and loading condition, delamination was found to induce other damage mechanisms such as in-plane shear damage, through-the-thickness translaminar fracture or buckling of load bearing plies due to loss of lateral support.

Chapter 3

3 Research objectives

NCF composites have emerged as an attractive opportunity in the face of an increasing demand for light-weight materials in automotive sector. They are a trade-off between UD prepregs and woven fabric composites, imparting superior mechanical properties at a lower production cost. However, the crashworthiness properties of these materials is the key criteria for their adoption by the automotive OEMs for structural applications in light-weight vehicles. Unlike in metals, where the plastic deformation is the primary contributor to the crashworthiness of the structures, several distinct mechanisms contribute to the energy absorption in the structures made with composite materials (discussed in detail in Section 2.2.3.3). Several researchers have contributed towards a better understanding of the initiation, growth and monitoring of these mechanisms over the last few decades through their experimental and numerical investigations under various mechanical loading conditions (Section 2.3). There, however, remain many unexplored research avenues, some of which form the deliverables of the investigation in this study. The gaps in the existing state-of-the-art are pointed out in this chapter. The chapter concludes with a list of research tasks to fill in those gaps.

3.1 Gaps in the literature

It was alluded to in Section 2.3.1 that numerous characterization studies have been performed in the last decade and a half on NCF composites. The stitching fibers in NCF composites were found to have a negligible effect on the measured engineering properties in these studies. Furthermore, characterization tests at elevated temperatures revealed a more pronounced effect on the matrix-dominated properties. The compression properties were found to be generally half of the corresponding tensile properties of the same material system. The compression properties were also reported to exhibit a higher sensitivity to the local fiber misalignments. Multiple studies report comparisons between the measured engineering properties of NCF composites and competitor UD prepreg and woven composites. The interlaminar fracture toughness test results were generally

dependent on specimen geometry, reinforcement architecture and testing parameters. Despite the availability of many reports, there is an inconsistency in the reported data trends with respect to CLT predictions or measurements on UD tape composites. For example, Godbehere et al (Godbehere, Mills, & Irving, 1994) reported only a 1% drop in tensile properties of NCF composites as compared to pre-impregnated UD, while Bibo et al (Bibo, Hogg, & Kemp, 1997) reported a 35% drop. There is also an inconsistency in the trends reported for the measured compression properties. The measurements may also be governed by the limitations of the actual test method employed (like in the case of in-plane shear), end conditions (for example, difference in the grip conditions in a compression test) and geometry of the specimens (for example, interlaminar fracture toughness characterization). These considerations make it imperative to thoroughly characterize the material system under investigation.

As can be inferred from Section 2.3.2, several numerical studies have been performed since 1980s to understand and predict the damage behavior in composites under tensile loads. The events leading up to failure are clearly understood in the case of unidirectional laminae. Generally speaking, in the case of multidirectional laminates, first form of damage occurs in the form of cracks in the transversely oriented plies, followed by cracking in other off-axis plies. The failure of the laminate is, however, governed by the failure of the load-bearing 0° fibers. Much of the work on damage in multidirectional laminates is of numerical nature and focused on characterizing the cracking patterns in the transverse plies and off-axis plies. Very few experimental studies on the evolution of damage with a focus on heavy-tow multidirectional NCF composites could be found. Further, while it is clear that the resin-rich zones caused by the stitching fibers are the most compliant zones in NCF composites, their role in damage evolution is still unclear. A part of this study, hence, focuses on developing a complete picture of the damage in NCF composites under tensile loads. The study aims at understanding the initiation and growth of several damage mechanisms and is supported by post-failure fractographic observations. The influence of stacking sequence on the damage growth, and energy absorption, is also investigated in this study.

Majority of the studies on compressive damage and failure in composites (Section 2.3.3) are focused on UD composites. The studies are primarily focused on understanding the formation of kink bands in axially loaded UD composites and the prediction of fracture plane angle in UD composites under transverse compression. The studies on multi-directional composites are conducted on cross-ply laminates to understand the influence of constraints on kink-band formation and not on characterizing the initiation and development of damage. None of the studies were aimed at understanding the evolution of damage in multi-directional NCF composites under compressive loads. The investigation conducted in this study, therefore, aims at capturing in-situ the growth of damage under compressive loads in NCF composites from initiation to failure.

3.2 Objectives

Although NCF composites have grown in prominence in the recent years for structural applications in lightweight automotive, there still are many unknowns with regards to the damage and energy absorption in these materials. There are inconsistencies and contradictions in the reported characterization results owing to various testing and geometric parameters. Further, a comprehensive experimental study that paints a complete picture of damage in NCF composites under tension and compression is lacking in the state-of-the-art. This study aims at contributing towards the same. Following research objectives were set, based on the identified gaps in the literature:

1. Characterize the mechanical response of NCF composites at quasi-static loading rates, including interlaminar fracture toughness.
2. Establish the damage evolution process, from initiation to failure, in multi-directional laminates under tension and compression using in-situ damage monitoring techniques and post-failure fractographic observations.
3. Connect the damage to underlying mechanics and energy dissipation in the creation of damage.

Chapter 4

4 Materials and Methods

This chapter gives an insight into the material system investigated in this study and also the experimental protocols maintained. The first part of the chapter describes the micro- and mesostructural details of the studied materials, including the manufacturing details. The test set-up, American Society for Testing and Materials (ASTM) standards and relevant experimental methods are discussed in the later part.

4.1 Material System

The NCF composites assessed in this study comprised a fast-curing epoxy resin (provided by Hexion Inc., Appendix 2; Zeng, 2020) and heavy tow unidirectional carbon fiber NCF layers (supplied by Zoltek Corp., Appendix 3; Trejo Sandoval, 2020). The fast-curing resin system, with a curing time of 5 minutes, was a three-part epoxy system, consisting of EPIKOTE™ Resin TRAC 06150, EPIKURE™ Hardener TRAC 06150 and internal mold release (IMR) agent HELOXY™ Additive TRAC 06805. The resin:hardener:IMR mixing ratio was 100:24:1.2. The PX35 UD300 heavy tow reinforcement fabric containing straight tows containing 50,000 continuous carbon filaments each, stitched by a polyester stitching in a Tricot knitting pattern in the tow direction. The reinforcement fabric also consisted of supporting glass yarns, oriented perpendicular to the tows. The areal density of the fabric was 333 g/m². The carbon fibers were 92.8% of the total weight of the fabric. The weight fraction and linear density of the polyester stitching were 1.8% and 75 decitex and of the supporting glass fibers, 3.0% and 34 decitex, respectively. Flat panels (Appendix 4), measuring 900 X 550 mm, with two unidirectional stacking sequences, [0]₇ and [0]₁₁, and two multi-directional stacking sequences were fabricated, namely [0/±45/90]_s and [±45/0]_s. The laminates were tested in axial and transverse directions, and will be referred to as [0/±45/90]_s, [90/±45/0]_s, [±45/0]_s, and [±45/90]_{2s} in this dissertation. The panels were manufactured using High-Pressure Resin Transfer Molding (HP-RTM) process at Fraunhofer Project Center (FPC) at Western University, London Ontario (Figure 21).

In this process, the fabrics were first placed in the mold in the desired stacking sequence such that the stitching fibers were away from the surface of the mold. The fabrics were bonded together with a chemical binder. The mold was then preheated to and maintained at 120°C. The resin, hardener and IMR were mixed in the aforementioned ratio at 120 bar and injected into the mold at a flow rate of 40 g/s under a press force of 1500 kN. The force was then increased to 4500 kN during the curing process to yield the panels (Meirson, 2018). The resulting volume fraction of the panels was measured to be 53% by optical microscopy measurements. Further, optical microscopic observations confirmed that the void content was negligible. The test coupons were extracted from these panels using an abrasive waterjet cutter.

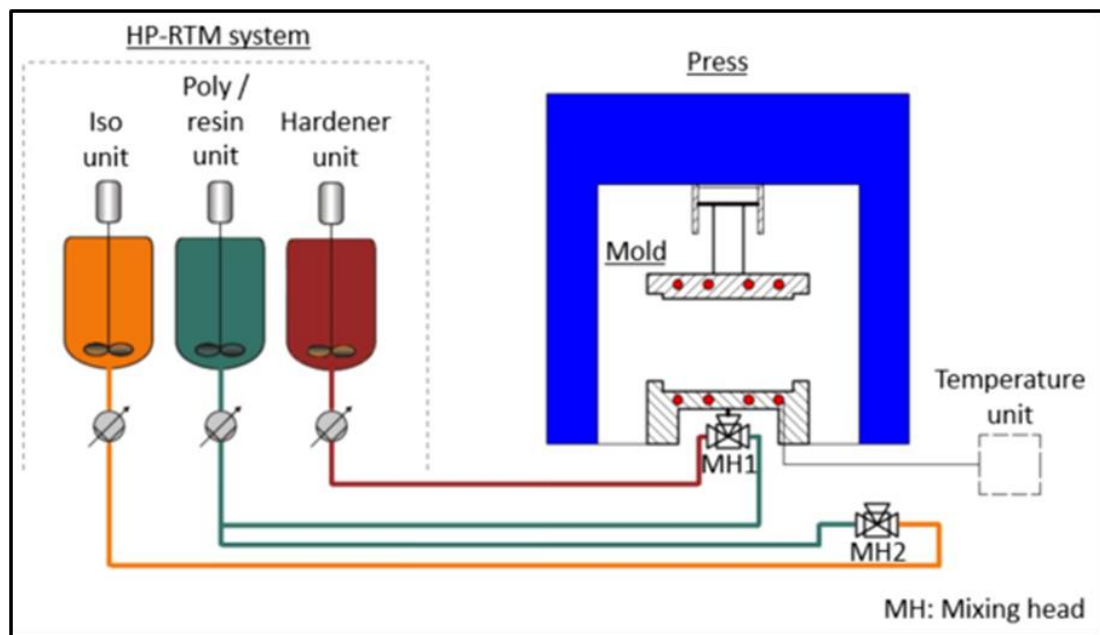


Figure 21: Schematic of High-Pressure Resin Transfer Molding (HP-RTM) process (Meirson, 2018)

4.2 Test set-up

The quasi-static characterization tests were carried out on a servo-hydraulic test frame (INSTRON 8804, Norwood, MA, USA; Figure 22) equipped with hydraulic wedge grips using either of 5 kN or 250 kN load cells. Two GRAS-505SM-C (Point Grey) digital cameras with 2448 X 2048 pixel resolution, with a pixel size of 3.45 μm , were used to capture the specimen images during the tests. The specimen surfaces to be imaged were speckled with a random white-on-black pattern to facilitate the strain measurement by DIC technique using the Vic3D software. The images were taken at a rate of 3.33 frames per second, unless otherwise specified. A region of (40 mm X 20 mm) 800 mm^2 was generally selected for strain acquisition.

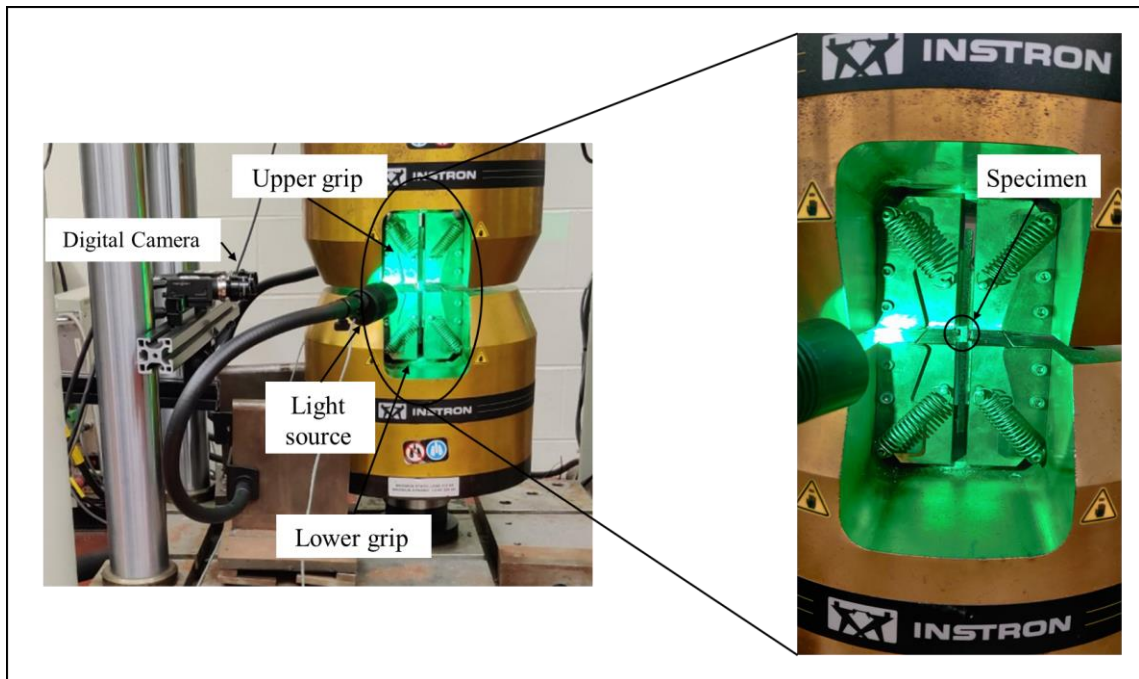


Figure 22: INSTRON 8804 servo-hydraulic test frame

4.3 Test methods

4.3.1 Quasi-static characterization

4.3.1.1 Tension, compression and in-plane shear tests

The tension (ASTMD3039, 2017), compression (ASTMD3410, 2016) and in-plane V-Notch shear tests (ASTMD7078, 2012) were conducted on the set-up described in Section 4.2 with a 250 kN load cell in accordance with the respective ASTM standards (test parameters can be found in Table 1). The listed tests were conducted on all the stacking sequences ($[0]_7$ or $[0]_{11}$, $[0/\pm 45/90]_s$, $[\pm 45/0_2]_s$) in both axial and transverse directions. The specimens were extracted from the thinner unidirectional lamina, $[0]_7$, for tension and in-plane shear tests. The compressive tests were conducted on the unidirectional lamina with 11 layers, i.e. the thicker lamina, to avoid Euler buckling of the test coupon. The microstructure of both the UD layups was, however, comparable.

Table 1: Quasi-static mechanical test parameters. ‘t’ stands for specimen thickness.

	ASTM standard	Dimensions (mm)	Gauge length (mm)	Rate of testing (mm/min)
Tension	D3039	200*25*t	50	2
Compression	D3410	150*25*t	10	1
V-Notch shear	D7078	76*56*t	31	2

Test coupon geometry is represented in Figure 23. Carbon fiber/epoxy tabs were bonded on both the faces at the end of the specimens with Devcon 5 Minute[®] two-part epoxy glue to promote the failure in gauge lengths in tension and compression tests. The thickness of the tabs was in the range of 2.5-3.0 mm. The tabs used for tension tests had a low bevel angle of approximately 10° to allow for a smooth transition into the coupon gauge length. On the other hand, non-beveled tabs were used for compression tests, as they have been reported to produce acceptable failure modes in the ASTM D3410 standard. Spacers were used for specimen alignment in the V-Notch test while tightening the clamping bolts. A bolt torque of 94 Nm was required to clamp the specimens in the V-Notch test fixture.

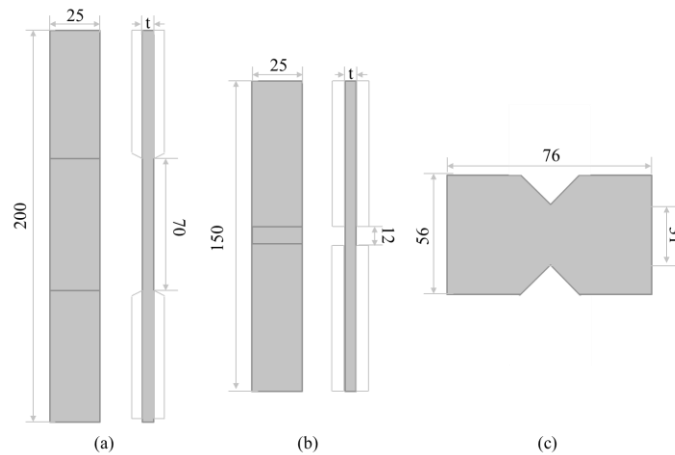


Figure 23: Representative test coupon geometry for (a) tensile test (b) compressive test (c) V-Notch in-plane shear test. ‘t’ stands for specimen thickness. All dimensions are in ‘mm’.

4.3.1.2 Interlaminar fracture toughness tests

The opening Mode-I interlaminar fracture toughness was determined using a DCB test. The test was conducted in accordance with the ASTM D5528 standard (ASTMD5528, 2013). Flat, rectangular, 25 mm wide test coupons were extracted from the manufactured plaques using a waterjet cutter. The specimens were approximately 130 mm long, including a Teflon insert on the mid-plane with a length of 65 mm (Schematic for a typical DCB specimen is shown in Figure 24.a.). The Teflon insert was placed on the midplane during the plaque manufacturing process. The Mode-I opening forces were applied to the specimens through Nickel plated aluminum piano hinges (Figure 24.b.) glued to the specimens using Loctite 495 adhesive. The piano hinges were glued to result in an initial delamination length (a_0), measured from the line of load introduction to the end of the insert, of 50 mm. The edge of the specimen was coated with a thin layer of a white correction fluid to aid in visual detection of the crack. The specimen was then loaded at a constant crosshead displacement rate of 5 mm/min. The crack propagation was observed at the edge of the specimen using two GRAS-505SM-C (Point Grey) digital cameras with 2448 X 2048 pixel resolution. The images of the edge were taken at 2 frames/second. The crack lengths were manually measured using ImageJ software.

Modified Compliance Calibration (MCC) method was used to calculate Mode-I interlaminar fracture toughness (G_{Ic}). The slope (A_1) of least squares plot of normalized delamination length (a/h) as a function of cube root of compliance ($C^{1/3}$) is used in this method. Compliance is the ratio of load-point displacement (δ) and load (P). The formula for G_{Ic} calculation is as follows:

$$G_I = \frac{3P^2C^{2/3}}{2A_1bh} \dots (11)$$

Where:

P = load (N)

C = compliance (mm/N)

A_1 = slope of least squares plot (a/h) vs ($C^{1/3}$) ((mm/N)^{-1/3})

b = specimen width (mm)

h = specimen thickness (mm)

Alternate data reduction methods include Modified Beam Theory (MBT) method, Compliance Calibration (CC) (ASTMD5528, 2013) and a load-independent equation (de Verdiere, Skordos, May, & Walton, 2012; Isakov, May, Paul, & Nishi, 2019), which are discussed in the Appendix 5.

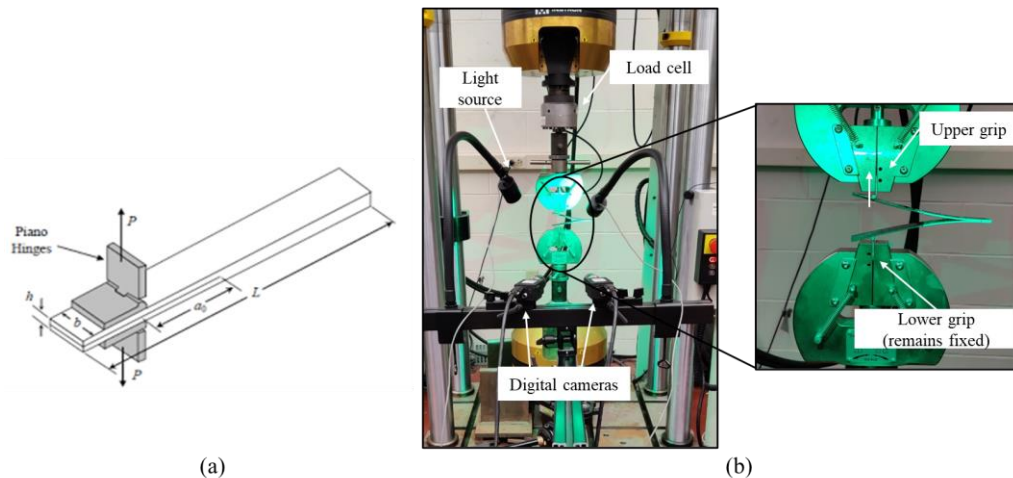


**Figure 24: (a) Schematic for typical Double Cantilever Beam (DCB) test specimen
(b) DCB test set-up**

The test method used to determine Mode-II shear delamination fracture toughness by End Notch Flexure (ENF) test, ASTM D7905 (ASTMD7905, 2019) standard was referred to for sample preparation and test parameters. Similar to DCB test coupons, rectangular specimens were removed from the plaques using waterjet cutter. The specimens were 25 mm wide and 140 mm long, containing 50 mm of non-adhesive Teflon insert on the midplane. The tests were carried out on a 3-point testing fixture with a specimen span (2L) of 100 mm and a half span (L) of 50 mm (Figure 25). The radius of loading and support pins was 9 mm. The specimen was placed such as to have an initial delamination length of 30 mm. The initial delamination in an ENF test is measured from the center of the support pin to the end of Teflon insert. A thin coat of white correction fluid was applied on the edge, like in DCB test. The test was carried out at a crosshead displacement rate of 0.5 mm/min. The edges were observed using two GRAS-505SM-C (Point Grey) digital cameras at 1 frame per second and the crack lengths were measured manually using ImageJ software. Further, the specimens were not subjected to any additional pre-cracking in this case to avoid any external inaccuracies in the data. The Mode-II fracture toughness (G_{IIc}) was calculated by Carlson method (Carlsson & Pipes, 1987):

$$G_{II} = \frac{9P^2 a^2}{16E_{11} b^2 t^3} \dots (12)$$

Where:

P = load (N)

a = crack length (mm)

E_{11} = Elastic modulus of the specimen arms (N/mm²)

b = specimen width (mm)

t = half of specimen thickness (mm)

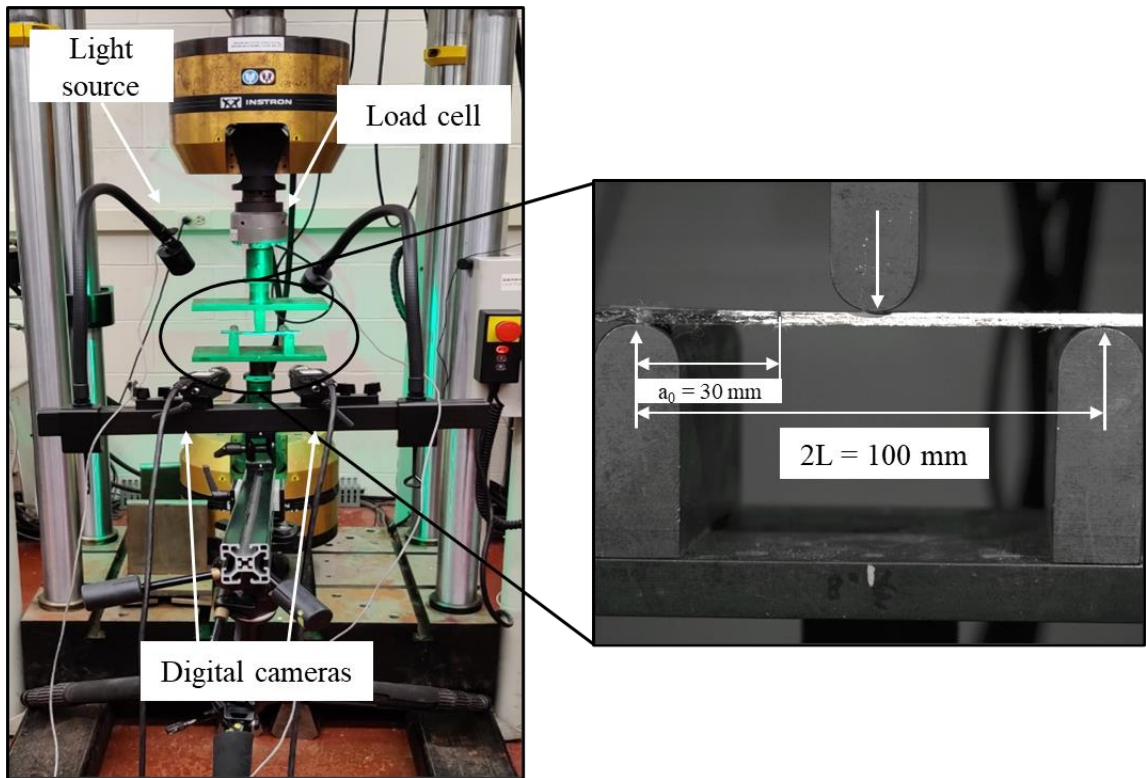


Figure 25: End Notch Flexure (ENF) test set-up

4.3.2 Damage evolution tests

The damage evolution was captured in-situ using an ER technique, which required polishing of the specimen edges to observe the microstructure. The specimen edges were first wet sanded with 240-grit, 400-grit and 600-grit silicon carbide sandpaper. Next, the specimen edges were polished with a 3-micron diamond paper and mineral oil on a low nap polishing pad for two hours in 20-minute runs, and finally with 0.25-micron diamond powder and mineral oil on a medium nap polishing pad for two to three hours in 20-minute runs. The tests were paused at pre-defined displacements, where a 125 μm thick cellulose acetate film wetted with acetone was compressed on the specimen edge using a rubber pad for two minutes to imprint the microstructure. The replicas were then observed under a Leitz Purapol 11 optical microscope (Figure 26). The displacement was then reduced manually to nearly 0 mm and the process repeated for subsequent values of displacement. Only one test per stacking sequence and loading condition was conducted.

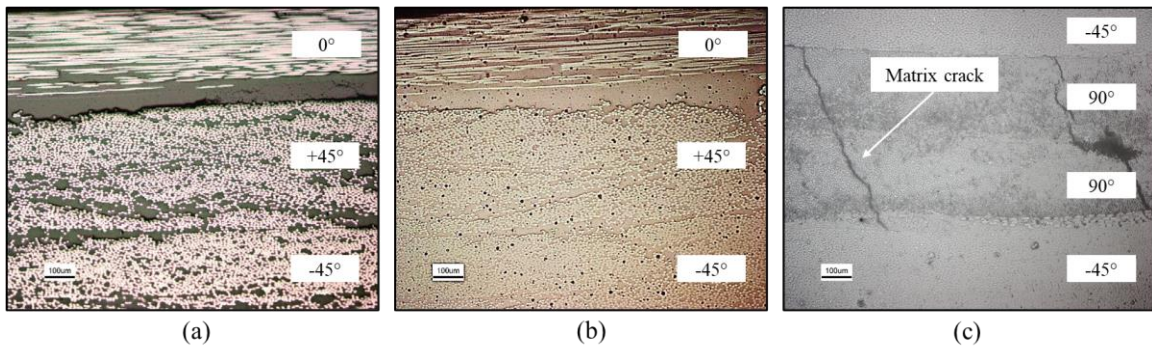


Figure 26: $[0/\pm 45/90]_s$ laminate microstructure on: (a) Actual edge (b) Replicating tape (c) Crack on replicating tape

A 30 mm section from the 50 mm gauge length (hence an area of approximately 90 mm^2) was considered for damage observation. The cracks appearing in each individual ply were measured. Only the cracks extending through the thickness of an entire ply were counted as one ply crack. The positions of the cracks were marked on the replica during microscopic observation to later determine the crack spacings. The crack opening displacements were measured from the microscopy images using ImageJ software. Delaminations along the ply interfaces were measured directly from the replica using a ruler.

4.3.3 Post-failure characterization

The edges and the surfaces of the specimens were observed post-failure with a Nikon Eclipse L150 optical microscope with DS-Fi3 digital camera and a Scanning Electron Microscope (SEM) respectively. The surfaces of the failed specimens were observed under Hitachi SU3900 SEM. The specimens were coated with gold for 2 minutes. The images were taken in electron backscattering (BSE(3D)) mode at 0.3 mmHg pressure and 15 kV voltage.

Chapter 5

5 Results: Quasi-static material characterization

The global response of the NCF composites under quasi-static loads is discussed in this chapter. All the tests are conducted on the test set-up discussed in Section 4.2. The stress was calculated directly using the load data from the machine and the measured specimen geometry in all the tests. The global strain, in all the tests was measured using DIC (Section 4.3.1). The engineering properties are summarized in Appendix 6. It must, however, be noted that this chapter focuses solely on the discussion of global response. The connection to the microstructure is made in the subsequent chapters (Chapter 6 and Chapter 7).

5.1 Tensile loads

5.1.1 Unidirectional lamina

Five specimens each were tested under axial and transverse tensile loads. All the specimens exhibited a linear-elastic behavior until failure (Figure 27). All the tested specimens failed in the gauge section in a brittle fashion. While the failure of the axially loaded coupons was primarily in the middle of gauge section, the transversely loaded specimens failed closer to either of the grips but within the gauge length.

The axial tensile response is dominated by the fiber response. The test coupons failed explosively when the failure strain of carbon fibers was reached, at about 1.3%. Some of the specimens exhibited a slight increase in stiffness at higher strains. This phenomenon can be most clearly observed in the stress-strain curve of “specimen 2” in Figure 27.a. This could be attributed to unfolding of a limited crimp in the specimen and rotation of the fibers in the direction of loading. The response under transverse tensile loads, on the other hand, was governed by the matrix and fiber-matrix interface properties. Since the load-to-failure of these specimens was much lower than the capacity of the load cell, considerable noise was recorded in the data in the form of oscillations. The failure characteristics of the specimens are discussed in detail in the next chapter (Section 6.1).

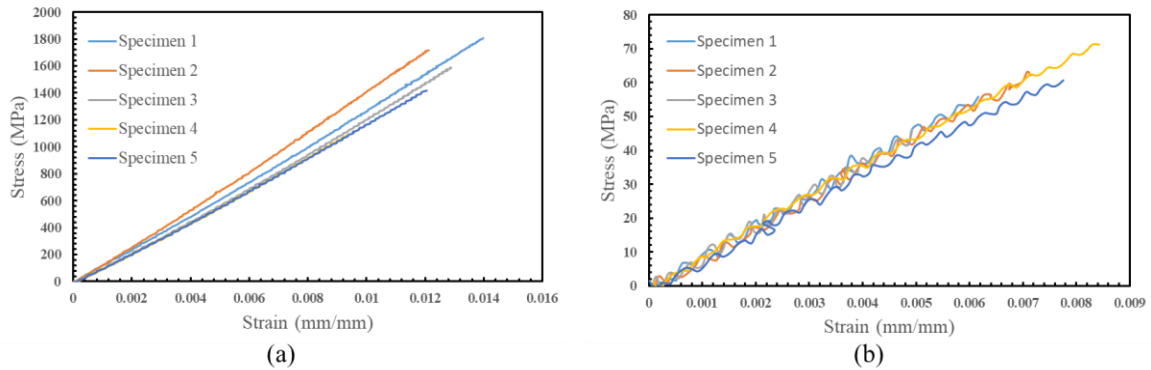


Figure 27: Stress-strain curves for unidirectional lamina under (a) axial tensile loads (b) transverse tensile loads

5.1.2 Multidirectional laminates

The stress-strain responses of all the test coupons from the $[0/\pm 45/90]_s$ and $[90/\pm 45/0]_s$ laminates were repeatable (Figure 28.a. and Figure 28.b.) with very minimal scatter. The failure of all the test coupons was governed by the failure of the load bearing plies. All the tested laminates failed in the gauge section when the failure strain of the load-bearing fibers was reached (1.3% strain). As can be seen in Appendix 6, the measured engineering elastic moduli, tensile strength and strain-to-failure are almost identical for both the laminates. The elastic moduli, tensile strengths and failure strains were measured to be 42 GPa, 546 MPa, 1.4% and 42 GPa, 532 MPa, 1.3% for $[0/\pm 45/90]_s$ and $[90/\pm 45/0]_s$ laminates respectively. This implies that the stacking sequence of the laminate does not affect the measured engineering properties. Minor differences were, however, observed in the stress-strain responses. Load drops were observed close to failure, at about 1.2% strain, in the test coupons in the $[0/\pm 45/90]_s$ laminate. These drops supposedly correspond to the breakage of carbon fiber bundles and occur around the same strain. Such load drops were also observed in the $[90/\pm 45/0]_s$ laminates at a lower strain of 0.9%. In this case, however, the drops correspond to cracking in off-axis plies. This is an indication that although the stacking sequence of the laminates has negligible influence on the measured engineering properties under tension, the initiation and growth of damage must be different depending on the relative position of the plies in the laminate. The same is investigated further in Section 6.2.2.1.

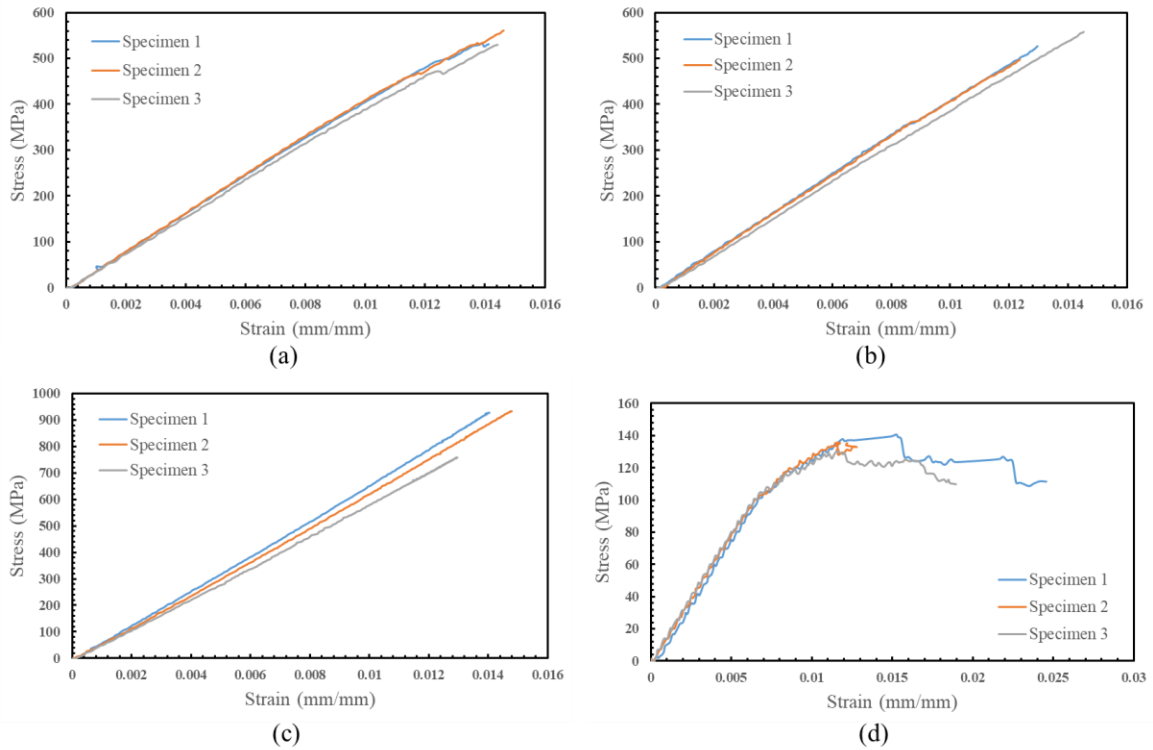


Figure 28: Tensile stress-strain curves for (a) $[0/\pm 45/90]_s$ laminate (b) $[90/\pm 45/0]_s$ laminate (c) $[\pm 45/0]_2$ laminate (d) $[\pm 45/90]_2$ laminate

The response of the stiffer 0° plies was reflected in the stress-strain response and measured properties of $[\pm 45/0]_2$ laminate (Figure 28.c.). The stiffness and the tensile strengths of the laminate in the axial direction were measured as 62 GPa and 934 MPa. The tested coupons failed in a brittle manner in the center of the gauge length once the failure strain of 0° plies was reached (1.4% strain). On the other hand, in the $[\pm 45/90]_2$ laminate, all the plies are oriented off-axis with respect to the loading direction. Therefore, the laminate was significantly more compliant as compared to the $[\pm 45/0]_2$ laminate. The elastic modulus and tensile strength were measured to be 18 GPa and 135 MPa respectively for the $[\pm 45/90]_2$ laminate.

Very clear change in slope and load drops could be observed in the stress-strain curves of the $[\pm 45/90_2]_s$ laminate (Figure 28.d). The change in slope at around 0.75% strain suggests an onset of damage. The growth of damage makes the material further compliant, as can be most clearly seen in the stress-strain response of “specimen 1” in Figure 28.d. The two sharp load drops, as characterized by vertical lines, likely correspond to cleavage of the 45° plies. The laminate fails eventually at about 1.8%. The damage evolution process is further discussed in Section 6.2.2.2. A large amount of scatter can be observed in the strain-to-failure recordings of the $[\pm 45/90_2]_s$ laminate. This may be attributed to the individual plies all failing along the same plane in that particular test coupon, which is a stochastic phenomenon.

5.2 Compressive loads

5.2.1 Unidirectional lamina

The unidirectional lamina exhibited a linear-elastic response to failure under axial loads (Figure 29.a.), reflecting the expected response from 0° plies. The failure in all the axially loaded specimens was by formation of out-of-plane kink bands in the gauge section at a failure strain of 0.8%. The compressive stiffness of the materials was measured to be 122 GPa, which was equal to the tensile stiffness (121 GPa). The compression strength (1000 MPa) was, however, about 60% of the tensile strength (1637 MPa). The results in this study are slightly different from the literature reports which generally suggest tensile stiffness to be 10% higher than the compressive stiffness, and the compression strength to be about 50% of the tensile strength. Furthermore, the axial compression strength measurements contain a large amount of scatter. As has been reported in the literature, the axial compression strengths are highly sensitive to even small misalignments. Therefore, the scatter may be attributed to a bundle of fibers with large local misalignment or a slight specimen misalignment. On the other hand, the unidirectional lamina failed under transverse compression as a result of matrix yielding and fiber/matrix debonding at 2.42% strain. The change of slope of the stress-strain curves (Figure 29.b.) is indicative of the shear response of the matrix. The failure of all the tested specimens was characterized by the formation of a failure plane inclined at an angle of about 53° to the loading direction in the gauge section, which is discussed in detail in Section 7.1.2.

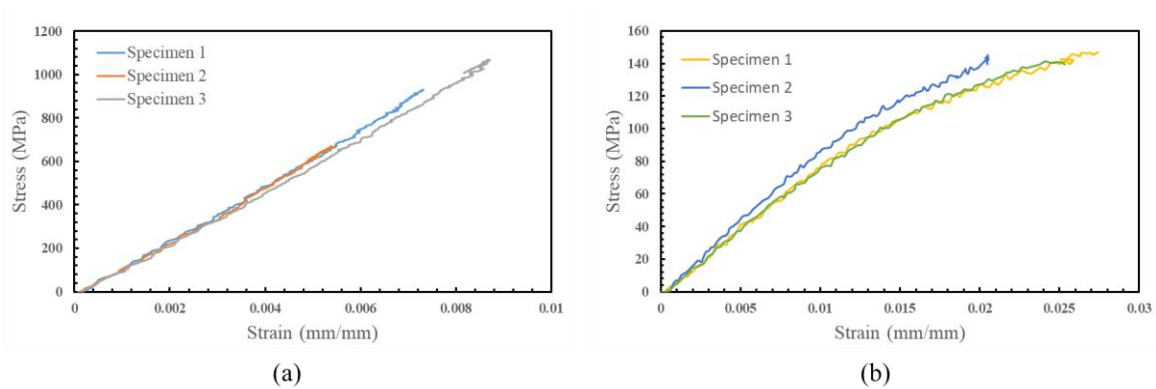


Figure 29: Stress-strain curves for unidirectional lamina under (a) axial compressive loads (b) transverse compressive loads

5.2.2 Multidirectional laminates

Three specimens each were tested for all the laminates investigated in this study. The failure was a combination of delamination, matrix crack and fiber shear failure in the laminates, depending on the stacking sequence and loading condition. The failure occurred in the gauge section of the coupons and the visually observed laminate specific failure characteristics were consistent across all the tests.

The effect of stacking sequence can be clearly observed on the compressive responses of $[0/\pm 45/90]_s$ and $[90/\pm 45/0]_s$ laminates (Figure 30.a. and Figure 30.b.). The $[0/\pm 45/90]_s$ laminate, wherein the compliant off axis plies are sandwiched between the 0° plies, is stiffer and significantly stronger. The strains-to-failure for the $[0/\pm 45/90]_s$ laminate are slightly higher than the $[90/\pm 45/0]_s$ laminate. The compression moduli, compression strengths, strains-to-failure were measured to be 37 GPa, 384 MPa, 1.1% and 31 GPa, 265 MPa and 1% for the $[0/\pm 45/90]_s$ and $[90/\pm 45/0]_s$ laminates respectively. The presence of 0° plies on the outside constrains the damage in the compliant off-axis plies, delaying the catastrophic failure. The failure in $[90/\pm 45/0]_s$ laminate, on the other hand, is very strongly dependent on the stability of the central load-bearing plies. The material fails catastrophically as soon as the load-bearing plies fail.

The compressive stiffness and strengths of the $[\pm 45/0_2]_s$ laminate (Figure 30.c.; measured to be 59 GPa and 399 MPa respectively) is significantly higher than the $[\pm 45/90_2]_s$ laminate (Figure 30.d.; measured to be 18 GPa and 179 MPa), as was expected due to higher concentration of the stiffer 0° plies. There was, however, high amount of scatter in the compression data for $[\pm 45/0_2]_s$ laminate. The response of this laminate is very strongly dependent on the stability of the central block of 0° plies, which is highly sensitive to even the slightest of fiber misalignments, which may cause scatter in the data. The data for $[\pm 45/90_2]_s$ laminate was, however, consistent.

The damage initiation and propagation processes are discussed in detail in Section 7.2.

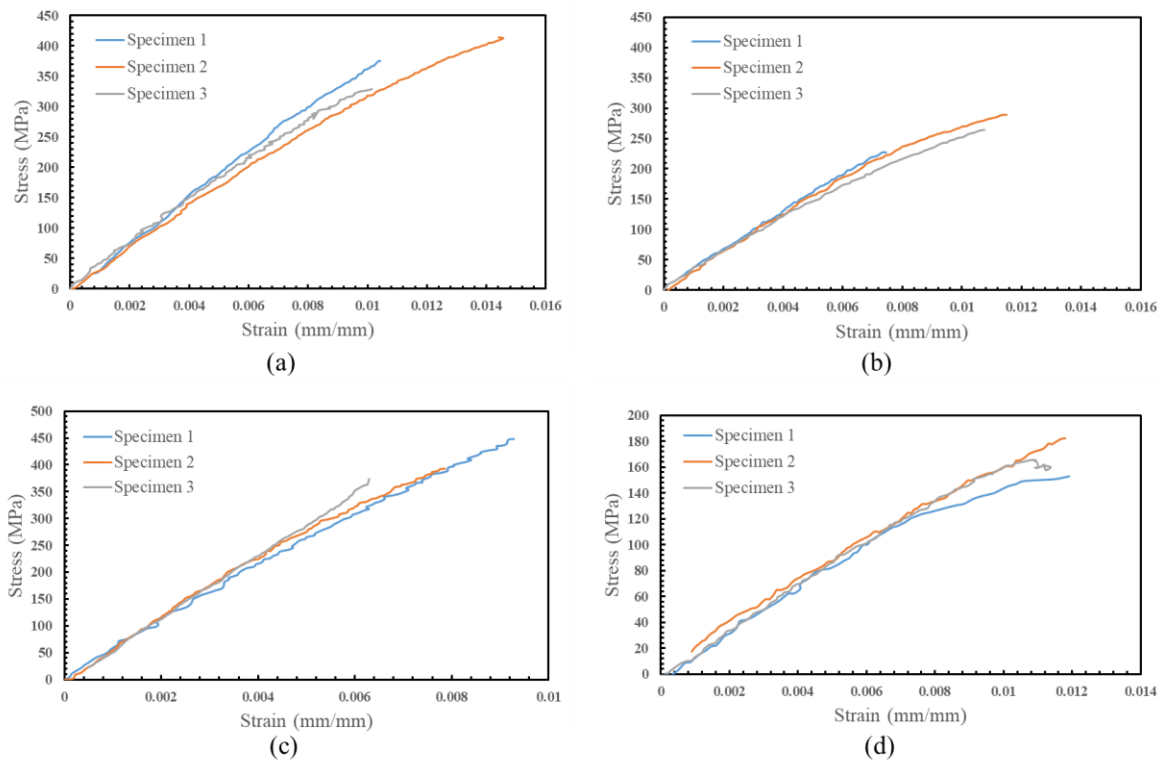


Figure 30: Compressive stress-strain curves for (a) $[0/\pm 45/90]_s$ laminate (b) $[90/\pm 45/0]_s$ laminate (c) $[\pm 45/0]_s$ laminate (d) $[\pm 45/90]_s$ laminate

5.3 In-plane shear loads

The in-plane shear properties of the unidirectional lamina were obtained using V-Notch rail shear test. A uniform simple shear state could be obtained through this test. The

stress-strain curves recorded from the test are shown in Figure 31.a. The shear modulus of the lamina was measured as 3.55 GPa. The stress-strain curves are characterized by the load drops associated with splitting between fiber and matrix at the roots of the notches followed by failure in the gauge length. Although the overall shapes of the stress-strain curves are identical for the specimens, the strain at which the notch-root splits occurred was found to vary. The load drops associated with the splits are observed between 2% and 4% engineering shear strain. The failure stress (about 89 MPa) was, however, close to the stress at which the notch-root splits (Figure 31.b.) were observed (about 75 MPa). The specimen shear strain-to-failure was recorded as 8.88%.

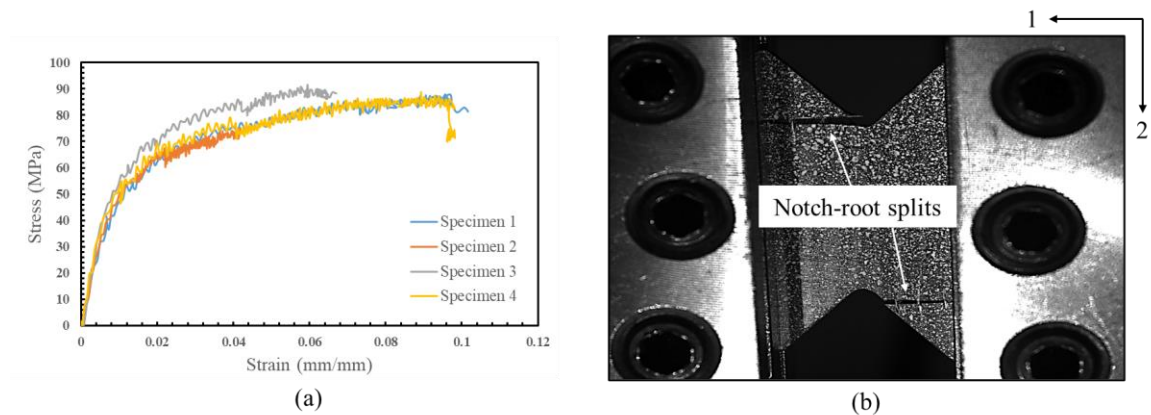


Figure 31: (a) Stress-strain curves for unidirectional lamina under in-plane shear loads (b) Notch-root splits observed during the V-Notch rail shear test

5.4 Interlaminar fracture toughness tests

5.4.1 Crack propagation under Mode-I and Mode-II loads

5.4.1.1 Mode-I loads

Three DCB tests were conducted for unidirectional and cross-ply laminates each under the testing conditions as described in Section 4.3.1.2. A symmetric opening of arms was observed in all the tests. Since the peak loads were around 50 N in all the tests (Figure

32), which is significantly lower than the capacity of the load cell (5 kN), the load signal data contained large amount of noise. A moving average filter was hence used to eliminate the noise. The data was averaged over 8-10 points for the tested specimens. Unprocessed load-displacement curves can be found in Appendix 7.

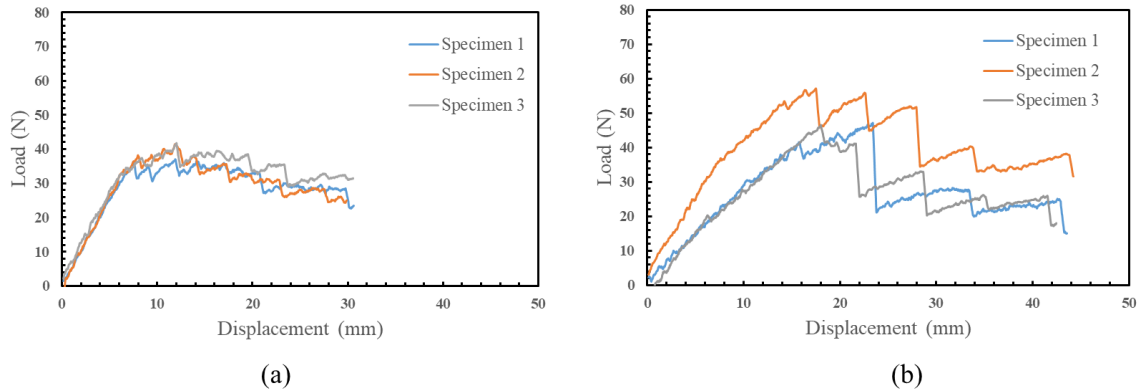


Figure 32: Filtered Mode-I load-displacement curves for (a) unidirectional lamina (b) cross-ply laminate

The crack propagated along the midplane in the interlaminar region in all the three tested specimens for unidirectional lamina (Figure 33.a.). However, the crack instantly migrated to the 0//90 interface upon initiation from the pre-crack in cross-ply laminates (Figure 33.b.). The crack then propagated along the 0//90 interface.

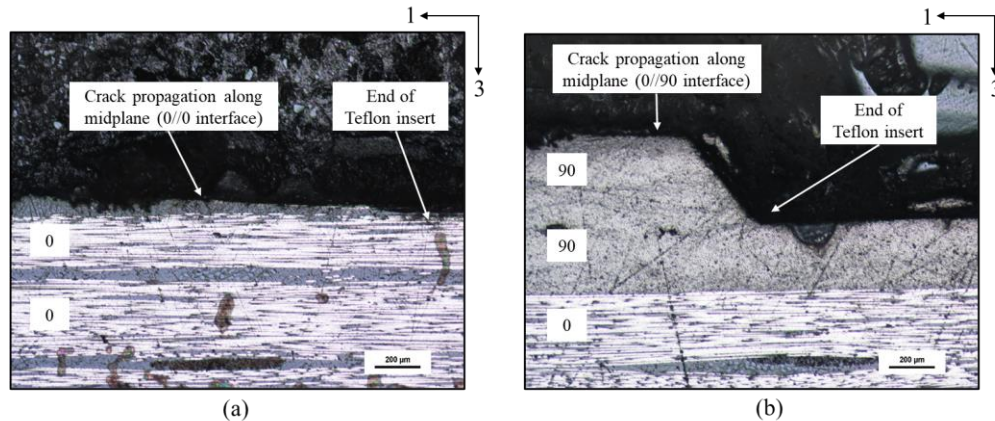


Figure 33: Mode-I interlaminar crack propagation in (a) unidirectional lamina (b) cross-ply laminate (through-thickness views)

A “stick-slip” type of crack propagation behavior was observed in both unidirectional laminae and cross-ply laminates. This tendency is characterized by alternating periods of unstable crack growth and crack arrest. The periods of unstable crack growth are characterized by sudden load drops and large jumps in crack length (Representative curves are shown in Figure 34, more curves in Appendix 8 and Appendix 9). The crack may either exhibit a slow growth, as is observed in the case of unidirectional lamina, or may remain relatively stationary, as in cross-ply laminates.

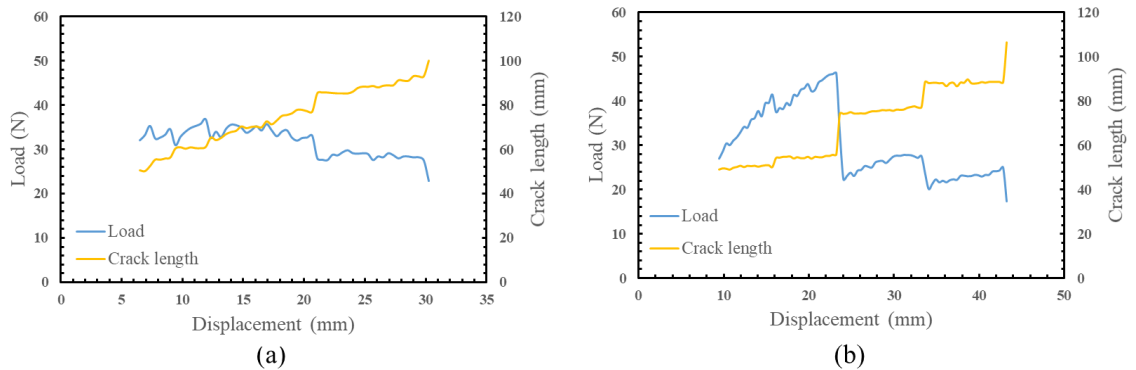


Figure 34: Representative Mode-I interlaminar crack propagation characteristics in (a) unidirectional lamina (b) cross-ply laminate

The stick-slip behavior of the crack was correlated with top views of the tested coupons. The crack arrest in unidirectional lamina was found to coincide with the presence of stitching sites (encircled in Figure 35.a.). On the other hand, the major resistance to crack propagation in cross-ply laminates was offered by the transverse tows on the crack path (encircled in Figure 35.b.). The presence of tows pinned the crack in a stationary position until sufficient energy was available for the crack to move around the tows.

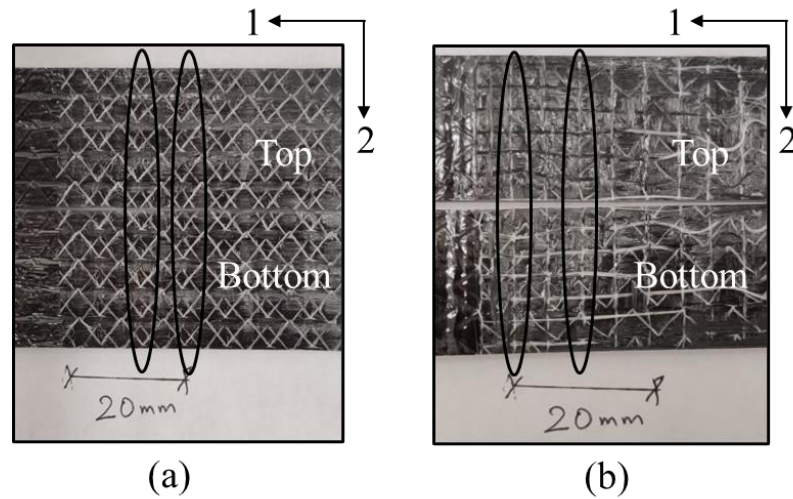


Figure 35: Top views of tested (a) unidirectional (b) cross-ply test coupons

5.4.1.2 Mode-II loads

Three ENF tests each were performed for unidirectional lamina and cross-ply laminates to understand crack propagation under Mode-II shear loading conditions. High consistency was observed in the load-displacement data for both stacking sequences (Figure 36). As also was observed during DCB tests, the crack primarily propagated on the mid-plane in unidirectional lamina and instantaneously deviated from the mid-plane to and propagated along 0//90 interface in cross-ply laminates.

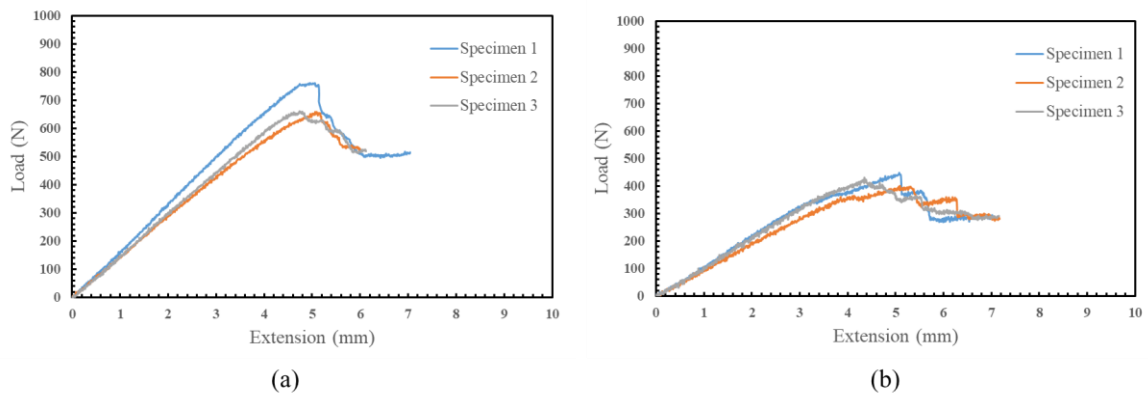


Figure 36: Mode-II load-displacement curves for (a) unidirectional lamina (b) cross-ply laminate

Representative crack propagation curves can be found in Figure 37 and the crack propagation results from other tests may be found in Appendix 10 and Appendix 11. A stable crack propagation was achieved under Mode-II loading in unidirectional laminae. However, similar to the crack propagation tendency under Mode-I loads, the crack exhibited a stick-slip behavior in cross-ply laminates. The transverse fiber tows resisted the propagation of the crack (inset in Figure 37.b.), resulting in periods of crack staying stationary, followed by the crack progressing in an unstable fashion till the next fiber tow arrests the crack.

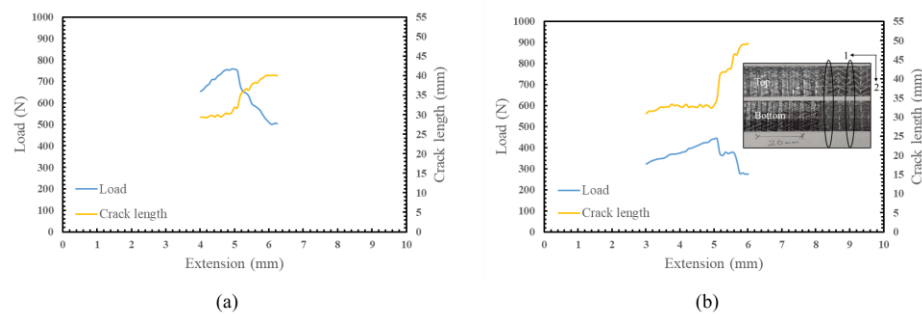


Figure 37: Representative Mode-II interlaminar crack propagation characteristics in (a) unidirectional lamina (b) cross-ply laminate

5.4.2 Resistance curves and fracture toughness

Representative resistance curves (R-curves), in which the interlaminar fracture toughness is plotted versus crack length, under Mode-I and Mode-II loads are shown in Figure 38. R-curves for all specimens may be found in Appendix 12 and Appendix 13. Although a stick-slip behavior was observed in all tested specimens, the fracture toughness value at which the crack first extends from the Teflon insert has been reported as the initiation value (marked as “x” in Figure 38 and reported in Table 2). A linear fit was used after initiation to determine the propagation values, which correspond to the plateau region in R-curves. Except in the cross-ply laminate under Mode-I loading, an increase in the propagation values after initiation can be seen. Resin-rich pockets at the front of Teflon insert and on the path to migration of crack from midplane to 0//90 interface may have caused the additional toughening for initiation in cross-ply laminates under Mode-I loading.

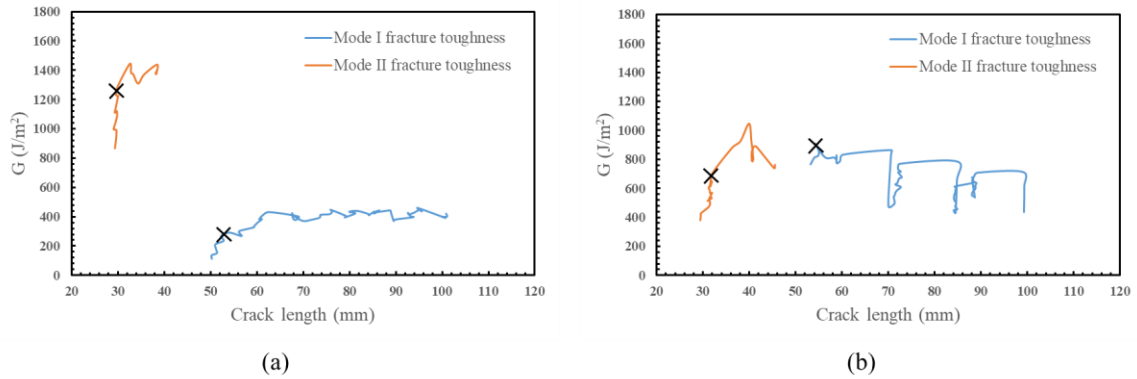


Figure 38: Representative R-curves for (a) unidirectional lamina (b) cross-ply laminates

An increase of approximately 45% may be noted in the Mode-I fracture toughness (G_{Ic}) of cross-ply laminate as compared to the unidirectional lamina. This increase may primarily be attributed to the resistance offered to the crack propagation in cross-ply stacking sequence by the transverse fiber tows. The tows force the crack to follow a wavy path to follow their undulations along the $0//90$ interface. A transversely oriented fiber bundle may also cause the crack to split into multiple cracks. All these phenomena lead to higher effective crack length in the cross-ply laminate and hence, a higher energy dissipation in crack propagation. The crack, by comparison, follows a relatively straight path between two 0° layers in unidirectional lamina, with minor resistance to propagation from stitching sites. The crack, however, stays effectively linear and requires comparatively lower amount of energy to propagate.

Table 2: Interlaminar fracture toughness under Mode-I and Mode-II loads in unidirectional and cross-ply laminates. All the values are reported in J/m^2 .

	Mode-I opening loads		Mode-II shearing loads	
	Initiation	Propagation	Initiation	Propagation
$[0_4]_s$	364 (± 3)	443 (± 45)	1333 (± 256)	1580 (± 316)
$[0_3/90]_s$	1151 (± 230)	645 (± 26)	672 (± 124)	888 (± 87)

The G_{IIc} for propagation in unidirectional lamina is measured to be approximately three times the G_{Ic} . As was discussed in Section 5.4.1.1, a stable crack propagation could be achieved in unidirectional lamina. The reported propagation G_{IIc} values may hence be considered reliable. The presence of cusps has been identified as a key feature in Mode-II delamination (discussed in detail in Section 5.4.3.2). The cusps lead to a larger surface area of crack and has been reported to cause the G_{IIc} to be about 2.4 times higher than the G_{Ic} . The presence of stitching sites further adds to the resistance to propagation. The difference in the fracture toughness values in cross-ply laminate under Mode-I and Mode-II loading conditions was, however, just under 40%. This can be attributed to the nature of reinforcement stacking sequence, as under both the loading conditions, the primary resistance to crack propagation is offered by the transverse tow bundles.

5.4.3 Post-failure characterization

The changes in the post-failure morphology with changes in loading conditions provide a direct insight into distinct micro-mechanisms that contribute to delamination fracture toughness and a means to physically validate the predictive failure criteria.

5.4.3.1 Mode-I loads

SEM investigations of the unidirectional fracture surfaces in this study show an overall rougher appearance (Figure 39, the crack propagates from bottom to top along 1-direction, as indicated by black arrows). The crack propagation occurred very close to the fiber matrix interface in unidirectional composites, as evidenced by presence of matrix on the fibers. Distinct features were observed on the free edges of the specimen versus at the center. As the material present at the free surfaces was unconstrained at one end, it was free to deform, leading to formation of riverlines at the free edges (Figure 39.a.). However, towards the center of the specimen, the material was effectively in a state of plane strain, leading to a planar cleavage (Figure 39.b.) type of fracture surface in resin rich regions.

‘Tidemarks’ (Figure 39.d.) can also be clearly seen on the fracture surface. These discrete bands are usually associated with changes in the crack speed (stick-slip behavior, as was explained in previous section). Areas with higher plastic deformation correspond to areas of crack arrest or slow growth and relatively feature free areas correspond to areas of rapid crack growth. The tidemarks are believed to be a result of blunting at the tip of a sharp crack and are aligned normal to the direction of crack propagation (Greenhalgh E. , 2009).

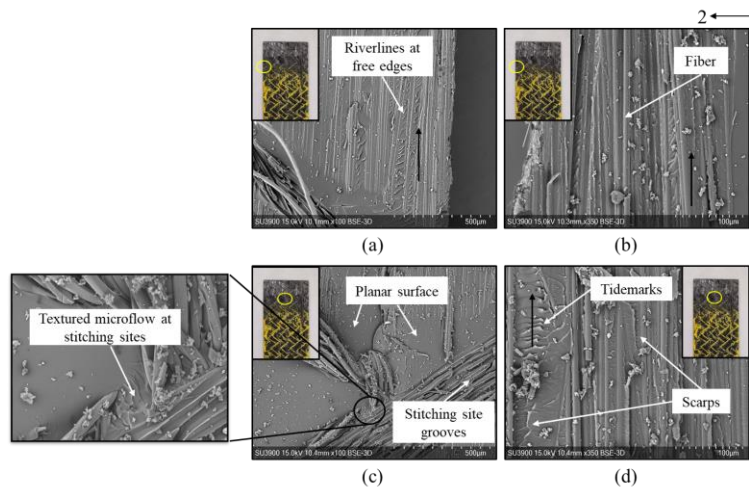


Figure 39: SEM characterization of the fracture surfaces of unidirectional composites under Mode-I loads

In general, the fracture extends along the fibers and spreads into surrounding matrix area, as evidenced by presence of matrix deformation lines extending from fibers, aligned in the direction of crack growth. The convergence of these deformation planes leads to the formation steps, called ‘scarps’ (Greenhalgh E. , 2009). Moreover, grooves left behind by pullout of stitches can be clearly seen on the failure surface. Local textured microflow of matrix can be observed too.

The fracture surfaces of the tested cross-ply specimens are shown in Figure 40, in which the direction of crack propagation is along 1-direction from bottom to top. Unlike in unidirectional composites, no major distinction was found between the feature on the free edges and at the center of the specimen. Riverlines and scarps, diagnostic of local plastic deformations, could be observed on both, free edges and center.

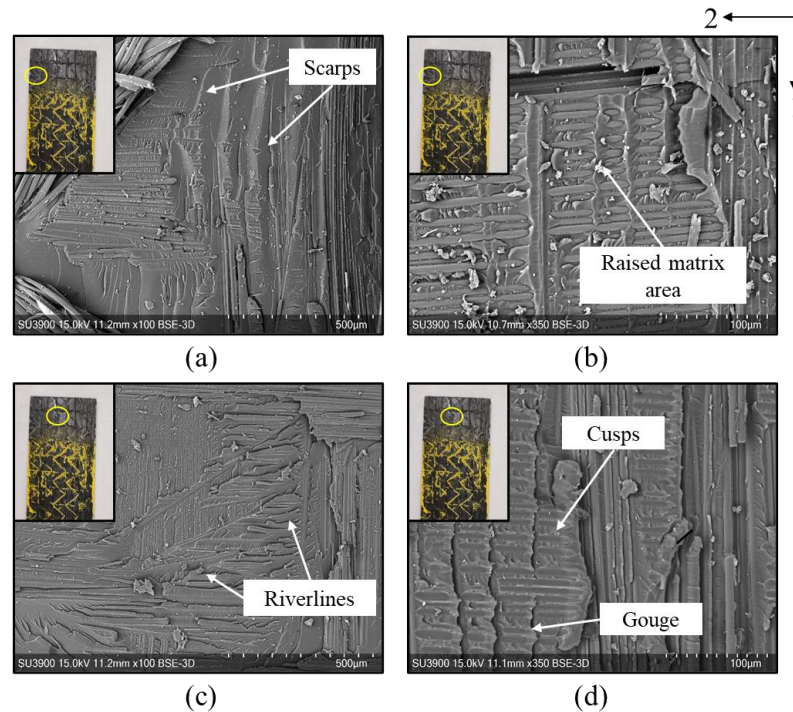


Figure 40: SEM characterization of the fracture surfaces of cross-ply laminates under Mode-I loads

Unlike in unidirectional composites, cusps and gouges can be seen on the failure surfaces of the cross-ply laminates. Cusps, also referred to as ‘hackles’, ‘flakes’, ‘lacerations’ or ‘serrations’ (Greenhalgh E. , 2009), appear as inclined platelet-like structures on the surface and may be formed as a result of local sliding of surfaces (discussed in detail in subsequent section). Deep ‘gouges’ (Greenhalgh E. , 2009), extending underneath the surface, may be seen accompanying the cusps. The gouges occur at the base of the cusps, where several cusps are aligned along a line. The spacing between the gouges however seems to vary.

5.4.3.2 Mode-II loads

Fractographic observations reveal that the crack primarily propagates along fiber/matrix interface under Mode-II loads in both, unidirectional and cross-ply laminates. This is supported by the presence of bare fibers and clean fiber tracks left behind by pulled out fibers on the failure surfaces. Unlike in under unidirectional laminae subjected to Mode-I opening loads, no discernable distinction could be made between features on free edges versus at the center.

The dominant feature in both the investigated laminates was the presence of cusps. The cusps are formed owing to a relative shearing of two surfaces. The mechanism of formation of cusps may be understood by considering the stress state in front of the crack tip, which consists of a tensile traction angled at 45° . As the loads increase, the cracks grow along the tensile traction vertically in the interlaminar resin rich region and then rotate locally at the interface boundary. This leads to the formation of cusps, which detach from the surface, leaving behind the inclined platelet-like features. Generally, the cusps coalesce with the adjacent cusps, leading to one surface retaining cusps and the matching surface being left with the cusp marks. These are labelled as “scallops” in Figure 41. These features may be influenced by numerous factors such as fiber spacing and matrix toughness. In addition to cusps and scallops, gouges were also observed in cross-ply laminates.

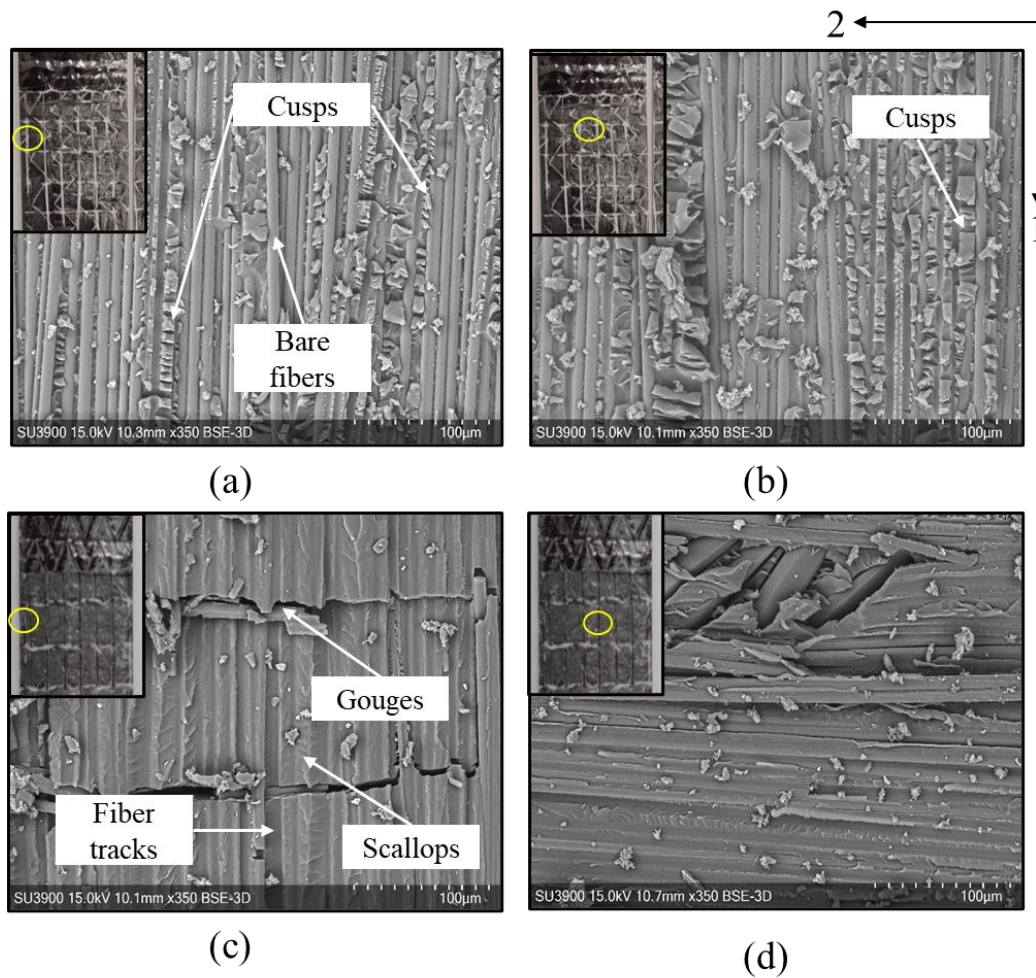


Figure 41: (a-b) SEM characterization of the fracture surfaces of unidirectional composites under Mode-II loads (c-d) SEM characterization of the fracture surfaces of cross-ply laminates under Mode-II loads

Chapter 6

6 Results: Tensile damage in non-crimp fabric composites

The damage in the NCF composites with increasing load under quasi-static tension is connected to the global stress-strain response (Section 5.1) in this chapter. The chapter starts with a discussion on the characterization of damage in unidirectional lamina with the help of microscopy techniques. As the tensile failure in unidirectional lamina is unstable, it was not possible to trace the initiation and propagation of damage. Next, the initiation and propagation of damage in multidirectional laminates was investigated. This analysis was accomplished using edge replication technique (Section 4.3.2). The growth of different damage modes is compared and connected to the underlying mechanics, driven by the stacking sequences. Finally, the damage growth is connected to the energy dissipated in individual damage modes with loading-unloading tests.

6.1 Post-failure damage characterization of unidirectional composites

6.1.1 Failure under axial tension

The post-failure images of the specimens are shown in Figure 42, where the specimens were loaded along 1-direction. The composite specimens failed such that the resulting fracture plane was almost flat and oriented perpendicular to the direction of fiber alignment and by extension, also the direction of loading. No significant fiber breaks were observed in the specimen away from the fracture plane (Figure 42.b.). This indicates that all the fibers that failed were present on the same plane.

A closer inspection of the failure surface using SEM (Figure 42.c. and Figure 42.d.) revealed presence of lines radiating from a local point of origin, marked as 'x' in Figure 42.d. The sites marked as 'x' act as local crack initiation sites leading to the failure of the fibers. The presence of radial lines originating from these local sources of damage on the fiber ends may be used to infer the local growth directions. A failed fiber effectively induces failure in the neighboring fibers, providing a convenient means to be able to determine direction of crack growth within a local bundle or cluster of fibers. Plastic

deformation in the matrix is also observed in the regions where fibers are separated by resin. This indicates the transfer of stress from a site of broken fiber to adjacent fibers through the resin material, where the fibers are not in direct contact with each other. Furthermore, relatively short fiber pull-out lengths suggest strong fiber-matrix adhesion, which nominally translates into efficient stress transfer between fibers.

Based on the post-failure observations, it may be said the failure process in unidirectional composites with breakage of a single fiber is due to a possible local defect in the fiber. A single broken fiber then induces failure in neighboring fibers, making the material further compliant. The failure of multiple neighboring fibers in a cluster on the same plane eventually leads to the catastrophic failure, similar to what has been reported in the literature (Raz-Ben Aroush, et al., 2006). It is, however, unclear from the available data if multiple such clusters of fiber failure occur simultaneously on the fracture plane.

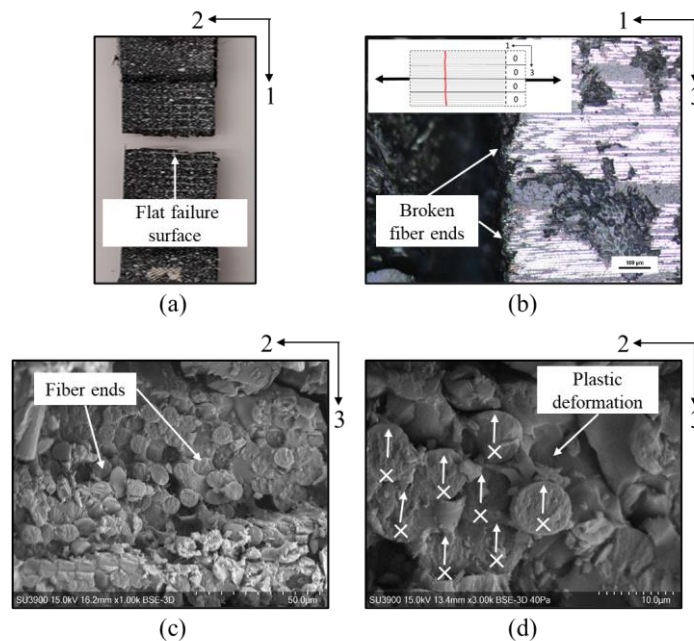


Figure 42: (a) Specimen failed under axial tension (b) Image of the edge of failed specimen taken using optical microscope (c, d) Images of the failed surface taken using SEM

6.1.2 Failure under transverse tension

The unidirectional composites in transverse tension exhibit a brittle, cleavage type of fracture with a smooth fracture plane (Figure 43.a.; The fibers are aligned along 1-direction and the specimen is loaded along 2-direction). The fracture plane is perpendicular to the direction of loading, i.e. along the direction of carbon fiber tows. Optical microscopic observations of the edge of the specimen revealed that the fracture plane propagated through the tows (Figure 43.b.). High magnification images using SEM of the fracture surface showed the presence of pull-out of the supporting glass yarns, resin-rich areas in the vicinity of the supporting yarns and mostly bare fibers. These features are indicative of failure of the material along the fiber-matrix interface by debonding.

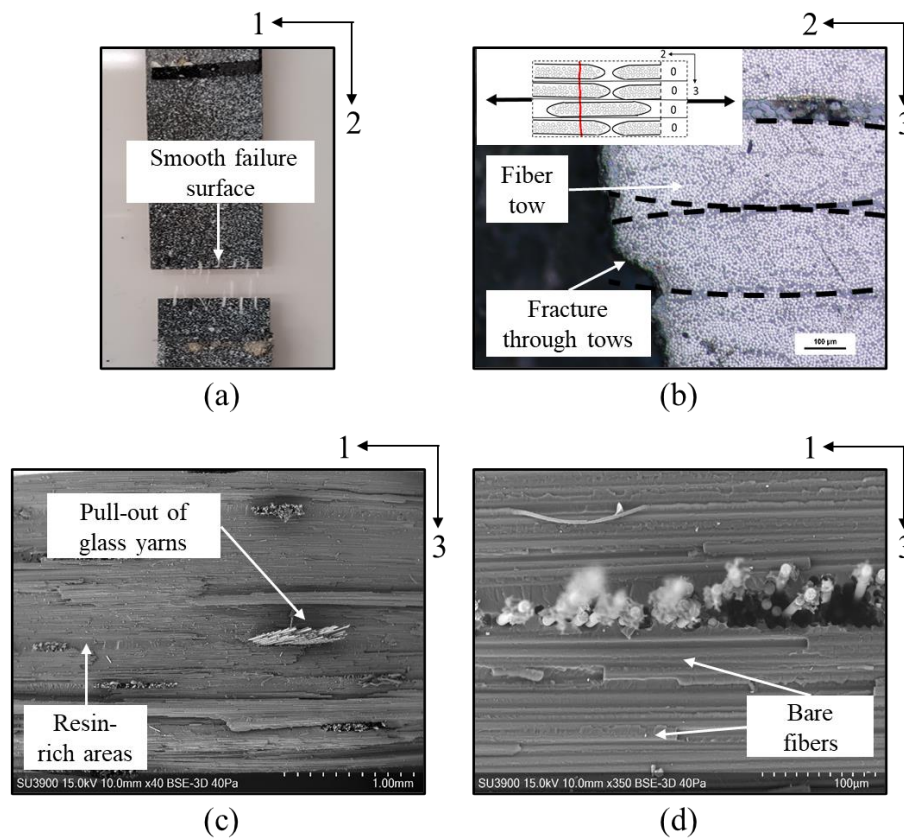


Figure 43: (a) Specimen failed under transverse tension (b) Image of the edge of failed specimen taken using optical microscope (c, d) Images of the failed surface taken using SEM

6.2 Damage in multidirectional composites

6.2.1 Virgin specimens

Images of replicas taken from the edges of untested specimens revealed that there was no damage prior to loading (Figure 44). For reference, the 0° plies were oriented along the laminate y-direction, while the laminate x-direction was normally aligned with loading direction.

The tows in a single NCF layer are stitched together with low density linear polyester fiber yarns. The stitching yarns tend to cause resin-rich pockets between carbon fiber tows, while transversely oriented supporting glass fiber yarns influence the localized resin layers between adjacent plies (encircled in Figure 44).

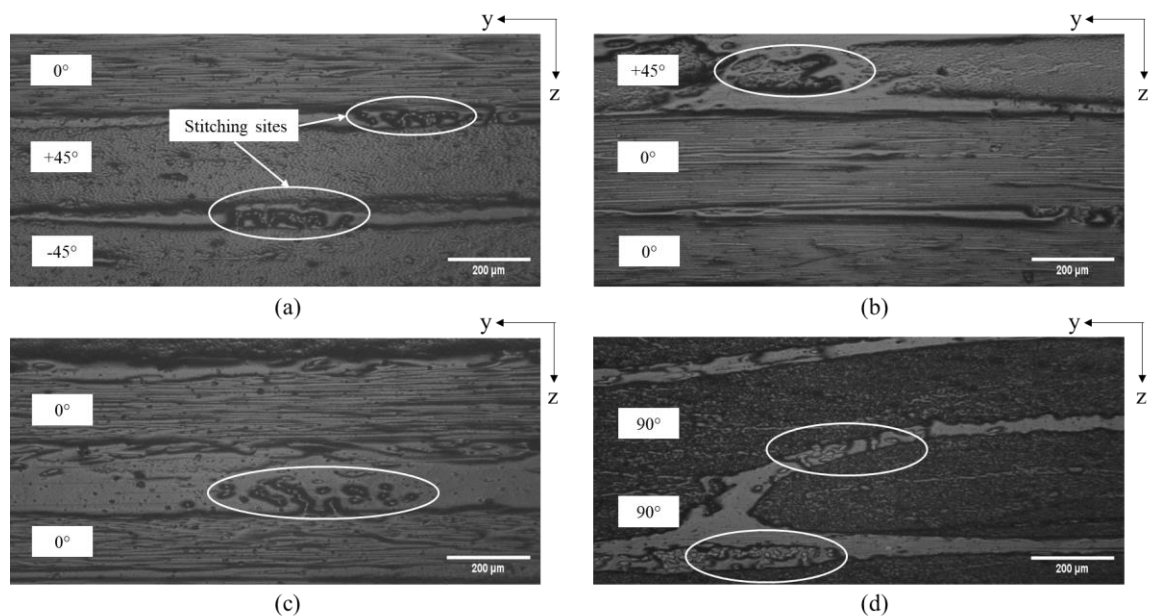


Figure 44: Edge replicas of virgin (a) $[0/\pm 45/90]_s$ laminate (b) $[90/\pm 45/0]_s$ laminate (c) $[\pm 45/0]_2$ laminate (d) $[\pm 45/90]_2$ laminate

6.2.2 Damage evolution under quasi-static tension

6.2.2.1 $[0/\pm 45/90]_s$ and $[90/\pm 45/0]_s$ laminates

The stress-strain curves of the tested specimens upon interruptions at pre-defined strain values, as per the process described in the previous section, are shown in Figure 45. Both laminates exhibited a linear-elastic response through all the loading steps. Therefore, it was not possible to define strain at damage onset based on the stress-strain curves alone. However, a reduction in the slope of the stress-strain curves with an increasing strain was observed, indicating the occurrence and development of damage within the materials.

Damage was first observed as localized cracks at the stitching sites between the 90° plies after a strain of approximately 0.29% in the $[0/\pm 45/90]_s$ laminate (Figure 46). As the strain was increased to 0.61%, cracks were observed to extend through the thickness of the 90° plies, where the majority of these cracks originated from the damaged stitching sites. Some of the 90° ply cracks caused cracks to initiate in the adjacent -45° ply.

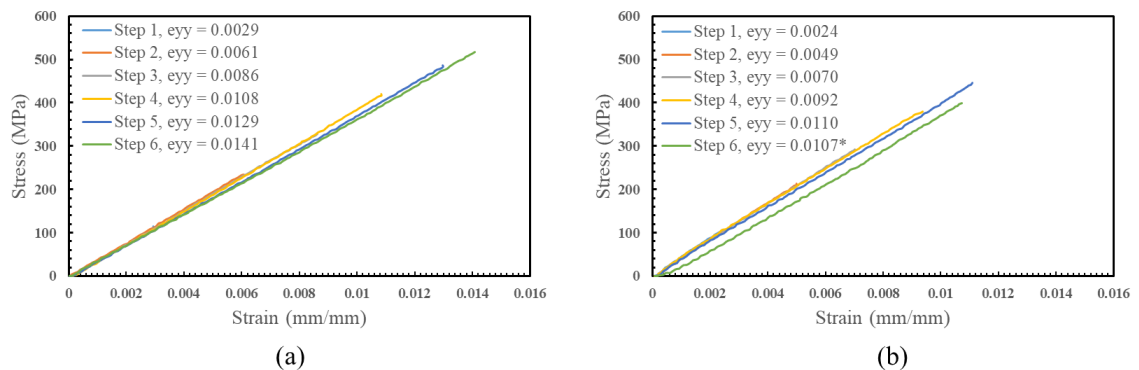


Figure 45: Stress-strain curves from interrupted tension tests for (a) $[0/\pm 45/90]_s$ laminate (b) $[90/\pm 45/0]_s$ laminate

Ply cracks in the 90° and -45° plies continued to multiply with increasing strain and saturated once the applied strain exceeded 0.61% (Figure 46). Once the strain reached 0.86% (Figure 46), ply crack saturation is reached in 90° plies and the cracks initially observed at the stitching sites grew into delamination cracks at the interface between the 90° plies. These cracks will be referred to as 90/90 delamination cracks. Since the $+45^\circ$ and -45° plies were perpendicular, ply cracks in the -45° plies did not cause ply cracks to

initiate in the $+45^\circ$ plies. Instead, delamination cracks formed between the $+45^\circ$ and -45° plies, which will be referred to as $+45/-45$ delamination. Extension of the $90/90$ and $+45/-45$ delamination cracks were widespread after a strain of 1.29% (Figure 46), which was just before specimen failure.

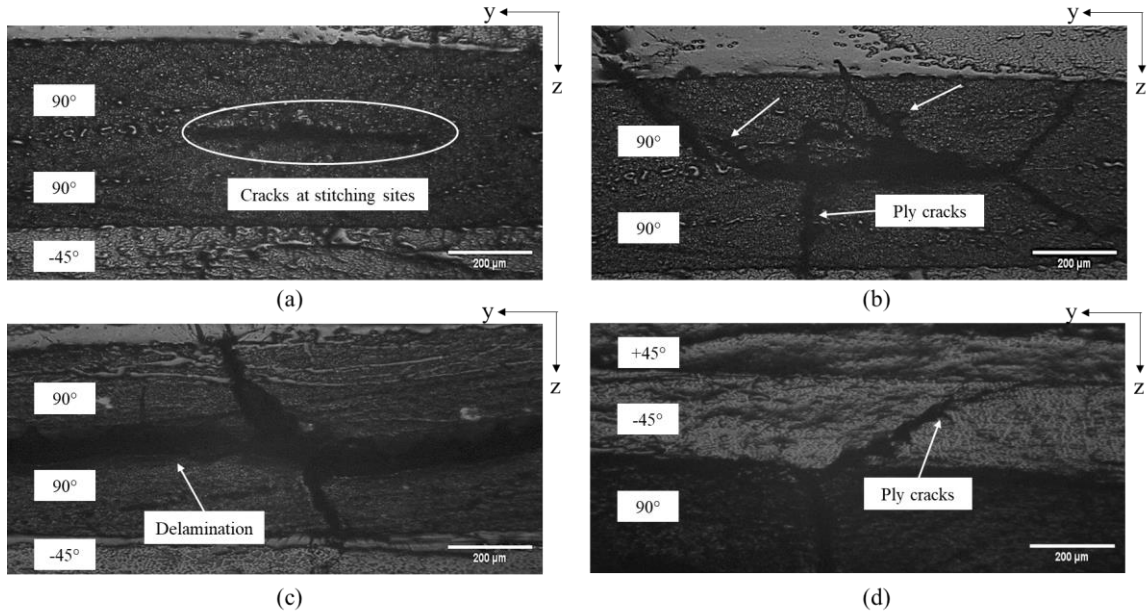


Figure 46: Damage features in the $[0/\pm 45/90]_s$ laminate under tension at (a) 0.29% strain (b) 0.61% strain (c) 0.86% strain (d) 1.29% strain

On the other hand, damage in the $[90/\pm 45/0]_s$ laminate along the x-direction (Figure 47) was observed to initiate after an applied strain of approximately 0.70%. The strain at onset of damage was likely higher for transverse loading since cracks did not initiate at the stitching sites. Uniformly spaced cracks were observed in the 0° plies, where some of these cracks initiated ply cracks in the adjacent $+45^\circ$ ply, as in the $[0/\pm 45/90]_s$ laminate. Cracks continued to multiply in 0° and $+45^\circ$ plies with increasing strain. The reduced spacing between the cracks lead to overlapping of the relaxed stress fields in the crack vicinities due to which the stresses in between two neighbouring cracks were not high enough for a new crack to form (i.e., crack shielding). Ply cracks seemed to saturate at this point, which was observed at approximately 1.10% strain. Thereafter, delamination crack started to grow at the ± 45 ply interface, which preceded specimen failure.

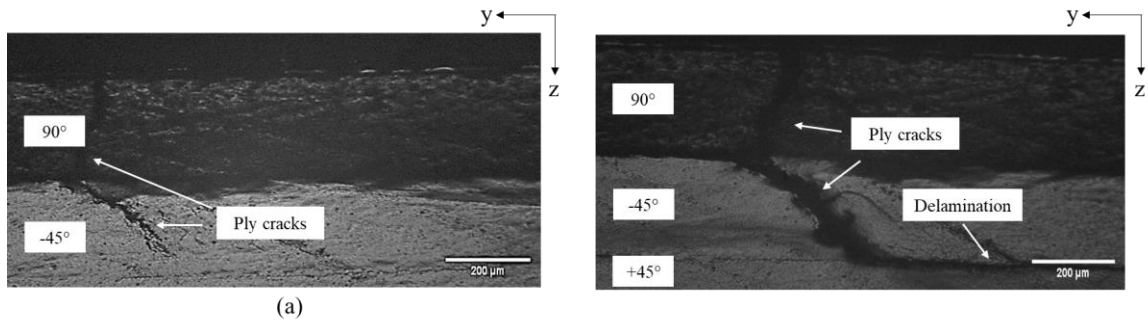


Figure 47: Damage features in the $[90/\pm 45/0]_s$ laminate under tension at (a) 0.70% strain (b) 1.10% strain

6.2.2.2 $[\pm 45/0_2]_s$ and $[\pm 45/90_2]_s$ laminates

The response of the $[\pm 45/0_2]_s$ laminate was dominated by the on-axis 0° plies, which resulted in a linear elastic stress-strain behaviour (Figure 48.a.). In contrast, the stress-strain response for the loaded $[\pm 45/90_2]_s$ laminate exhibited nonlinearity prior to reaching the peak strain (Figure 48.b.).

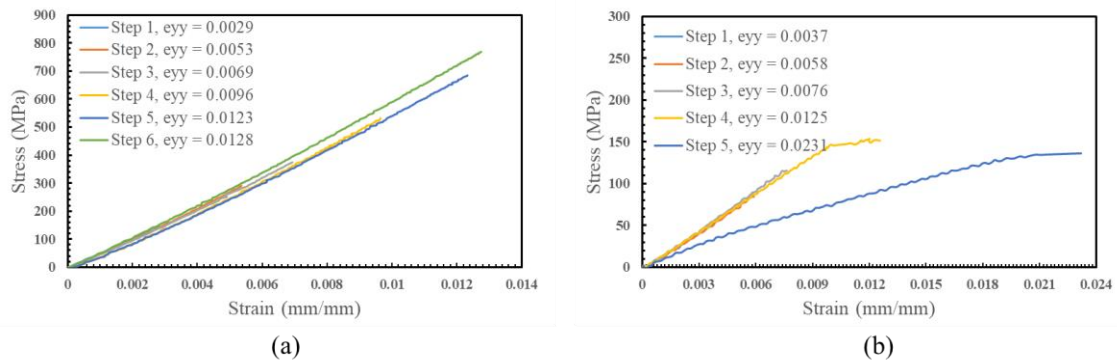


Figure 48: Stress-strain curves from interrupted tension tests for (a) $[\pm 45/0]_s$ laminate (b) $[\pm 45/90]_s$ laminate

In the $[\pm 45/0_2]_s$ laminate, damage initiation was observed in the form of cracks at stitching sites at 0.69% (Figure 49.a.). Cracking in multiple stitching sites was observed as the strain was increased. Minor cracking was observed in -45° ply at 1.23% strain (Figure 49.b.), which was just before specimen failure. The minor cracks in the -45° ply are not counted as ply cracks since they do not span the entire ply thickness. The failure is expected to have occurred when multiple neighbouring fibers present in the same plane in the 0° plies fractured, rendering the specimen incapable of carrying further load.

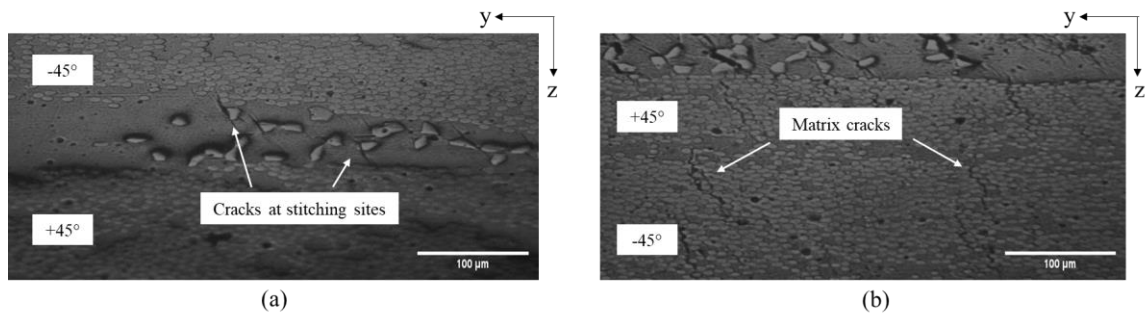


Figure 49: Damage features in the $[\pm 45/0_2]_s$ laminate under tension at (a) 0.69% strain (b) 1.23% strain

The damage evolution process in $[\pm 45/90_2]_s$ laminate was comparable to the damage progression in the $[0/\pm 45/90]_s$ laminate. Cracks were observed at the stitching sites between 90° plies at 0.37% strain, as can be seen in Figure 50.a. As the strain was increased to 0.58% (Figure 50.b.), the cracks in stitching sites were found to nucleate ply cracks in 90° plies. However, the 90° ply cracks instantly saturated and the damage progression was then primarily in the form of $90/90$ delamination cracks and ply cracks in $+45^\circ$ plies. Once these two damage modes stopped growing at 1.25% strain (Figure 50.d.), the primary damage growth was in the form of delamination crack along the $+45/-45$ ply interface up to a strain of 2.31%, after which the specimen failed.

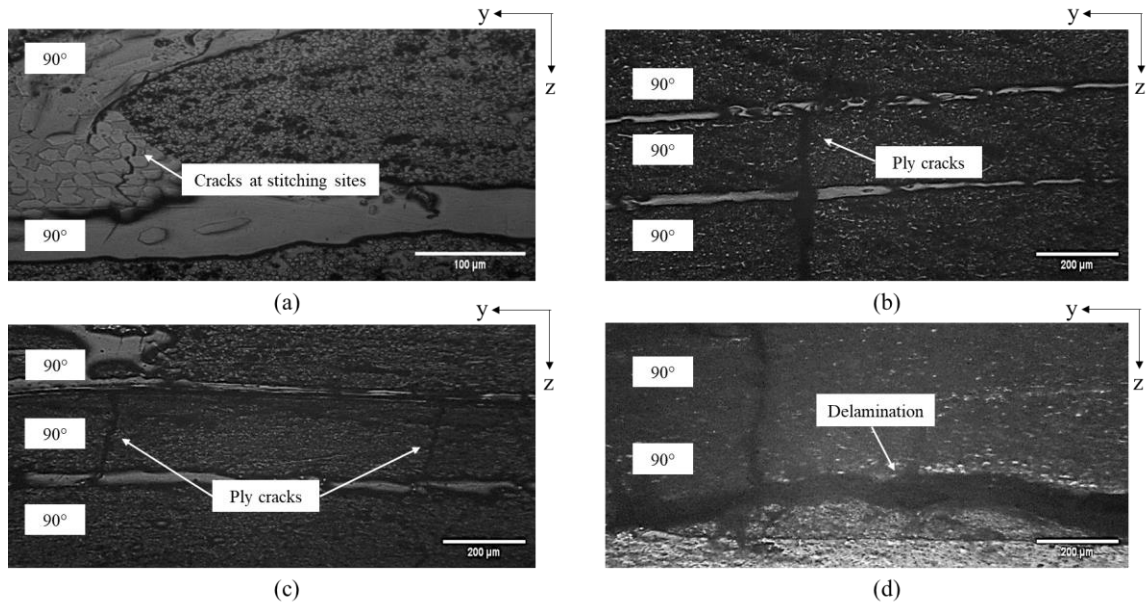


Figure 50: Damage features in the $[\pm 45/90]_s$ laminate under tension at (a) 0.37% strain (b) 0.58% strain (c) 0.76% strain (d) 1.25% strain

6.2.2.3 Damage quantification and stiffness degradation

The damage modes observed in the studied laminates under axial and transverse tensile loads were quantified and correlated with stiffness degradation (Figure 51). The total damage area is considered to be summation of ply crack and delamination crack surface areas. Ply cracks and delamination cracks were both assumed to span the entire width of the specimen. The number of ply cracks was multiplied by width and ply thickness to calculate area associated with ply cracking. The delamination area was determined by multiplying measured delamination lengths and specimen width. Clear drops in laminate stiffness can be seen corresponding to increase in damage areas (Figure 51). Laminate stiffness was calculated from the stress-strain curves of the interrupted tests (Figure 45 and Figure 50) within the strain range of 0.1%-0.2%. Although the stiffness of both, $[0/\pm 45/90]_s$ and $[90/\pm 45/0]_s$ laminates, drops to 87% of the initial stiffness (E_0) at the end of the test, the damage area is higher for the $[0/\pm 45/90]_s$ laminate. The most significant drop in laminate stiffness was observed in the case of $[\pm 45/90]_s$ laminate, which was about 57% of E_0 . The major contribution to stiffness drops in $[0/\pm 45/90]_s$ laminate and $[\pm 45/90]_s$ laminate came from 90/90 delamination crack (Figure 51).

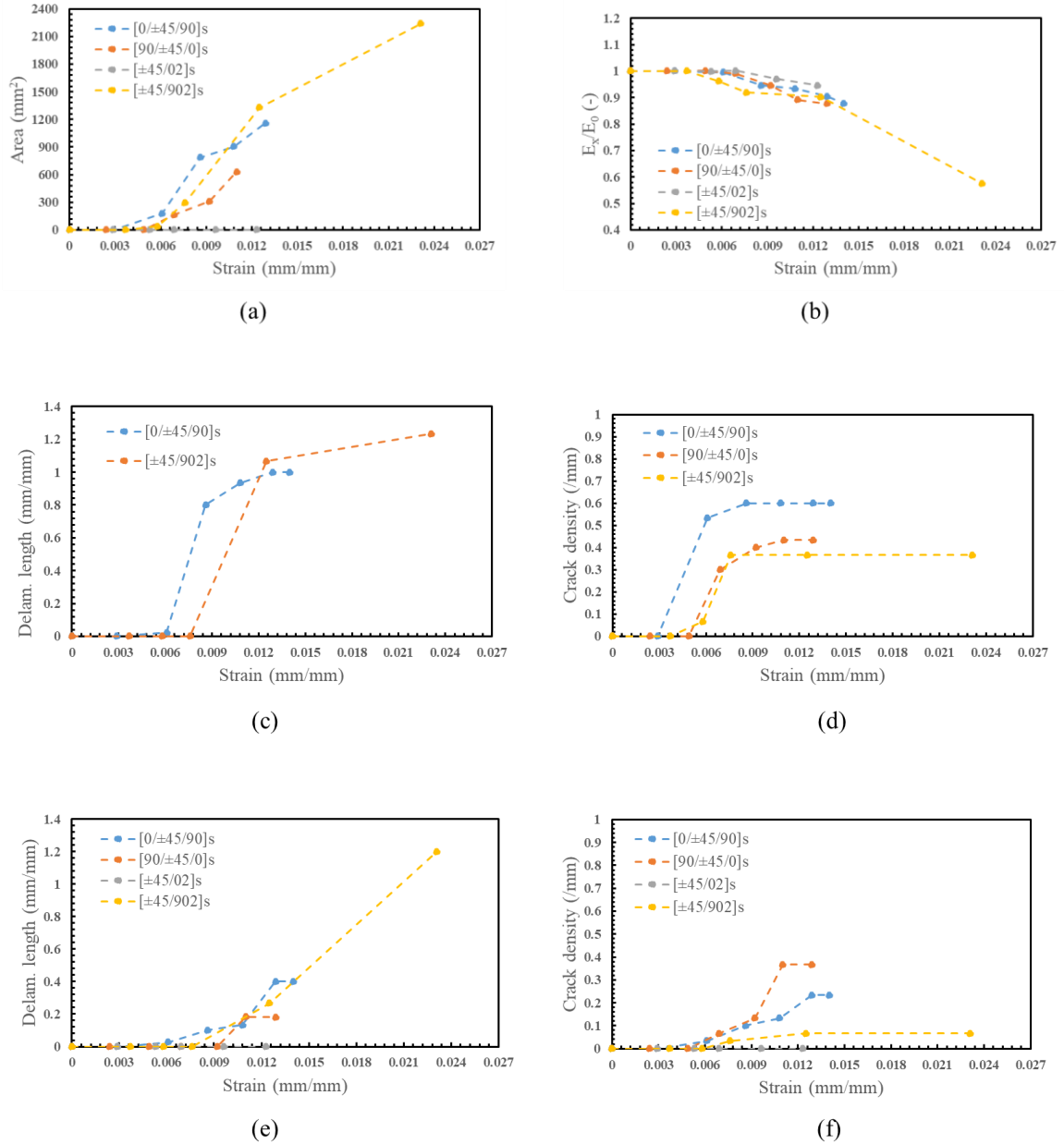


Figure 51: Influence of stacking sequence on (a) total damage area (b) laminate stiffness degradation (c) 90/90 delamination crack growth (d) ply crack multiplication in 90° plies (e) +45/-45 delamination growth (f) ply crack multiplication in 45° plies

The stacking sequence and ply thickness also have a pronounced effect on the onset of ply cracks in 90° ply due to ply constraint effects. The 90° plies are sandwiched between 0° plies in the $[0/\pm 45/90]_s$ laminate and are more greatly constrained, which leads to multiple cracks originating from a single damaged stitching site and hence, a higher density of cracks as compared to the $[90/\pm 45/0]_s$ laminate in which the 90° plies are unsupported at one end (Figure 51). Further, an increase in the thickness of the 90° plies leads to a reduced effective constraining. This causes an onset of ply cracks in 90° ply at lower stresses (Parvizi, Garrett, & Bailey, 1978). Cracking in the 45° plies (Figure 51) on the other hand, seems to be more influenced by crack density in 90° plies and the presence of $90/90$ delamination crack; however, this is inconclusive at this stage. The $+45/-45$ interface was the most prone to delamination crack growth, which accelerated only after the saturation of other damage modes (Figure 51). Finally, a higher concentration of 0° plies, as is the case in $[\pm 45/0]_s$ layup, suppresses all other damage modes. The failure then is due to a tensile fracture of multiple 0° fibers in close vicinity.

6.2.3 Post-failure damage characterization

As was discussed in the previous sections (Section 6.2.2), although the actual process of damage growth is dependent on the stacking sequences and loading conditions, the catastrophic failure of the test coupons is dictated by the failure of 0° plies. Visual inspection of the failed coupons revealed that the different plies failed on different planes, confirming the occurrence of delamination and matrix cracks prior to the final failure of the specimen. The scanning electron microscopy images of the failed surfaces of the multidirectional laminates are shown in Figure 52. Similar features may be observed on the 0° , 45° and 90° plies, irrespective of the ply stacking sequence and loading condition. The different laminates will hence not be discussed separately in this section.

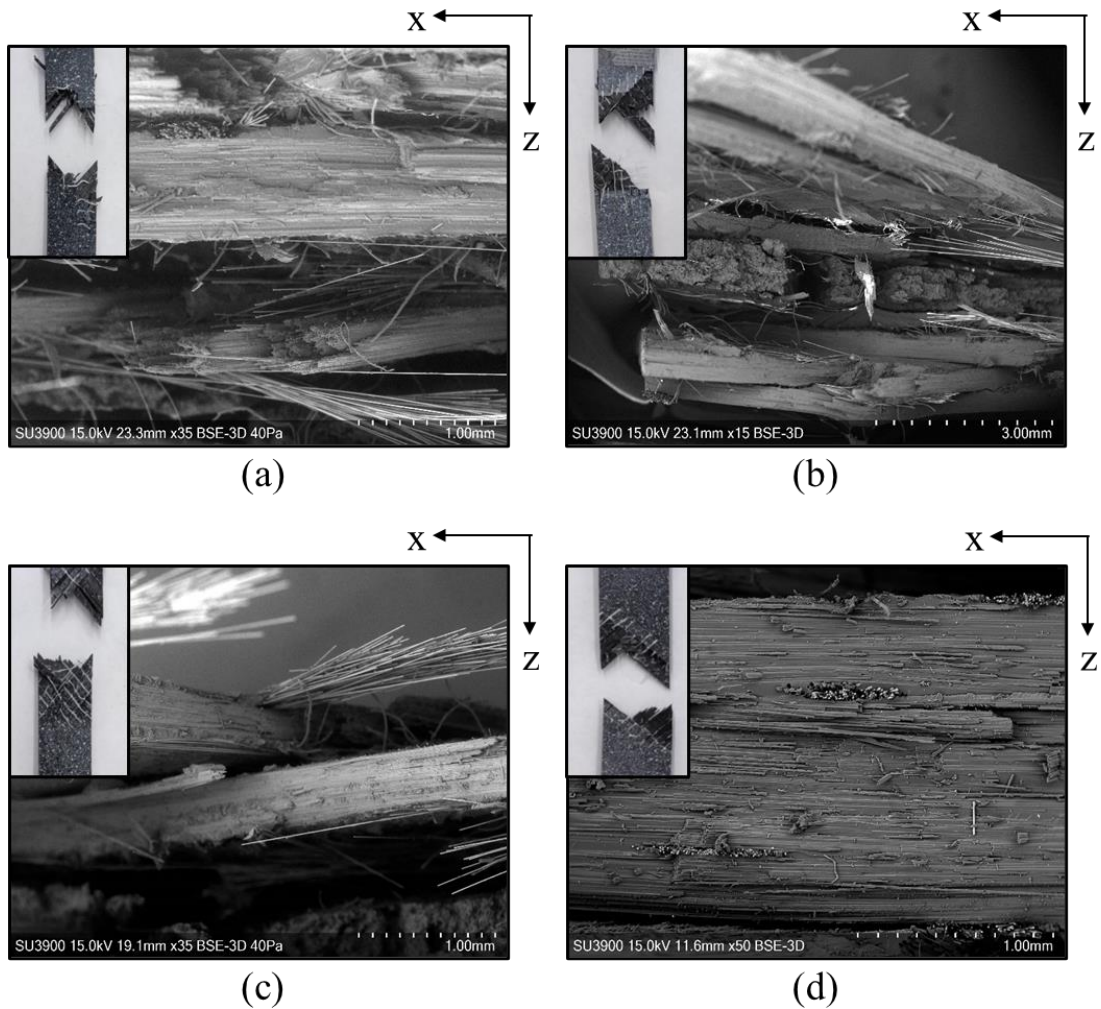


Figure 52: Post failure surfaces of (a) $[0/\pm 45/90]_s$ laminate (b) $[90/\pm 45/0]_s$ laminate (c) $[\pm 45/0]_2$ laminate (d) $[\pm 45/90]_2$ laminate

Some of the general features observed on the surfaces of 0° and 90° plies in the laminates were similar to the distinguishing features observed on the surfaces of unidirectional composites (Section 6.1). The load bearing 0° plies were characterized by a rugged surface and radial markings extending from a local defect on broken fibers (Figure 53.a.). On the other hand, the surfaces of 90° plies were smooth with bare fibers and pockets of resin-rich areas, indicative of failure by fiber-matrix debonding. The edge images of the 90° plies revealed that the catastrophic crack passed through the tows and not along the tow boundary (Figure 53.d. and Figure 53.f.).

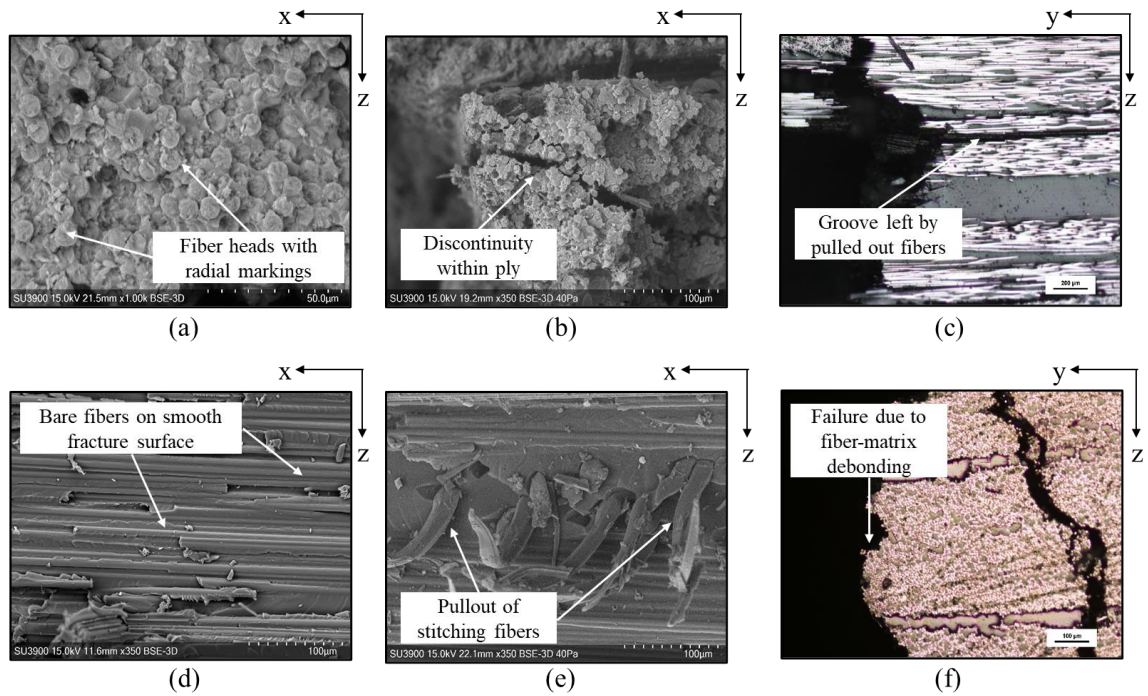


Figure 53: (a-b) Post failure surface of 0° plies (c) Edge image of failed 0° ply (d-e) Post failure surface of 90° plies (f) Edge image of failed 90° ply

Other than the common general features observed on the surfaces of 0° plies, unlike in unidirectional composites, the failure was non-coplanar. The surface (Figure 53.b.) and edge images (Figure 53.c.) revealed the presence of grooves left behind by the pulled-out fibers. This indicates that fiber breaks occur at multiple points throughout the ply. The locations of these fiber breaks may correspond to breaks in the adjacent compliant plies. The single fiber breaks then cause failure of neighboring fibers, which then get pulled out as in clusters or as a bundle upon catastrophic failure, leaving behind the grooves. Similarly, in the 90° plies, in addition to the features observed in transversely loaded unidirectional composites, pull-out of stitching polyester fibers was observed on the surface. Localized plastic deformation was observed in the immediate vicinity of the pulled-out stitching fibers. This can be attributed to the continued stress transfer to the 90° plies through the adjacent stiffer plies.

A close inspection of failed 45° plies reveals the presence of hackles (Figure 54.a.), which are indicative of in-plane shear within the lamina. However, as was also observed in the damage evolution process (Section 6.2.2), the ± 45 interface is most prone to delamination owing to its orthogonality. The presence of delamination during the fracture process between $+45^\circ$ and -45° ply effectively degrades the level of constraint on the plies, allowing them to rotate in the direction of loading, which eventually leads to the tensile fracture of the 45° plies along the tow boundary (Figure 54.b. and Figure 54.c.). The features observed on the surfaces of 45° plies were consistent across the two tested laminates under the axial and transverse loading conditions.

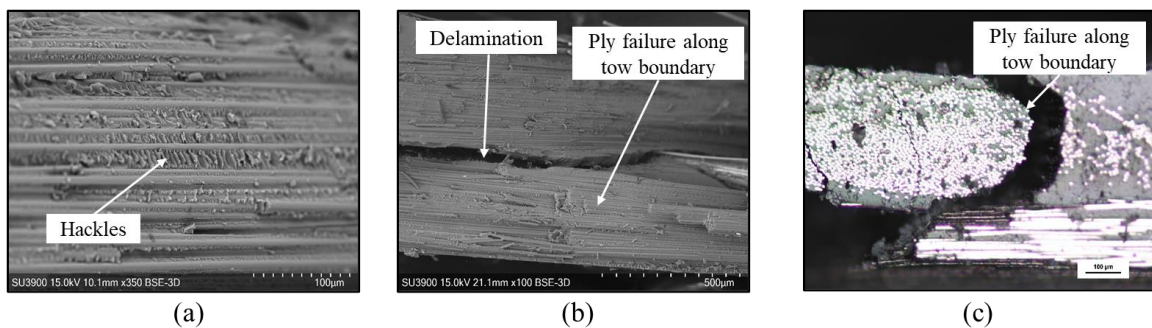


Figure 54: (a-b) Post failure surface of 45° plies (c) Edge image of failed 45° ply

6.2.4 Energy dissipation in damage

The damage evolution and post-failure characteristics of multidirectional laminates under quasi-static tensile loads were discussed in Section 6.2.2 and Section 6.2.3. Damage initiation was observed as cracks in the stitching sites, more specifically along the fiber/stitching thread interface. The cracks in the stitching sites were later found to nucleate other forms of damage, primarily ply cracks and delamination. The rates of growth of the damage forms depended on the stacking sequence and geometric parameters. The failure, however, was governed by the brittle failure of load-bearing fibers. The post-failure fractography revealed that the ply failure in transverse plies was through the fiber tows and the failure in the plies oriented at 45° was along the tow boundary. This section correlates the damage with the energy dissipated in the creation of damage.

The energy dissipated in damage was calculated using two strategies. In the first strategy, the energy dissipated in the damage was calculated as an arithmetic sum of energies dissipated in the individual damage modes. The energy dissipated in the individual modes is a product of the area of a particular damage mode and critical strain energy release rates associated with that mode. As was described before, ply cracks and delamination along $\pm 45^\circ$ interface were the two primary damage modes in the laminates. The damage areas are already quantified in the Section 6.2.2.3. Further, from the fractographic observations, it may be said that the damage occurs primarily under Mode-I loading conditions. Therefore, the critical strain energy release rates for matrix ply cracks is taken as 200 J/m^2 (Hull & Clyne, 1996), which is average fracture toughness reported for epoxy resins. As the $\pm 45^\circ$ interface was found to be the most susceptible to delamination growth, the fracture toughness value for growth of delamination cracks along a cross-ply interface may be used here. The Mode-I fracture toughness for propagation of delamination in a cross-ply was already measured in this study as 645 J/m^2 (Section 5.4.1.1). The sums of products of the critical strain energy release rates and damage areas yielded the total amount of energy dissipated in the creation of damage in the laminates. The stiffness drops corresponding to the damage were calculated from the stress-strain curves in the 0.1-0.2% strain range of the interrupted tests conducted to monitor the damage evolution (Section 6.2.2.3).

The second strategy for energy dissipation computation entailed performing loading-unloading tests. The test coupons with a similar geometry as used for the characterization and damage evolution tests were used for these displacement-controlled tests. The specimens were loaded in increments of 0.2 mm until failure at a cross head displacement rate of 2 mm/min. The cross head was brought back to a displacement value very close to 0 mm at the end of every loading cycle. The stress was calculated as a ratio of load readings from the load-cell and area and the strain in the tests was measured using DIC. The stress-strain curves for the tested laminates are shown in Figure 55. The energy dissipated in each step was calculated as a product of the area enclosed by the loop formed by the loading-unloading curves and the volume of the specimen used for strain measurement. The laminate stiffness was measured from the loading part of each step in the 0.1-0.2% strain range.

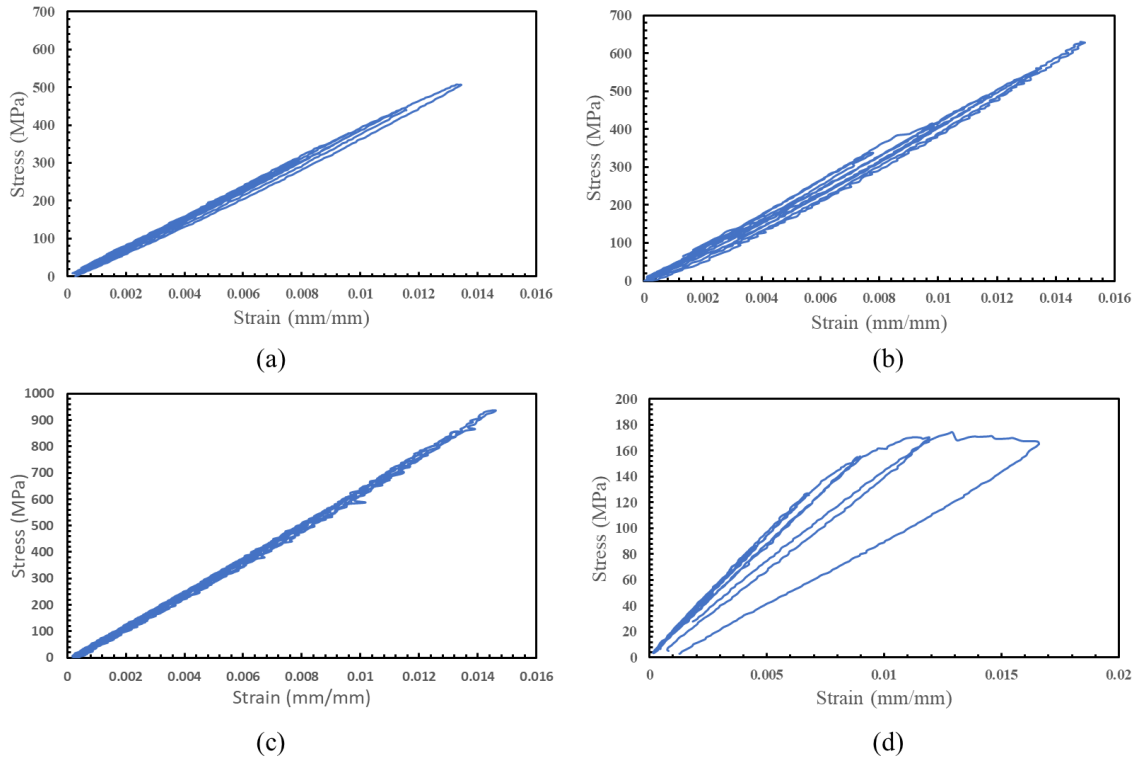


Figure 55: Stress-strain curves from loading-unloading test for (a) $[0/\pm 45/90]_s$ laminate (b) $[90/\pm 45/0]_s$ laminate (c) $[\pm 45/0/2]_s$ laminate (d) $[\pm 45/90/2]_s$ laminate

The energy dissipation and stiffness drop from both the strategies are compared in Figure 56. ‘DE’ stands for ‘Damage Evolution’ and represents results from the first strategy (from the damage evolution tests). ‘L-uL’ stands for ‘Loading-unLoading’ and is representative of the results from the second strategy.

The energy dissipation and laminate stiffness trends are in general agreement for all the tested laminates. The energy dissipation value in damage evolution tests is higher than the loading-unloading tests at around 0.8% (Figure 56.a.) for $[0/\pm 45/90]_s$ laminate. A possible cause for the higher energy dissipation could be due to a higher delamination length in the damage evolution test specimen. As it was described in Section 6.2.2.1, the key damage mechanism was identified as 90/90 delamination. It was formed by joining of cracks in the transverse cracks, whose crack density is governed by the cracks in stitching sites. The occurrence of cracks in the weak stitching sites is stochastic. A higher number of cracks in stitching sites at lower strains may result in higher transverse crack

density and longer delamination lengths at higher strains, leading to higher energy dissipated. The DE specimen failed at a lower strain in the $[90/\pm 45/0]_s$ laminate (Figure 56.b.). The failure was governed by the failure of the load-bearing fibers, which is also a statistical phenomenon (as was described in Section 2.3.2.1, Section 6.1.1 and Section 6.2.3).

A relatively high amount of energy dissipation was recorded in the case of $[\pm 45/0_2]_s$ laminate at a high strain of 1.1%. The exact cause of this relatively higher energy dissipation is inconclusive at this stage, but could have been caused due to damage during an unloading cycle.

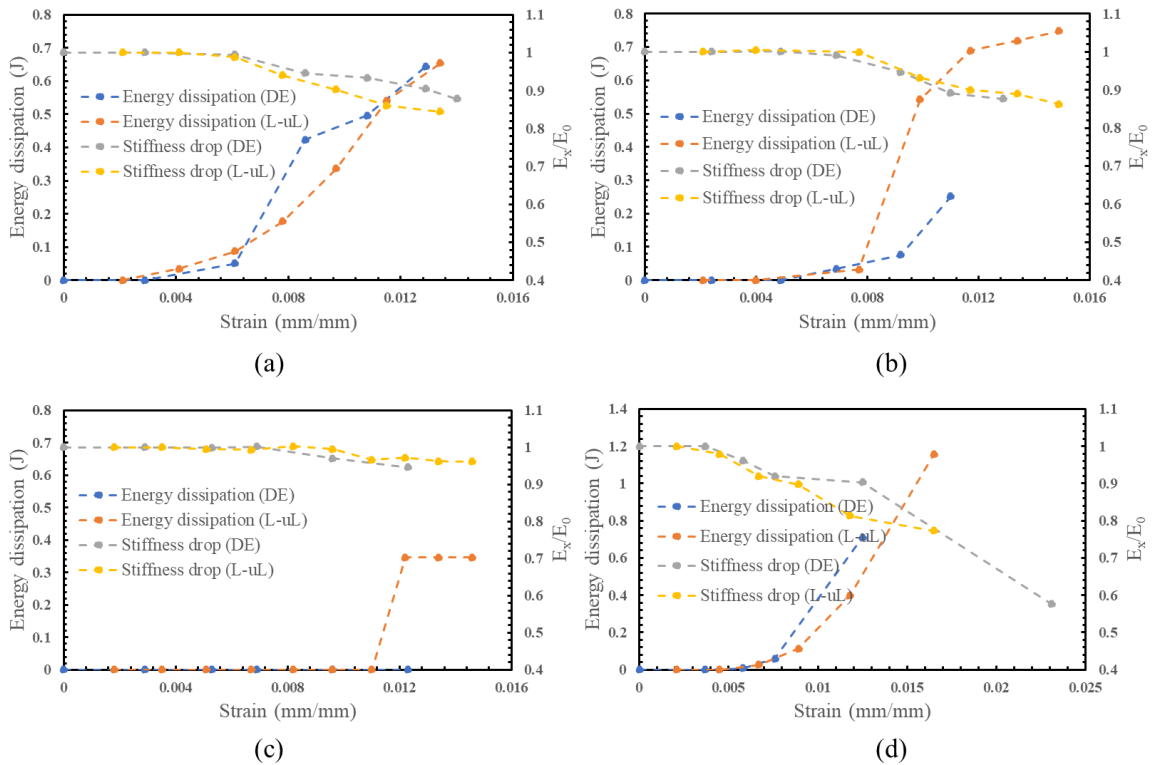


Figure 56: Energy dissipated in and stiffness drops in (a) $[0/\pm 45/90]_s$ laminate (b) $[90/\pm 45/0]_s$ laminate (c) $[\pm 45/0_2]_s$ laminate (d) $[\pm 45/90_2]_s$ laminate

It is, however, important to note the caveats and assumptions made in this analysis. The analysis ignores the energy lost as heat. It also ignores the energy dissipated in any probable secondary damage mechanisms like fiber pull-out, friction work due to fiber sliding, etc. in the DE results. Further, the analysis also assumes the formation of ply cracks and delamination under pure Mode-I loading conditions. However, indications of mode-mixity were observed through fractographic observations (Section 6.2.3). Finally, there are possibilities of unavoidable damage creation during unloading cycles in the L-uL results, which also absorb energy.

Chapter 7

7 Results: Compressive damage in non-crimp fabric composites

The behavior of the composites under compression is very critical to their utility as energy absorbing structural applications in automobiles. Even though the majority of the composites in commission are multidirectional laminates, a vast majority of the studies are focused on the failure in unidirectional lamina. This study is hence carried out with a primary focus on understanding the failure process in NCF multidirectional laminates. In-situ edge replication and post-failure optical microscopy are used to understand the initiation and growth of damage in the materials. Finally, an appraisal of the energy dissipated in the observed damage modes is performed.

7.1 Post-failure characterization of damage in unidirectional composites

7.1.1 Failure under axial compression

The unidirectional lamina failed by fiber microbuckling under axial compression. An out-of-plane kink band may clearly be seen in Figure 57. No in-plane component was observed. Inter-tow axial splits were also observed in the failed specimens. However, it is inconclusive at this stage if the inter-tow splitting precedes or succeeds the kink band formation.

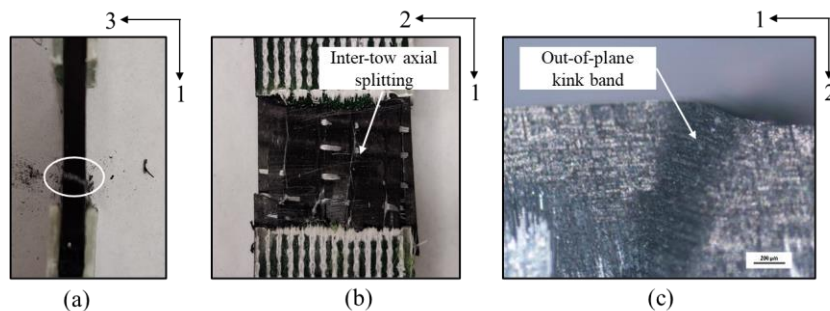


Figure 57: (a-c) Failure by out-of-plane kink band formation in unidirectional lamina under axial compression

7.1.2 Failure under transverse compression

The failure of unidirectional test coupon under transverse compression is characterized by a single crack inclined to the loading direction (Figure 58.a.). The crack is a result of matrix yielding and fiber-matrix debonding. The average fracture angle was measured to be 53° . The crack propagated primarily through the tows (Figure 58.b.). Several secondary cracks branching out of the primary crack were also observed. The growth of the secondary cracks was also found to be primarily through the tows rather than along the tow boundaries. However, no damage was observed away from the immediate vicinity of the crack site (Figure 58.c.) in the test coupon.

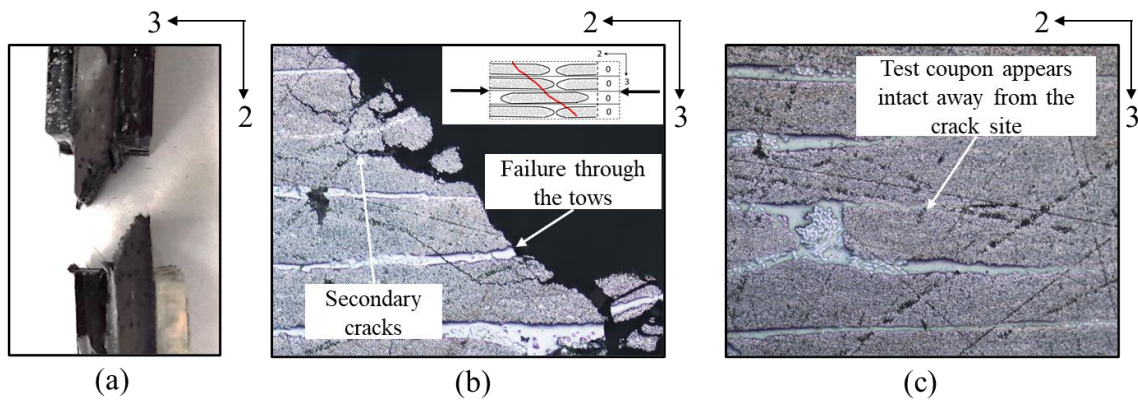


Figure 58: (a) Unidirectional lamina failed under transverse compression (b-c) Edge images of the test coupon failed under transverse compression

7.2 Damage in multidirectional composites

7.2.1 Damage evolution under quasi-static compression

Similar to the tensile loading case, damage evolution under compressive loading was traced using the in-situ ER technique (described in Section 4.3.2). Careful inspection of virgin test coupons using optical microscope showed the presence of resin-rich pockets caused by stitching sites (as was discussed in Section 6.2.1) and no pre-existing damage. The distinguishing damage modes, which characterize the growth of damage in laminates under axial and transverse compressive loads upto failure, are discussed in the upcoming subsections.

7.2.1.1 $[0/\pm 45/90]_s$ and $[90/\pm 45/0]_s$ laminates

The $[0/\pm 45/90]_s$ and $[90/\pm 45/0]_s$ laminates primarily exhibit linear elastic response (Figure 59) through majority of loading steps. First form of damage in $[0/\pm 45/90]_s$ laminate was observed at 0.71% strain as local cracks in the stitching sites (Figure 60.a.). As the coupon was further subjected to a greater load, cracks appeared in more stitching sites through the coupon, which corresponds to a change of slope in step 4 in Figure 59.a.. The load was sufficiently high at this point ($\epsilon_{yy} = 0.98\%$) for some of the cracks in the stitching sites to grow as delamination along the $0/+45$ and ± 45 interfaces (Figure 60.b.). The length of these cracks was in the order of tens of micrometers and hence could not be accurately quantified. The specimen suffered an instantaneous catastrophic failure in the next loading step at 1.17% strain.

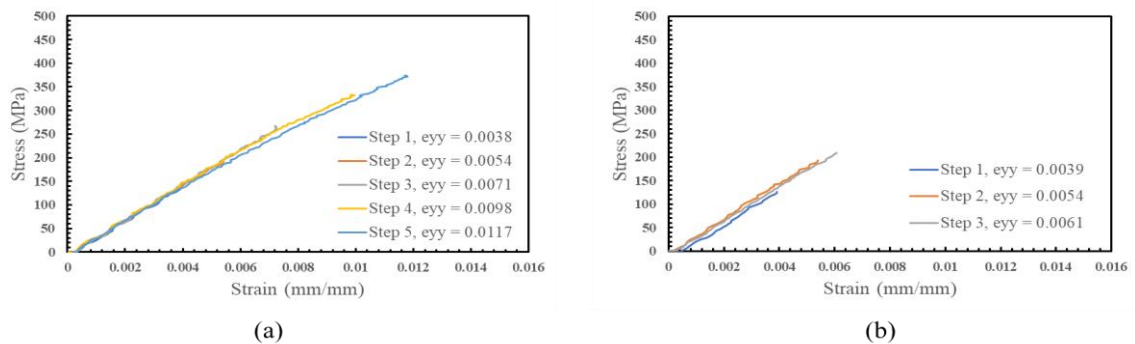


Figure 59: Stress-strain curves from interrupted compression tests for (a) $[0/\pm 45/90]_s$ laminate (b) $[90/\pm 45/0]_s$ laminate

However, the damage initiation was observed at a lower strain in the $[90/\pm 45/0]_s$ laminate. Minor fiber-matrix debonding cracks were observed in the 90° plies (Figure 60.c.) at 0.39% strain. Majority of the cracks were confined to a single tow each in both the 90° plies. These cracks however caused no appreciable reduction in stiffness, as can be deduced from the linear-elastic stress-strain curves (steps 1 and 2 in Figure 59.b.). As the specimen was further strained to 0.54% strain, a single delamination crack, tens of micrometers long, was observed along the ± 45 interface (Figure 60.d.). This crack, however, does not seem to have grown from a cracked stitching site. The laminate failed in the next loading step (step 3 in Figure 59.b.).

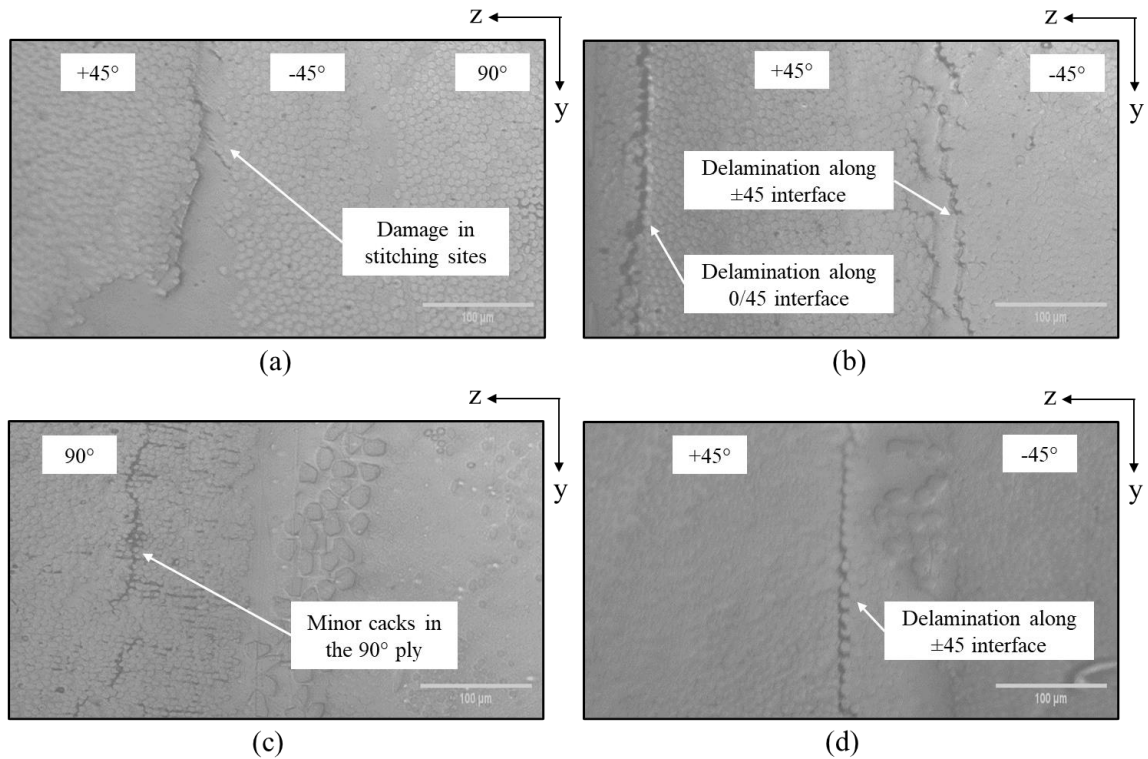


Figure 60: Damage in compression loaded (a) $[0/\pm 45/90]_s$ laminate at 0.71% strain (b) $[0/\pm 45/90]_s$ laminate at 0.98% strain (c) $[90/\pm 45/0]_s$ laminate at 0.39% strain (d) $[90/\pm 45/0]_s$ laminate at 0.54% strain

7.2.1.2 $[\pm 45/0_2]_s$ and $[\pm 45/90_2]_s$ laminates

The stress-strain response of the $[\pm 45/0_2]_s$ laminate under compression is primarily governed by the stiffer 0° plies (Figure 61.a.). The stress-strain response of this laminate under axial compression is linear-elastic through all loading steps. The damage initiates at the interface between glass yarns and matrix at 0.23% (Figure 62.a.) in this case. At higher loads, cracks were observed in multiple such glass yarn and stitching sites (Figure 62.b.). The laminate ultimately failed catastrophically when the load bearing 0° plies failed. On the other hand, in the $[\pm 45/90_2]_s$ laminate, the damage initiated in the stitching sites on ± 45 interface at 0.63% strain (Figure 62.c.), followed by delamination along ± 45 interface at 0.97% strain (Figure 62.d.) and eventual failure.

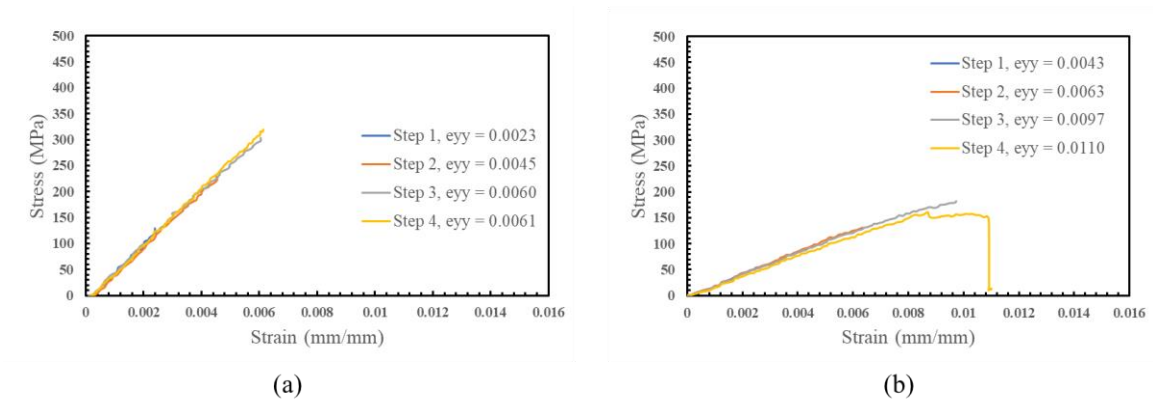


Figure 61: Stress-strain curves from interrupted compression tests for (a) $[\pm 45/0_2]_s$ laminate (b) $[\pm 45/90_2]_s$ laminate

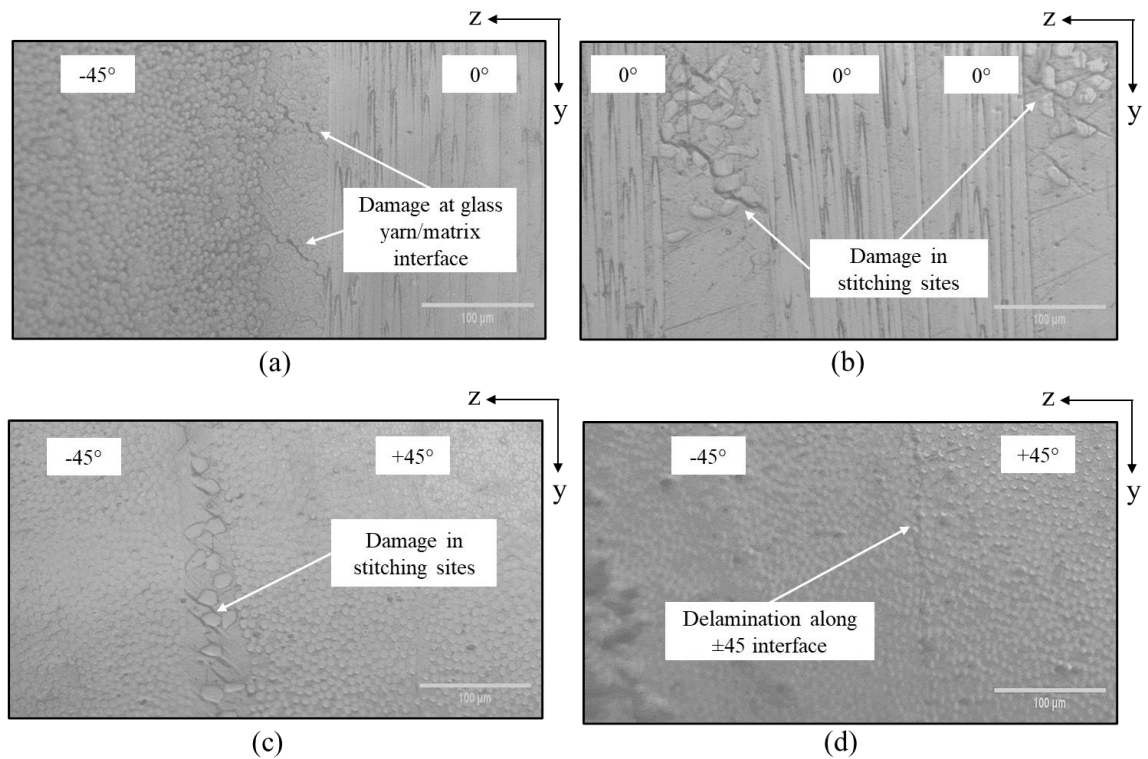


Figure 62: Damage in compression loaded (a) $[\pm 45/0_2]_s$ laminate at 0.23% strain (b) $[\pm 45/0_2]_s$ laminate at 0.60% strain (c) $[\pm 45/90_2]_s$ laminate at 0.63% strain (d) $[\pm 45/90_2]_s$ laminate at 0.97% strain

7.2.2 Post-failure damage characterization

As was discussed in the previous section (Section 7.2.1), although damage initiated in the form of local cracks in the stitching sites, negligible growth of damage was observed until the point of failure in multidirectional composites. The failure in multidirectional laminates is hence instantaneous and entails a high degree of interaction between various failure modes, as is also evidenced by post-failure observations. The same will be discussed in the next sections.

7.2.2.1 $[0/\pm 45/90]_s$ and $[90/\pm 45/0]_s$ laminates

The failure of a $[0/\pm 45/90]_s$ laminate under axial compression is primarily characterized by out-of-plane buckling of 0° plies (aligned along y-direction) and the presence of a single angled crack through the off-axis 45° and 90° plies (Figure 63.a.) oriented at 51° to the loading direction. Similar to the transverse compressive failure in unidirectional composites, the angled crack through the off-axis plies is a combination of failure of the matrix by in-plane shear and fiber-matrix debonding. The key characteristic of the axial compressive failure in this laminate is, however, presence of delamination along $0/+45$ interface (Figure 63.b.). At a sufficiently high load, the local cracks in the stitching sites grow as delamination, which causes the 0° plies to buckle out-of-plane. The loss of the load-bearing 0° plies causes failure of off-axis plies by transverse compression failure mode through the tows (Figure 63.d.) and hence, catastrophic failure of the test coupon. The areas of the test coupon away from the failure site appear intact (Figure 63.e.).

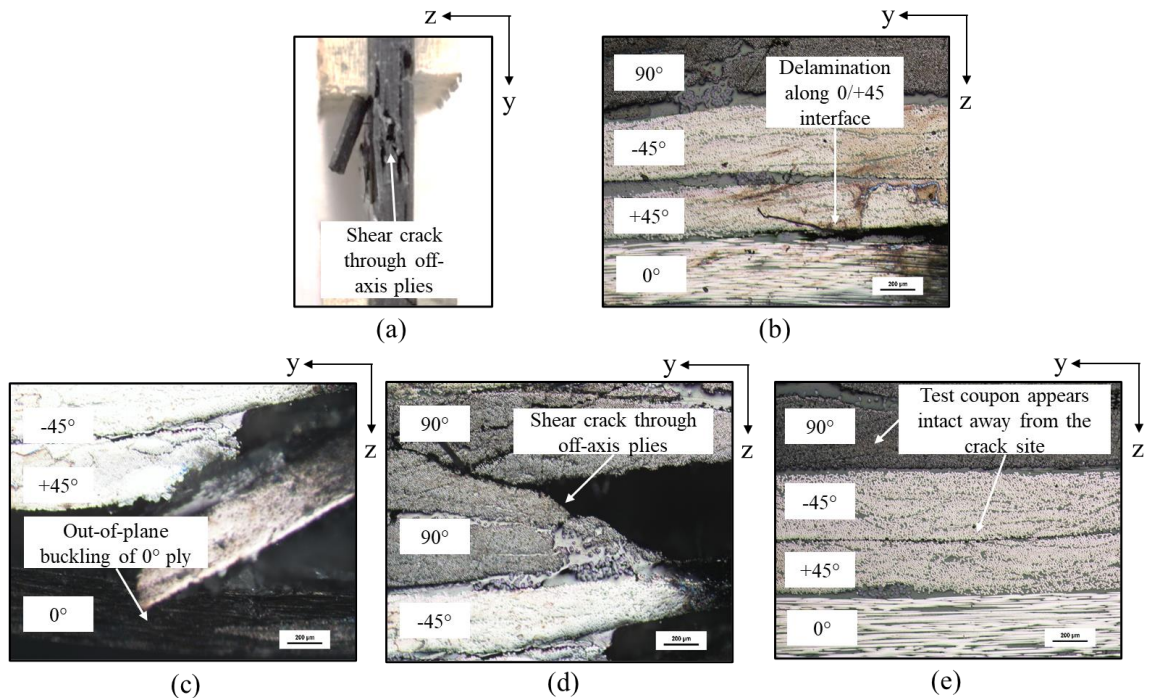


Figure 63: (a) [0/±45/90]_s laminate failed under compression (b-e) Edge images of failed [0/±45/90]_s laminate under compression

A different set of failure modes was observed in the [90/±45/0]_s laminate (Figure 63.a. and Figure 64.a.). Unlike in the [0/±45/90]_s laminate, the delamination seems to have a relatively lesser influence on the failure process. The load bearing plies are centrally located in this loading case. The failure of the laminate is hence driven primarily by the compressive failure of the centrally located 0° plies.

Figure 64.b. and Figure 64.c. reveal a failure of the load bearing plies by shear mode. This failure mode reportedly occurs in composites with very low fiber misalignment at practical volume fractions, when the fibers are closely packed and their relative deformations are in-phase (Agarwal, Broutman, & Chandrashekhara, 2015). This mode is characterized by failure of the plies inclined at approximately 45° to the loading direction (y-direction in Figure 64) and a localized rotation of the fibers (Figure 64.c.). Based on the results from damage evolution tests (Section 7.2.1), it may be said that the rotation of fibers must have occurred at the instant of failure, as no evidence of rotation was found before the failure. The failure of the 0° plies causes the laminate to collapse by buckling,

characterized by a single obliquely oriented shear crack through the off-axis plies, oriented at about 49° to the loading axis, on either side of the central load-bearing plies. A closer inspection also reveals the presence of delamination along 0° / -45° interface extending along y -direction (Figure 64.d.), but is unlikely to have played a major role in the catastrophic failure of the laminate.

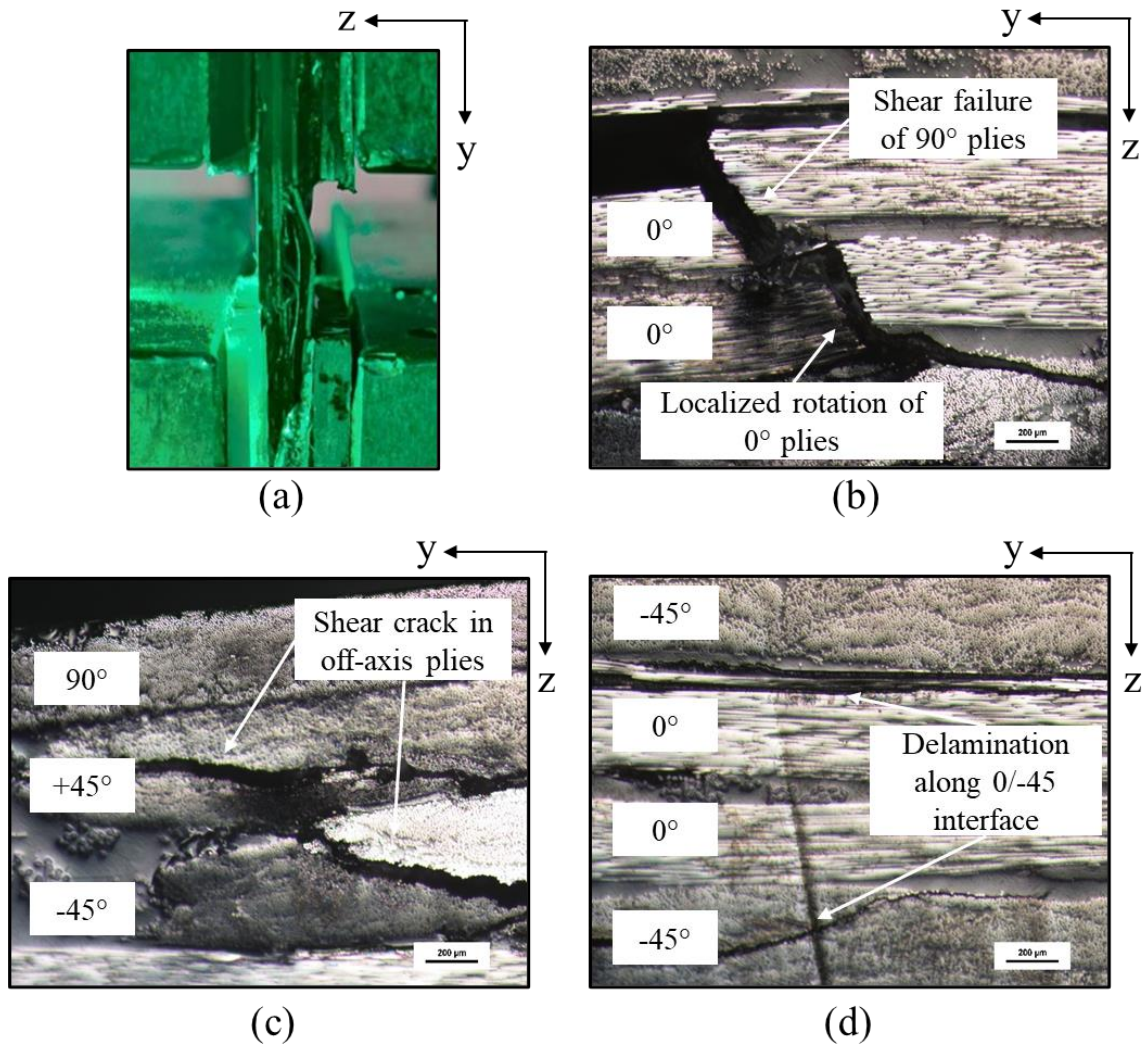


Figure 64: (a) $[90/\pm 45/0]_s$ laminate failed under compression (b-d) Edge images of failed $[90/\pm 45/0]_s$ laminate under compression

7.2.2.2 $[\pm 45/0_2]_s$ and $[\pm 45/90_2]_s$ laminates

Similar to the failure in $[90/\pm 45/0]_s$ laminate (Section 7.2.2.1), the failure of $[\pm 45/0_2]_s$ laminate under compressive loading is governed by the failure of central load-bearing 0° plies (Figure 65.a.). The failure of the 0° plies in this case is, however, an amalgamation of different failure modes (Figure 65.b.-c.). Formation of localized kink band is observed, which is likely a result of local crimp in the fibers, along with the shear failure of the 0° plies, with the failure plane oriented at 33° to the loading axis. Further, localized delaminations were observed between the 0° plies. The delaminations effectively divided the stack of 0° plies into multiple sublamina, which then failed independently by localized rotations and shear. Since no onset of delamination was observed through the damage evolution process (Section 7.2.1), it is not possible to concretely conclude from the available data if the delaminations started to propagate prior to or during fiber failure. Once the 0° plies fail, the outer 45° plies fail at a site in the vicinity of failure site in 0° plies. While the crack may either propagate through the tows or along the boundary of the inner -45° ply, a definite tendency for the crack to propagate along the boundary of outer $+45^\circ$ ply at the ± 45 interface may be observed (Figure 65.d.). This may be attributed to the orthogonality of the ± 45 interface.

On the other hand, all the plies in the $[\pm 45/90_2]_s$ laminate are effectively off-axis plies. The failure hence occurs by the transverse compression mode, i.e., by yielding of the matrix due to in-plane shear and fiber-matrix debonding, as is characterized by the presence of an oblique crack inclined at 58° and parallel to the fibers (Figure 66.a.). The crack passes through the tows in 90° plies (Figure 66.b.). Further, delaminations are observed along the $90/-45$ interface (Figure 66.c.), but no such interply crack was observed along the ± 45 interface, as was generally the case under other loading conditions. The crack through 90° plies, together with the delamination along $0/+45$ interface and the crack passing through the tows in the outer 45° plies (Figure 66.d.) forms one continuous crack in the $[\pm 45/90_2]_s$ laminate under compressive loading.

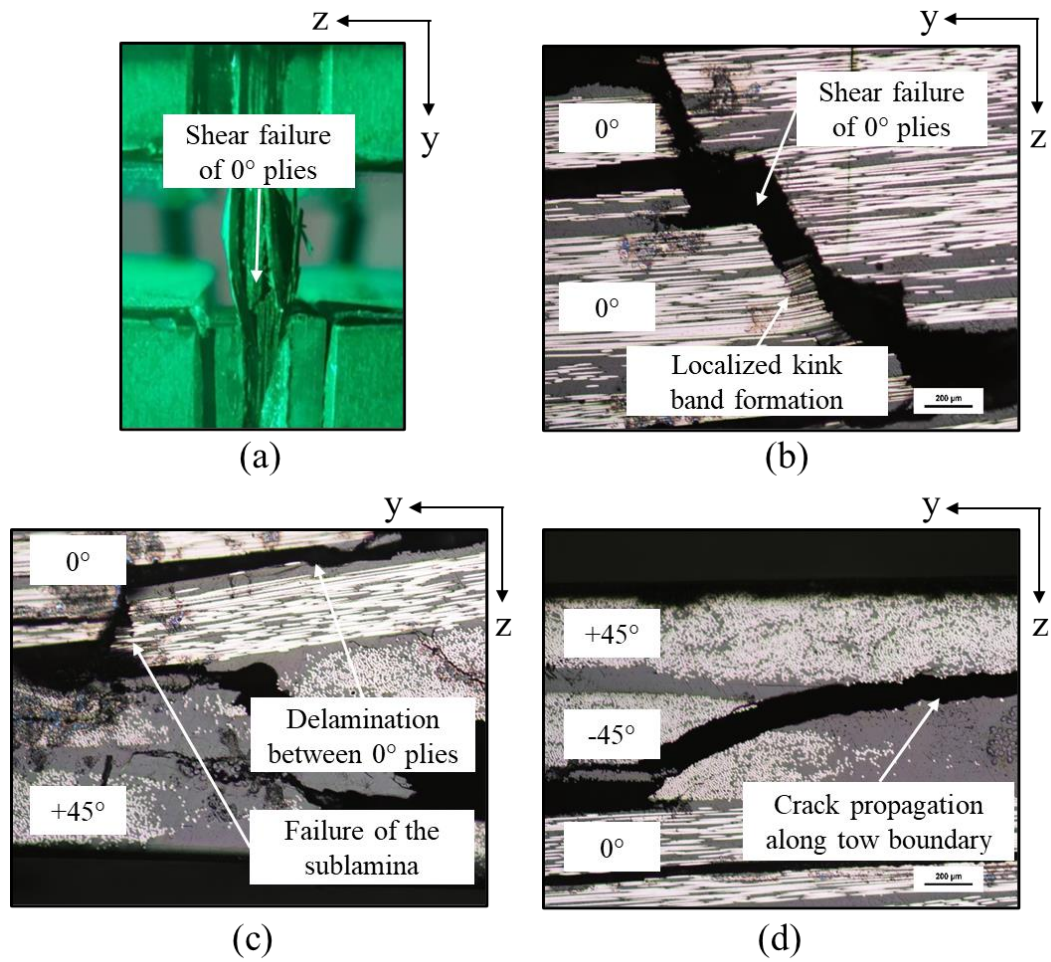


Figure 65: (a) $[\pm 45/0_2]_s$ laminate failed under compression (b-d) Edge images of failed $[\pm 45/0_2]_s$ laminate under compression

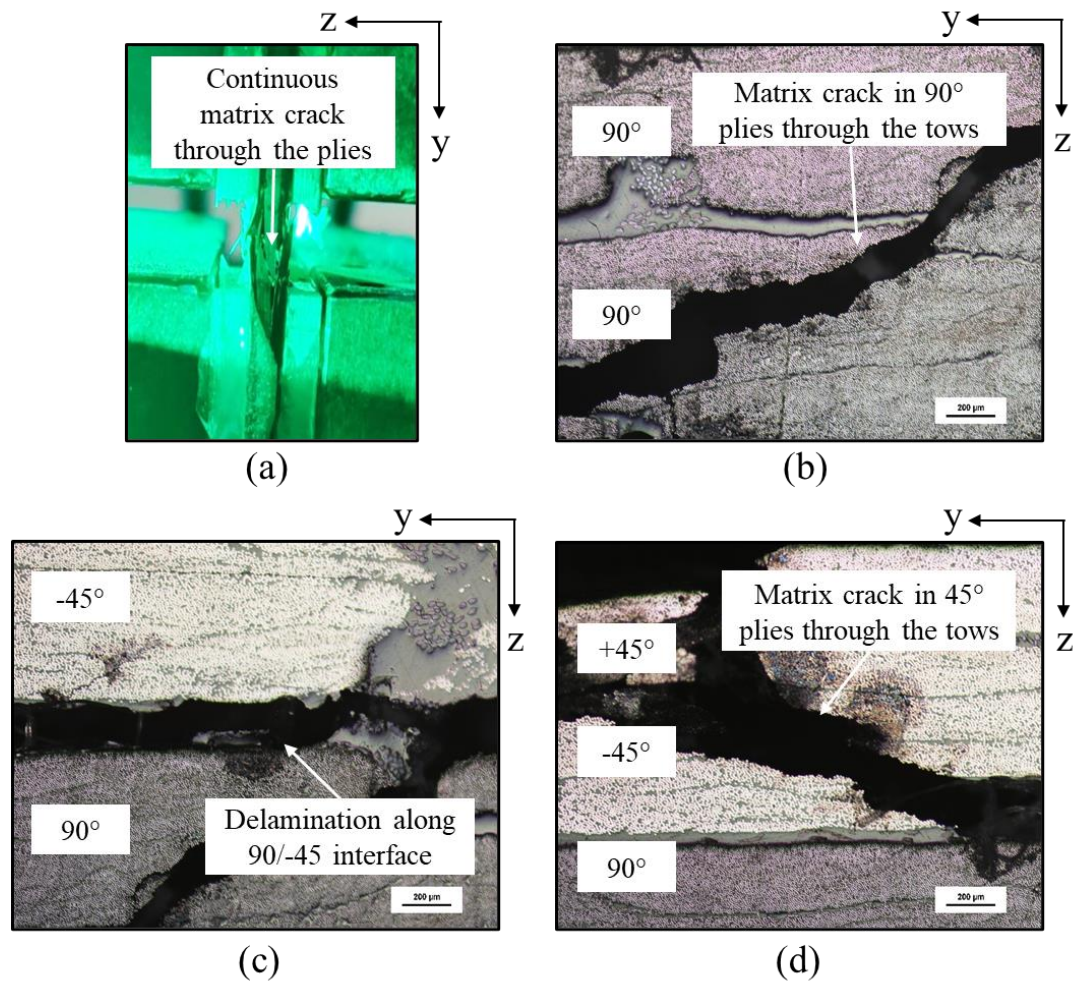


Figure 66: (a) $[\pm 45/90_2]_s$ laminate failed under compression (b-d) Edge images of failed $[\pm 45/90_2]_s$ laminate under compression

7.2.3 Energy dissipation in damage

The damage in multidirectional laminates under quasi-static compression was described in the previous sections. The sites with stitching fibers were found to nucleate the initiation of damage in composites. The damage growth was primarily in the form of delamination and shear crack in the matrix or fibers, and was dependent on the stacking sequence. The observed primary damage modes are listed in Table 3. The growth of damage was instantaneous at an experimentally observable timescale. The laminates were found to be intact away from the damage site, indicating a degree of co-dependence between the damage modes.

Table 3: Primary damage modes in multidirectional laminates under quasi-static compression

Laminate	Primary damage modes
$[0/\pm 45/90]_s$	<ul style="list-style-type: none"> • Delamination along $0/+45$ interface • Single matrix shear crack through 45° and 90° plies
$[90/\pm 45/0]_s$	<ul style="list-style-type: none"> • Fiber shear crack in 90° plies • Delamination along $90/-45$ interface • Two matrix shear crack through 45° and 0° plies
$[\pm 45/0_2]_s$	<ul style="list-style-type: none"> • Fiber shear crack in 0° plies
$[\pm 45/90_2]_s$	<ul style="list-style-type: none"> • Single matrix shear crack through 45° and 0° plies

An energy appraisal of the observed primary damage modes will be performed in this section. The total energy dissipated in the laminate will be tallied against the energies required to create individual damage modes to predict the extent of damage (Details can be found in Appendix 14). For the purpose of this analysis, the presence of secondary damage modes, if any, will be ignored. Also, the energy dissipated in the forms of heat and friction will be ignored. It is assumed that the energy dissipated in the laminates is utilized completely in the creation of primary damage modes for the respective case, as listed in Table 3.

The energy dissipated in the laminate may be calculated using the load-displacement curves (Representative curves shown in Figure 67). The blue part of the curves is the loading part of the curve, as recorded during uninterrupted tests. The black dashed line is the unloading curve, which is assumed to trace back along a path parallel to the initial elastic region of the loading curve. This assumption implies that all the energy dissipated in the damage, responsible for the change of slope of the loading curve after elastic regime, is non-recoverable and that the damage is permanent. The total energy dissipated in damage (Table 4) is the area enclosed by the loading-unloading loop. The calculated energies are listed in Appendix 15.

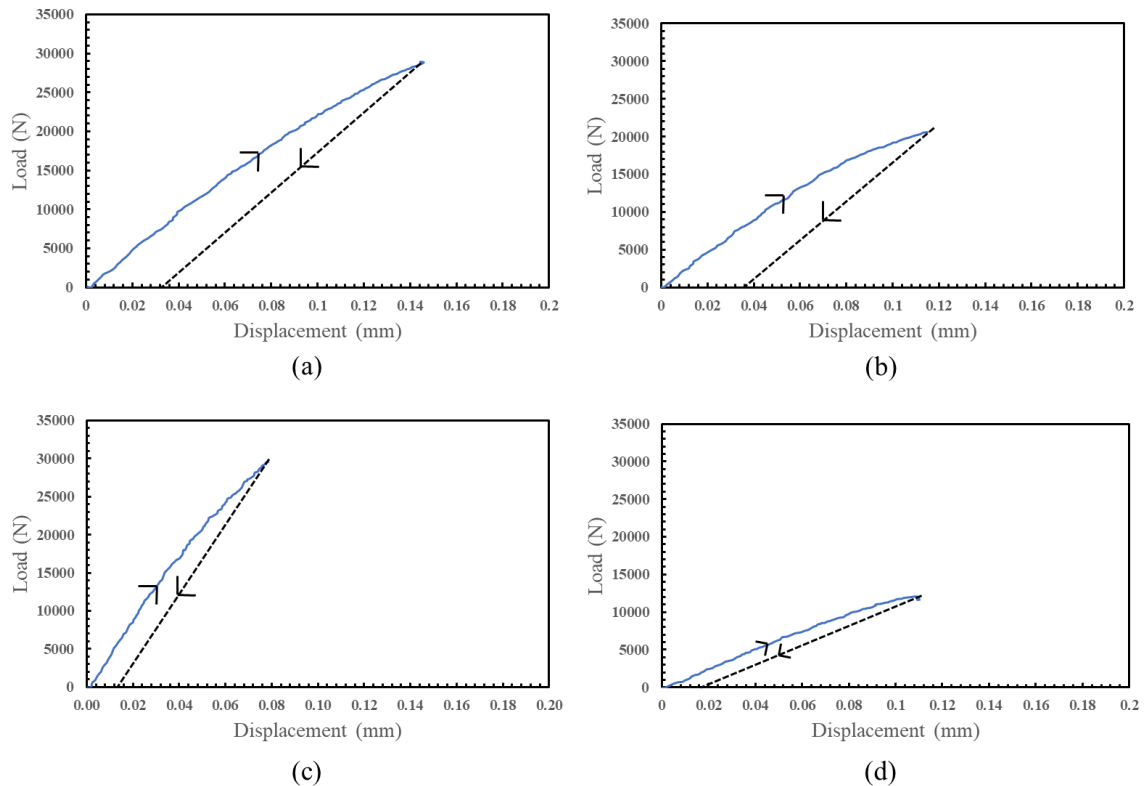


Figure 67: Representative load-displacement curves for (a) $[0/\pm 45/90]_s$ laminate (b) $[90/\pm 45/0]_s$ laminate (c) $[\pm 45/0]_2$ laminate (d) $[\pm 45/90]_2$ laminate

Now, the energy dissipated in the individual damage modes may be determined by multiplying the area of damage and the critical strain energy release rate of that particular damage mode. The critical strain energy release rate is the amount of energy required to create a unit area of damage. The damage modes commonly observed across the two tested laminates are matrix shear crack, fiber shear crack and delamination on the interface between load bearing ply and the adjacent ply. From the list of primary damage modes and fractography results (Table 3 and Section 7.2), it is clear that a definite number of matrix and fiber shear cracks are present in the material. Further, post-failure visual observations confirmed that the cracks span the entire width of the test coupon. Therefore, knowing the geometry of the specimen and the angle of fracture plane, areas of matrix and fiber shear damage may be determined (listed in Table 4). The post-failure visual inspection also confirmed that the delamination cracks span the entire width of the specimen.

The delamination cracks on the 0/45 interface open primarily under Mode-I due to the transverse tensile stresses. As was experimentally observed, the delaminations grow at high loads from damage in the stitching sites (Section 7.2.1). The fracture toughness values for delamination propagation on 0/45 interface under Mode-I loads must hence be used in this analysis. Although the propagation fracture toughness value for delamination along 0/45 interface was not measured, reports suggest that the values for delamination propagation on 0/45 interface are close to those along 0/90 interface. The propagation Mode-I fracture toughness of a cross-ply laminate was experimentally measured to be 645 J/m^2 in this study. The critical strain energy release rate for delamination propagation along 0/45 interface is assumed to be 645 J/m^2 .

The critical strain energy release rates for matrix and fiber shear damage modes, however, were not experimentally measured. They can, however, be estimated from the energy dissipation in $[\pm 45/0_2]_s$ and $[\pm 45/90_2]_s$ laminates. The energies in the $[\pm 45/0_2]_s$ and $[\pm 45/90_2]_s$ laminates were dissipated primarily in fiber shear failure and matrix shear failure respectively. Therefore, the ratio of energy dissipated and the respective crack areas would yield the critical strain energy release rates for fiber and matrix shear damage modes. The critical strain energy release rates for fiber and matrix shear damage modes, hence, are 4243 J/m^2 and 1728 J/m^2 .

Table 4: Total energy dissipated in damage and damage areas in multidirectional laminates under compressive loading

Laminate	Energy dissipated (J)	Matrix shear crack area (mm^2)	Fiber shear crack area (mm^2)
$[0/\pm 45/90]_s$	0.550	57.15	----
$[90/\pm 45/0]_s$	0.443	56.86	20.23
$[\pm 45/0_2]_s$	0.224	----	52.70
$[\pm 45/90_2]_s$	0.121	69.82	----

Now, the knowledge of post-failure observations, fracture toughness, fiber shear and matrix shear damage areas may be used to predict the lengths of delamination in the $[0/\pm 45/90]_s$ and $[90/\pm 45/0]_s$ laminates. In $[0/\pm 45/90]_s$ laminate, the energy is dissipated in a single matrix shear crack and delamination along 0/+45 interface. The product of critical strain energy release rate for matrix shear damage and matrix shear area gives the energy required in 'J' to create the single matrix shear crack. This energy is subtracted from the total dissipated energy to give the energy remaining for creation of delamination crack. The ratio of the available energy and delamination propagation fracture toughness yields the area of delamination. The area of delamination is the product of width and length of delamination. Since the delamination spans the width of the test coupon, the length may be determined by dividing the area of delamination by the width of the specimen. The delamination length in $[0/\pm 45/90]_s$ laminate is predicted to be about 28 mm.

Similarly, the energy is dissipated in two matrix shear cracks, one fiber shear crack and delamination along 90/-45 interface in the $[90/\pm 45/0]_s$ laminate. Therefore, applying the same treatment as before, the energies dissipated in the matrix and fiber shear cracks were first determined. The energies were subtracted from the total dissipated energy, and the remaining energy was used to predict the length of delamination, which was approximately 16 mm in this case.

The predicted lengths are total delamination lengths in the specimen, i.e., a summation of delamination along both the 0/+45 or 90/-45 interfaces. The normalized predicted length is very close to the experimentally measured and normalized post-failure delamination length in the $[0/\pm 45/90]_s$ laminate, but appears to be overpredicted in the $[90/\pm 45/0]_s$ laminate (Figure 68). The overprediction in $[90/\pm 45/0]_s$ laminate is expected to be a reflection of an unaccounted population of secondary fiber/matrix debonds that were observed in damage evolution process (Section 7.2.1.1).

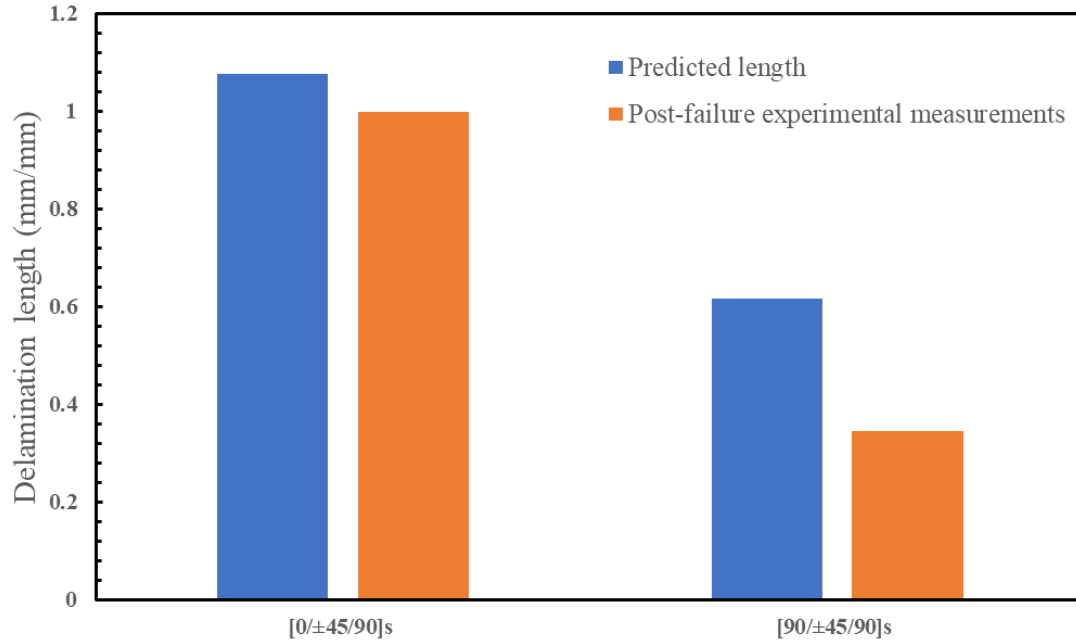


Figure 68: Comparison of predicted delamination lengths and post-failure measurements in $[0/\pm 45/90]_s$ and $[90/\pm 45/90]_s$ laminates under compression

Chapter 8

8 Discussion

The results from the experiments conducted to understand the mechanical response of and damage in NCF composites were presented in the previous chapters. The key results and discussions from the results are presented in the subsequent sections in this chapter. First, the damage in the composites under tension is discussed, followed by a discussion on damage under compression. The key crack propagation features observed in the interlaminar fracture toughness tests are presented, followed by a connection of observed damage and fracture toughness measurements to the energy dissipation characteristics.

8.1 Damage under tensile loads

8.1.1 Unidirectional composites

The unidirectional composites exhibited a linear-elastic response under both, axial and transverse tensile loads, with an unstable catastrophic failure. The fracture planes under both loading conditions were almost flat and oriented perpendicular to the loading direction.

In the case of axial loading, the response of the materials was governed by the properties of the reinforcing fibers. Hence, the specimens failed at about 1.3%, when the failure strain for carbon fibers was reached. Post-failure edge observations revealed that all the failed fibers were present on the same plane, as no fiber breaks were observed away from the failure plane. Observations of the failure surface using SEM indicated a co-operative type of failure of fibers. The failure process likely commenced with the breakage of a single fiber, followed by stress redistribution through the matrix to the neighboring fibers, causing them to break. The failure of a cluster of such fibers on the same plane leads to the catastrophic failure of the specimens under axial tension. The failure under transverse tension was, on the other hand, by fiber/matrix debonding, as indicated by the presence of mostly bare fibers on the failure surface. The crack passed through the fiber tows rather than along the tow boundary.

8.1.2 Multidirectional composites

The first form of damage observed in the multidirectional composite laminates under tension was in the form of cracks in the resin-rich zones created by the stitching threads, which were referred to as ‘stitching sites’ in this dissertation. More specifically, the cracks were present at the stitching fiber-matrix interface. The stitching sites on the midplane, adjacent to off-axis plies, were found to be the most likely to be damaged at lower strains. The cracks in the stitching sites nucleated other damage modes at higher strains, depending on the stacking sequence.

The global stress-strain response and the measured engineering properties were largely identical in the $[0/\pm 45/90]_s$ and $[90/\pm 45/0]_s$ laminates. However, although the laminate exhibited stiffness loss to a similar degree in both the laminates, the damage area was higher in the $[0/\pm 45/90]_s$ laminate. This was largely attributed to the presence of 90/90 delamination cracks at higher strains in the $[0/\pm 45/90]_s$ laminate. Effect of the constraint of the neighboring plies (‘the ply constraining effect’) on the evolution of transverse cracks could also be clearly seen in the tests. In the $[0/\pm 45/90]_s$ laminate, when the 90° plies are sandwiched between other off-axis and 0° plies, a higher crack density was observed as compared to the $[90/\pm 45/0]_s$ laminate, when the transverse plies are on the outer side and unsupported at one end. The transverse cracks had a tendency to cross over into the adjacent 45° plies.

The response of $[\pm 45/0_2]_s$ laminate was dominated by a high concentration of stiff 0° plies in the loading direction. The response was, hence, linear-elastic till the point of failure, i.e. until the point when the failure strain of 0° fibers was reached. No major damage, other than cracks in the stitching sites and minor cracks in the 45° plies, was observed in this case. The stress-strain response of the $[\pm 45/90_2]_s$ laminate was characterized by two changes in slope and two sharp load drops. The changes in slope correspond to the onset of cracking in transverse plies and onset of 90/90 delamination respectively. The two sharp load drops correspond to the cleavage of 45° plies.

Comparison of the $[0/\pm 45/90]_s$ laminate and $[\pm 45/90_2]_s$ laminate yields an understanding of the effect of reduced effective constraining. In the $[\pm 45/90_2]_s$ laminate, four transversely oriented plies are stacked together against the two 90° plies together in the $[0/\pm 45/90]_s$ laminate. This caused cracking of transverse plies in the $[\pm 45/90_2]_s$ laminate at lower stresses.

Furthermore, post-failure edge images and fractographic observations revealed non-coplanar damage, unlike in unidirectional composites. Fiber breaks were found in the 0° plies even away from the failure plane, which may correspond to cracks in the adjacent off-axis plies. The cracks in transverse plies were found to always pass through the tows, whereas the cracks in 45° plies were mostly along the tow boundaries.

8.2 Damage under compressive loads

8.2.1 Unidirectional composites

The materials exhibited a linear-elastic response until failure under axial compression. The axial compression modulus was measured to be almost equal to the axial tensile modulus, and the strength to be almost 60% of the corresponding axial tensile strength. The axial compression failure was characterized by an out-of-plane kink band and inter-tow splits. It was, however, inconclusive if the splits preceded the kink band formation.

The failure under transverse compression, on the other hand, was characterized by a single crack passing through the fiber tows, aligned at 53° to the loading direction. The failure, in this case, is a combination of matrix yielding and fiber/matrix debonding, which manifests as a prominent plastic zone in the global stress-strain curves.

8.2.2 Multidirectional composites

In-situ damage monitoring revealed that, similar to the tensile loading cases, the initiation of damage was in the form of cracks in the stitching sites. These cracks grew to form delamination or matrix cracks at higher strain, leading to the catastrophic unstable failure. The global stress-strain behavior of the multidirectional composites was very strongly dependent on the stacking sequence of the laminates. Unlike under tension, the effect was evident in the measured engineering properties as well, especially in the $[0/\pm 45/90]_s$ and $[90/\pm 45/0]_s$ laminates.

The $[0/\pm 45/90]_s$ laminate, where the compliant off-axis plies were sandwiched by the stiff 0° plies, was stiffer and stronger than the $[90/\pm 45/0]_s$ laminate. Post-failure edge observations revealed two primary damage modes: Delamination along $0/+45$ interface and a single angled matrix shear crack passing through all the off-axis plies. These observations are suggestive of a failure due to structural instability because of out-of-plane buckling of the 0° plies, after cracks in the stitching sites grew as delamination along $+45$ interface. The response of the $[90/\pm 45/0]_s$ laminate, on the other hand, was dictated by the central load-bearing plies. The laminate failed as soon as the central plies failed in fiber shear mode. The fiber shear failure mode has been reported in the materials with minimum fiber misalignments and is a confirmation that the maximum strength of the load-bearing plies is approached. On comparison, it may be inferred that the presence of 0° plies on the outside constrains the damage in the compliant off-axis plies in $[0/\pm 45/90]_s$ laminate, delaying the catastrophic failure.

The failure of the $[\pm 45/0_2]_s$ laminate was, as expected, dictated by the failure of the central 0° plies. Although the failure was primarily by fiber shear, local kink band and localized delamination cracks were observed near the failure site. The delamination effectively divided the laminate into sublaminae, which then may have failed independently. The failure of the $[\pm 45/90_2]_s$ laminate is effectively in the form of a single oblique crack, resulting from a combination of matrix yielding and fiber/matrix debonding. Minor delaminations were observed along the $0/+45$ interface along with the matrix shear crack.

8.3 Interlaminar fracture toughness tests

8.3.1 Unidirectional composites

The crack propagated on the midplane under both, Mode-I and Mode-II loads in unidirectional composites very close to and on the fiber/matrix interface respectively. While a stick-slip behavior (characterized by alternating periods of unstable progression of crack and crack arrestation) was observed under Mode-I loads, stable crack propagation was achieved under Mode-II loads. The crack arrestation sites corresponded with the presence of stitching sites. It is interesting to note that although the stitching sites arrested the cracks in fracture toughness tests, the cracks initiated in these sites under uniaxial tensile and compressive loads. The stitching pattern, hence, must affect the damage in the form of cracks in NCF composites.

The Mode-II fracture toughness (G_{IIc}) for initiation and propagation in unidirectional composites was measured to be about thrice the Mode-I fracture toughness (G_{Ic}). This was attributed to the presence of hackles, which was observed as a key feature on the Mode-II delamination failure surface using SEM. The hackles lead to a higher effective surface area, which increases the G_{IIc} . The hackles, along with the resistance offered by stitching sites to the crack propagation, caused the G_{IIc} to be three times higher than the G_{Ic} .

8.3.2 Cross-ply composites

In the case of cross-ply laminates ($[0_3/90]_s$), the crack instantly migrated from the midplane to the 0//90 interface and propagated further along the 0//90 interface under both, Mode-I and Mode-II loads. A stick-slip type of crack propagation behavior was observed under both loading conditions. However, different from unidirectional composites, the transverse tows on the crack propagation path arrested the crack growth in the case. The tows forced the crack to follow an undulating path, causing the G_{Ic} for cross-ply laminates to be 45% higher than the unidirectional composites. However, as the primary resistance to the crack propagation was provided by transverse tows under both loading conditions, the G_{IIc} for crack propagation was only about 40% higher than the G_{Ic} .

8.4 Energy dissipation in formation of damage

8.4.1 Tensile loads

The energy dissipated in damage and the corresponding drops in laminate stiffness under tensile loads were compared using two strategies in this study. In the first case, the dissipated energy was calculated as a sum of product of the areas of different damage modes, as were determined in the damage evolution tests, and the critical strain energy release rates associated with those. In the second strategy, the energy was determined by multiplying the area enclosed by the loading-unloading curves to the volume of the specimen considered for strain measurement. The laminate stiffness was measured from the stress-strain curves in the tests relevant to the respective strategies. There was generally a good agreement between the results from both strategies. However, some minor differences were seen in the dissipated energy values for some laminates, which was attributed to the statistical nature of the events involved in the failure process, such as damage in the stitching sites, fiber breakage, etc.

8.4.2 Compression loads

The primary failure modes in the $[\pm 45/0_2]_s$ and $[\pm 45/90_2]_s$ laminate were fiber shear mode and matrix shear modes respectively. The energies dissipated in the creation of these modes, which were calculated using the stress-strain curves, were divided by the respective damage areas to obtain the critical strain energy release rates associated with the fiber shear and matrix shear failure modes. The primary damage modes observed in the $[0/\pm 45/90]_s$ and $[0/\pm 45/90]_s$ laminates were delamination along 0/45 interface and a matrix shear crack through the off-axis plies. Failure of central load-bearing plies by fiber shear mode was observed in the $[90/\pm 45/0]_s$ laminate. Using the estimated toughness values for fiber and matrix shear modes and the critical strain energy release rate associated with delamination growth, the extents of delamination were predicted. A good agreement was observed in the $[0/\pm 45/90]_s$ laminate, while the value was overpredicted in the case of $[90/\pm 45/0]_s$ laminate. The overprediction was attributed to the fact that the presence of secondary modes was ignored in this analysis.

Chapter 9

9 Conclusions and recommendations of future works

The key findings and novel contributions from this study are summarized in subsequent sections in this chapter, The chapter ends with recommendations on possible avenues for future work to further the knowledge in the field of damage in NCF composites.

9.1 Noteworthy conclusions

The key takeaways from this study can be summarized as follows:

- The tensile response of the unidirectional and multidirectional laminates in majority of the investigated cases was primarily linear-elastic, as it was governed by the presence of load bearing fibers aligned in the loading direction. The stacking sequence and the stitching sites were found to have a negligible influence on the measured tensile properties such as tensile strength, elastic modulus, strain-to-failure, etc.
- Stacking sequence had a pronounced impact on the measured compression properties. The impact was most clearly observed in the case of $[0/\pm 45/90]_s$ and $[90/\pm 45/0]_s$ laminates. The $[0/\pm 45/90]_s$ laminate was significantly stiffer than the $[90/\pm 45/0]_s$ laminate, as in the case of $[0/\pm 45/90]_s$ laminate, the stiff 0° fibers constrain the damage in the sandwiched off-axis plies and delay the catastrophic failure.
- The axial compression modulus was measured to be almost to the axial tensile modulus, and the axial compression strength to be about 60% of the axial tensile strength in unidirectional laminae. These trends are slightly different from the generally reported trends in open literature so far.

- Stick-slip crack propagation behavior was observed in unidirectional composites under Mode-I loads, with the stitching sites offering the resistance to crack propagation. A stable crack growth was observed under Mode-II loads. The Mode-II fracture toughness was measured to be almost three times that of the Mode-I fracture toughness. The hackles, that were observed on the fracture surface, were the primary contributors to higher Mode-II fracture toughness.
- On the other hand, stick-slip behavior was observed in cross-ply laminates under both, Mode-I and Mode-II loads. The transversely oriented carbon fiber tows resisted the propagation of crack in cross-ply laminates, forcing the crack to follow an undulating path. The Mode-II fracture toughness was only slightly higher in this case than the corresponding Mode-I fracture toughness.
- In-situ damage monitoring of tests under tensile and compression yielded a clear understanding of the initiation and evolution of distinct damage mechanisms in the materials. Initiation of damage was in the form of cracks in the stitching sites, at the stitching thread-matrix interface. The damage in the stitching sites act as nucleating sites for other forms of damage such as ply cracks and delamination.
- Under tensile loads, the cracks in the stitching sites are generally succeeded by cracks in the transverse plies. The cracks in the transverse plies have a tendency to cross-over into the adjacent 45° plies. The ± 45 interface was most susceptible to ply crack induced delamination. The final failure of the specimens was controlled by the failure of 0° plies. The rate of multiplication of ply cracks is strongly influenced by the constraint of the neighboring plies.
- The failure of the multidirectional laminates was instantaneous under compressive loads. Optical microscopic observations of the edge revealed different damage mechanisms, primarily in the form of fiber and matrix shear failures and delamination on the interface between 0° plies and the adjacent off-axis ply, contributing to the failure.

- An appraisal of energy contributions from the individual damage modes revealed that delamination cracks generally absorbed the most energy of all the damage modes in the laminates under various mechanical loading conditions.

9.2 Key novelties

- This study provides an in-depth in-plane quasi-static characterization and delamination characterization of the novel UD-NCF carbon fiber reinforced epoxy composites, further correlating the extent of damage to stress-strain behavior and material microstructure.
- This is one of the few available experimental studies in the literature that employs a combination of in-situ damage monitoring and microscopy techniques to provide a complete picture of damage in multidirectional NCF composites under tensile loads. Most prominently, this study clearly outlines the role of stitching sites in the damage evolution process.
- The focus in this study on understanding the damage in multidirectional NCF laminates under compressive loads, and its connection to the energy dissipation, is a novel contribution to the literature.

9.3 Recommendations for future work

- The engineering properties measured for UD material and the experimental data from the DCB tests can be used to calibrate material constitutive models.
- It was conclusively concluded in this study that the initiation of damage in NCF composites is in the form of cracks in the stitching sites at the interface between stitching threads and the matrix, and the further damage modes are nucleated by those. Further, it is also possible that the cracks in the stitching sites themselves make significant contribute to the energy absorption. Therefore, the characteristics of stitching sites can be tuned to alter the extents of damage, and by extension the energy absorption, in NCF composites. A deeper investigation in the stitching fiber/matrix adhesion is, hence, recommended.

- It was observed in the interlaminar fracture toughness tests that the stitching sites arrest the progression of cracks, which was termed as the ‘stick-slip’ behavior. The influence of different stitching patterns on the stick-slip behavior must, hence, be further investigated.
- As was pointed out in this study, although NCF composites have grown in prominence as a competition to unidirectional prepreg and woven composites, the key criteria for their adoption for structural applications in automotive is their crashworthiness. It would be of benefit to use the damage evolution and energy absorption data under tension as a baseline and compare their energy absorption to the prepreg and woven composites architectures of the same material system.
- The in-situ damage monitoring during the compression test of $[0/\pm 45/90]_s$ laminate revealed that the presence of stiff outer plies in a laminate contain and delay failure. However, once the delamination crack between the 0/45 interface grew, the specimen failed instantaneously. Therefore, a laminate containing central load-bearing plies may be considered, like $[0/\pm 45/0]_s$ stacking sequence, for better structural stability under compression.
- The energy dissipation calculations performed in this study using the stress-strain curves are only applicable in a uniaxial loading case. It is, hence, recommended that strategies for energy dissipation under multi-axial loading cases be further investigated and developed.

9.4 Final word

The correlation of the mechanical response of the NCF composites to damage and microstructure provides valuable information that is expected to aid in the better design of composite materials for structural applications in automobiles.

References

- (2020). Retrieved from Global Market Insights: <https://www.gminsights.com/industry-analysis/automotive-composites-market>
- Adams, D. (2009, February 02). *A comparison of shear test methods*. Retrieved from CompositesWorld: <https://www.compositesworld.com/articles/a-comparison-of-shear-test-methods>
- Agarwal, B. D., Broutman, L. J., & Chandrashekhara, K. (2015). *Analysis and Performance of Fiber Composites* (Third ed.). New Delhi, India: John Wiley & Sons.
- Alfred Franklin, V., & Christopher, T. (2013). Fracture Energy Estimation of DCB Specimens Made of Glass/Epoxy: An Experimental Study. *Advances in Materials Science and Engineering*, 1-7. doi:<http://dx.doi.org/10.1155/2013/412601>
- Allix, O., Feld, N., Baranger, E., Guimard, J.-M., & Ha-Minh, C. (2014). The compressive behaviour of composites including fiber kinking: modelling across the scales. *Meccanica*, 49, 2571-2586.
- Arai, M., Noro, Y., Sugimoto, K.-i., & Endo, M. (2008). Mode I and Mode II interlaminar fracture toughness of CFRP laminates toughened by carbon nanofiber interlayer. *Composites Science and Technology*, 68, 516-525. doi:[doi:10.1016/j.compscitech.2007.06.007](https://doi.org/10.1016/j.compscitech.2007.06.007)
- Argon, A. S. (1972). Fracture of composites. *Treatise on material science and technology*, 1, 79-114.
- Asp, L. E., Edgren, F., & Sjögren, A. (2004). Effects of Stitch Pattern on the Mechanical Properties of Non-Crimp Fabric Composites.

- ASTMD3039. (2017). Standard Test Method for Tensile Properties of Polymer Matrix Composite Materials. *Annual Book of ASTM*, 1-13. doi:10.1520/D3039_D3039M-17
- ASTMD3410. (2016). Standard Test Method for Compressive Properties of Polymer Matrix Composite Materials with Unsupported Gage Section by Shear Loading. *Annual Book of ASTM*, 1-16. doi:10.1520/D3410_D3410M-16
- ASTMD5528. (2013). Mode I Interlaminar Fracture Toughness of Unidirectional Fiber-Reinforced Polymer Matrix Composites. *Annual Book of ASTM*, 1-13. doi:10.1520/D5528-13
- ASTMD7078. (2012). Standard Test Method for Shear Properties of Composite Materials by V-Notched Rail Shear Method. *Annual Book of ASTM*, 1-15. doi:10.1520/D7078_D7078M-12
- ASTMD7905. (2019). Determination of the Mode II Interlaminar Fracture Toughness of Unidirectional Fiber-Reinforced Polymer Matrix Composites. *Annual Book of ASTM*, 1-18. doi:10.1520/D7905_D7905M-19E01
- Backhouse, R. A. (1995). *A comparative evaluation of non-crimp fabric composites with different stitching styles against unidirectional prepreg tape composites*. BAE-CMC internal report.
- Basu, S., Waas, A. M., & Ambur, D. R. (2006). Compressive failure of fiber composites under multi-axial loading. *Journal of the Mechanics and Physics of Solids*, 54, 611-634.
- Bibo, G. A., Hogg, P. J., & Kemp, M. (1997). Mechanical Characterisation of glass- and carbon-fibre-reinforced composites made with Non-Crimp Fabrics. *Composite Science and Technology*, 57, 1221-1241.
- Bibo, G., & Hogg, P. (1998). Influence of Reinforcement Architecture on Damage Mechanisms and Residual Strength of Glass-fiber/epoxy Composite Systems. *Composites Science and Technology*, 58, 803-813.

- Black, S. (2008, September 9). *Structural health monitoring: Composites get smart*. Retrieved from CompositesWorld: <https://www.compositesworld.com/articles/structural-health-monitoring-composites-get-smart>
- Bogdanovich, A. E., Karahan, M., Lomov, S. V., & Verpoest, I. (2013). Quasi-static tensile behavior and damage of carbon/epoxy composite reinforced with 3D non-crimp orthogonal woven fabric. *Mechanics of Materials*, *62*, 14-31.
- Boniface, L., Smith, P. A., Bader, M. G., & Rezaifard, A. H. (1997). Transverse Ply Cracking in Cross-Ply CFRP Laminates—Initiation or Propagation Controlled? *Journal of Composite Materials*, *31*(11), 1080-1112. doi:<https://doi.org/10.1177/002199839703101102>
- Bradley, W. (1989). *Relationship of matrix toughness to interlaminar Interlaminar Fracture Toughness* (Vol. 6). (K. Friedrich, Ed.) Elsevier. doi:<https://doi.org/10.1016/B978-0-444-87286-9.50009-7>
- Bradley, W. (1991). Understanding the Translation of Neat Resin Toughness into Delamination Toughness in Composites. *Key Engineering Materials*, *37*, 161-198. doi:<https://doi.org/10.4028/www.scientific.net/KEM.37.161>
- Brambleby, R., Louca, L., & Mouring, S. (2017). Influence of loading rate on the mode II fracture toughness of vinyl ester GRP. *Composites: Part A*, *93*, 153-162. doi:<http://dx.doi.org/10.1016/j.compositesa.2016.11.023>
- Brosius, D. (2015). *Thermosets vs. thermoplastics: Is the battle over?* Retrieved from CompositesWorld: <https://www.compositesworld.com/articles/thermosets-vs-thermoplastics-is-the-battle-over>
- Bru, T., Hellström, P., Gutkin, R., Ramantani, D., & Peterson, G. (2016). Characterisation of the mechanical and fracture properties of a uni-weave carbon fibre/epoxy non-crimp fabric composite. *Data in Brief*, *6*, 680-695. doi:<http://dx.doi.org/10.1016/j.dib.2016.01.010>

- Bruce, T. (2011). Mechanistic Mixed-Mode Failure Criterion for Continuous Fiber-Polymer Composites. *Electronic Thesis and Dissertation Repository*. London, Ontario, Canada: University of Western Ontario. Retrieved from <https://ir.lib.uwo.ca/etd/349>
- Budiansky, B., Fleck, N. A., & Amazigo, J. C. (1998). On kink-band propagation in fiber composites. *Journal of the Mechanics and Physics of Solids*, 46(9), 1637-1653.
- Cai, J., Qiu, L., Yuan, S., Shi, L., Liu, P., & Liang, D. (2012). Structural Health Monitoring for Composite Materials. *Open Access Chapter*, 37-60. InTechOpen.
- Carbon Neutrality Goals by Country*. (2021, June 17). Retrieved from Motivepower: <https://www.motive-power.com/npuc-resource/carbon-neutral-goals-by-country/>
- Carlsson, L., & Pipes, R. (1987). Chapter 6: Lamina compressive response. *Experimental characterization of advanced composite materials*, 67-81.
- Carraro, P. A., Maragoni, L., & Quaresimin, M. (2015). Influence of manufacturing induced defects on damage initiation and propagation in carbon/epoxy NCF laminates. *Advanced Manufacturing: Polymer & Composites Science*, 1(1), 44-53. doi:<https://doi.org/10.1179/2055035914Y.0000000004>
- Cox, B. N., & Dadkhah, M. S. (1995). The Macroscopic Elasticity of 3D Woven Composites. *Journal of Composite Materials*, 29(6), 785-819.
- Crossan, M. (2018). Mechanical Characterization and Shear Test Comparison for Continuous-Fiber Polymer Composites. *MESc Dissertation*. London, Ontario, Canada: Western University.
- Davidson, B. (1990). An Analytical Investigation of Delamination Front Curvature in Double Cantilever Beam Specimens. *Journal of Composite Materials*, 24, 1124-1137.
- de Verdier, M., Skordos, A., May, M., & Walton, A. (2012). Influence of loading rate on the delamination response of untufted and tufted carbon epoxy non crimp

fabric composites: Mode I. *Engineering Fracture Mechanics*, 96, 11-25.
doi:<http://dx.doi.org/10.1016/j.engfracmech.2012.05.015>

- Dexter, H. B., & Hasko, G. H. (1996). Mechanical properties and damage tolerance of multiaxial warp-knit composites. *Composite Science and Technology*, 56, 367-380.
- Edgren, F., Asp, L. E., & Joffe, R. (2006). Failure of NCF composites subjected to combined compression and shear loading. *Composites Science and Technology*, 66, 2865-2877.
- Edgren, F., Mattsson, D., Asp, L. E., & Varna, J. (2004). Formation of damage and its effects on non-crimp fabric reinforced composites loaded in tension. *Composites Science and Technology*, 64, 675-692. doi:10.1016/S0266-3538(03)00292-6
- Ewins, P. D., & Potter, R. T. (1980). Some observations on the nature of fiber reinforced plastics and the implications for structural design. *Philosophical Transactions of Royal Society of London A*, 294, 507-517.
- Ferrarese, A. (2020). Dynamic delamination testing of a composite material. *Master thesis*. Torino, Italy: Politecnico di Torino.
- Gamstedt, E. K., & Sjögren, B. A. (1999). Micromechanisms in tension-compression fatigue of composite laminates containing transverse plies. *Composites Science and Technology*, 59, 167-178.
- Gardiner, G. (2015, July 31). *Structural health monitoring: The toolbox*. Retrieved from CompositesWorld: <https://www.compositesworld.com/articles/structural-health-monitoring-the-toolbox>
- Godbehere, A. P., Mills, A. R., & Irving, P. (1994). Non-crimp fabrics versus prepreg CFRP composites – A comparison of mechanical performance. *6th International Conference on Fibre Reinforced Composites*. Newcastle.

- Gong, X., Hurez, A., & Verchery, G. (2010). On the determination of delamination toughness by using multidirectional DCB specimens. *Polymer Testing*, 29, 658-666. doi:doi:10.1016/j.polymertesting.2010.04.007
- González, C., & Llorca, J. (2007). Mechanical behavior of unidirectional fiber-reinforced polymers under transverse compression: Microscopic mechanisms and modeling. *Composites Science and Technology*, 67, 2795-2806.
- Greenhalgh, E. (2009). Delamination-dominated failure in polymer composites. In E. S. Greenhalgh, *Failure analysis and fractography of polymer composites* (pp. 178-223). Cambridge: Woodhead Publishing Limited.
- Greenhalgh, E. S. (2009). *Failure analysis and fractography of polymer composites*. Cambridge: Woodhead Publishing.
- Greenhalgh, E. S., Rogers, C., & Robinson, P. (2009). Fractographic observations on delamination growth and the subsequent migration through the laminate. *Composites Science and Technology*, 69, 2345-2351. doi:doi:10.1016/j.compscitech.2009.01.034
- Guillamet, G., Turon, A., Costa, J., & Renart, J. (2014). Damage evolution in thin and thick-ply regions of NCF thin-ply laminates under off-axis uniaxial loading. *ECCM-16th European Conference on Composite Materials*, (pp. 1-5). Seville.
- Gutkin, R. (2013). Modelling Compressive Damage in CFRP: Combining Friction with Damage. *The 19th International Conference on Composite Materials*, (pp. 1-8). Montreal.
- Gutkin, R., Pinho, S. T., Robinson, P., & Curtis, P. T. (2010). Micro-mechanical modelling of shear-driven fiber compressive failure and of fiber kinking for failure envelope generation in CFRP laminates. *Composites Science and Technology*, 70, 1214-1222.
- Gutkin, R., Pinho, S. T., Robinson, P., & Curtis, P. T. (2010). On the transition from shear-driven fibre compressive failure to fibre kinking in notched CFRP laminates

under longitudinal compression. *Composites Science and Technology*, 70, 1223-1231.

Hassani, S., Mousavi, M., & Gandomi, A. H. (2022). Structural Health Monitoring in Composite Structures: A Comprehensive Review. *Sensors*, 22(153), 1-45. doi: <https://doi.org/10.3390/s22010153>

Hu, Y., Kar, N. K., & Nutt, S. R. (2015). Transverse Compression Failure of Unidirectional Composites. *Polymer Composites*, 756-766.

Hull, D., & Clyne, T. W. (1996). *An Introduction to Composite Materials* (2 ed.). Cambridge University Press.

Hult, J. H., & McClintock, F. A. (1956). Elastic-plastic stress and strain distribution around sharp notches under repeated shear. *IXth International Congress of Applied Mechanics*, 8. Brussels.

Inglis, C. E. (1913, March 14). Stresses in a plate due to the presence of cracks and sharp corners. *Spring Meetings of the fifty-fourth Session of the Naval Architects*, 219-241.

Isakov, M., May, M., Paul, H., & Nishi, M. (2019). Fracture toughness measurement without force data – Application to high rate DCB on CFRP. *Composites: Part A*, 119, 176-187. doi:<https://doi.org/10.1016/j.compositesa.2019.01.030>

Joffe, R., Mattsson, D., Modniks, J., & Varna, J. (2005). Compressive failure analysis of non-crimp fabric composites with large out-of-plane misalignment of fiber bundles. *Composites: Part A*, 36, 1030-1046.

Kahla, H. B. (2019, June). Micro-cracking and delaminations of composite laminates under tensile quasi-static and cyclic loading. *PhD Dissertation*. Luleå, Sweden: Luleå University of Technology.

- Leopold, C., Schütt, M., Liebig, W. V., Philipkowski, T., Kürten, J., Schulte, K., & Fiedler, B. (2017). Compression Fracture of CFRP Laminates Containing Stress Intensifications. *Materials*, *10*, 1039. doi:10.3390/ma10091039
- (n.d.). *Lightweight, heavy impact*. McKinsey&Company.
- Liu, S., & Nairn, J. A. (1992). The formation and propagation of matrix microcracks in cross-ply laminates during static loading. *Journal of Reinforced Plastics and Composites*, *11*(2), 158-178. doi:https://doi.org/10.1177/073168449201100204
- Llobet, J., Maimí, P., Essa, Y., & Martín de la Escalera, F. (2019). Progressive matrix cracking in carbon/epoxy cross-ply laminates under static and fatigue loading. *International Journal of Fatigue*, *119*, 330-337. doi:10.1016/j.ijfatigue.2018.10.008
- Lowe, A. (1996). Transverse compressive testing of T300/914. *Journal of Materials Science*, *31*, 1005-1011.
- Mattson, D. (2005). Mechanical Performance of NCF Composites. *PhD Dissertation*. Luleå, Sweden: Luleå University of Technology.
- Mattsson, D., Joffe, R., & Varna, J. (2008). Damage in NCF composites under tension: Effect of layer stacking sequence. *Engineering Fracture Mechanics*, *75*, 2666-2682. doi:10.1016/j.engfracmech.2007.03.014
- McCartney, L. N. (1998). Predicting transverse crack formation in cross-ply laminates. *Composites Science and Technology*, *58*, 1069-1081.
- Meirson, G. (2018). *Plaques production through HP-RTM for mechanical characterization*. London Ontario: Internal report/Fraunhofer Project Center@Western University.
- Mikhaluk, D. S., Truong, T. C., Borovkov, A. I., Lomov, S. V., & Verpoest, I. (2008). Experimental observations and finite element modelling of damage initiation and evolution in carbon/epoxy non-crimp fabric composites. *Engineering Fracture*

Mechanics, 75(9), 2751-2766.
doi:<https://doi.org/10.1016/j.engfracmech.2007.03.010>

- Montesano, J. (2012). Fatigue damage characterization of braided and woven fiber reinforced polymer matrix composites at room and elevated temperatures. *PhD dissertation*. Toronto, Ontario, Canada: Ryerson University.
- Montesano, J., & Singh, C. V. (2015). Predicting evolution of ply cracks in composite laminates subjected to biaxial loading. *Composites Part B: Engineering*, 75, 264-273.
- Montesano, J., McCleave, B., & Singh, C. V. (2018). Prediction of ply crack evolution and stiffness degradation in multidirectional symmetric laminates under multiaxial stress states. *Composites Part B: Engineering*, 133, 53-67. doi:<https://doi.org/10.1016/j.compositesb.2017.09.016>
- Moran, P., Liu, X., & Shih, C. (1995). Kink band formation and band broadening in fiber composites under compressive loading. *Acta Metallurgica et Materialia*, 43, 2943-2958.
- Ogihara, S., & Takeda, N. (1995). Interaction between transverse cracks and delamination during damage progress in CFRP cross-ply laminates. *Composites Science and Technology*, 54, 395-404.
- Olsson, R., Marklund, E., & Jansson, N. (2012). Testing of carbon/epoxy NCF strength under mixed in-plane loading. *15th European Conference on Composite Materials: Composites at Venice, ECCM*. Venice.
- Parvizi, A., Garrett, K. W., & Bailey, J. E. (1978). Constrained cracking in glass fiber-reinforced epoxy cross-ply laminates. *Journal of Materials Science*, 13, 195-201.
- Pereira, A., & de Morais, A. (2004). Mode II interlaminar fracture of glass/epoxy multidirectional laminates. *Composites: Part A*, 35, 265-272. doi:[doi:10.1016/j.compositesa.2003.09.028](https://doi.org/10.1016/j.compositesa.2003.09.028)

- Pereira, A., de Morais, A., Marques, A., & de Castro, P. (2004). Mode II interlaminar fracture of carbon/epoxy multidirectional laminates. *Composites Science and Technology*, *64*, 1653–1659. doi:doi:10.1016/j.compscitech.2003.12.001
- Pimenta, S., Gutkin, R., Pinho, S. T., & Robinson, P. (2009). A micromechanical model for kink-band formation: Part I — Experimental study and numerical modelling. *Composites Science and Technology*, *69*, 948-955.
- Pimenta, S., Gutkin, R., Pinho, S., & Robinson, P. (2009). A micromechanical model for kink-band formation: Part II—Analytical modelling. *Composites Science and Technology*, *69*, 956-964.
- Pinho, S. T., Darvizeh, R., Robinson, P., Schuecker, C., & Camanho, P. P. (2012). Material and structural response of polymer-matrix fibre-reinforced composites. *Journal of Composite Materials*, *46*, 2313-2341.
- Prabhakar, P., & Waas, A. M. (2013). Interaction between kinking and splitting in the compressive failure of unidirectional fiber reinforced laminated composites. *Composite Structures*, *98*, 85-92.
- Raz-Ben Aroush, D., Maire, E., Gauthier, C., Youssef, S., Cloetens, P., & Wagner, H. D. (2006). A study of fracture of unidirectional composites using in situ high-resolution synchrotron X-ray microtomography. *Composites Science and Technology*, *66*, 1348-1353.
- Reis, P., Ferreira, J., Antunes, F., Costa, J., & Capela, C. (n.d.). *Analysis of the initial delamination size on the mode I interlaminar fracture of carbon/epoxy composites*. Retrieved from <http://www.iccm-central.org/Proceedings/ICCM17proceedings/Themes/Behaviour/DEFORM%20&%20FRACTURE%20OF%20COMP/F8.5%20Reis.pdf>
- Robinson, P., & Song, D. (1991). A Modified DCB Specimen for Mode I Testing of Multidirectional Laminates. *Journal of composite materials*, *26*(11), 1554-1577.
- Rosen, B. W. (1964). *Mechanics of composite strengthening*. Washington, D.C.: NASA.

- Rouf, K., Suratkar, A., Imbert-Boyd, J., Wood, J., Worswick, M., & Montesano, J. (2021). Effect of Strain Rate on the Transverse Tension and Compression Behavior of a Unidirectional Non-Crimp Fabric Carbon Fiber/Snap-Cure Epoxy Composite. *Materials*, *14*, 1-18. doi:<https://doi.org/10.3390/ma14237314>
- Roylance, D. (2001, June 2001). *Introduction to Fracture Mechanics*. Retrieved from Massachusetts Institute of Technology: <https://web.mit.edu/course/3/3.11/www/modules/frac.pdf>
- Rzeczkowski, J. (2021). An experimental analysis of the end-notched flexure composite laminates beams with elastic couplings. *Continuum Mechanics and Thermodynamics*, *33*, 2331–2343. doi:<https://doi.org/10.1007/s00161-020-00903-2>
- Sakai, T., Wakayama, S., Pérez-Pacheco, E., Rodriguez-Laviada, J., & Rios-Soberanis, C. R. (2013). Damage accumulation behavior of non-crimp fabric-reinforced epoxy composite under static and cyclic tensile loading. *Advanced Composite Materials*, *22*(4), 281-297. doi:10.1080/09243046.2013.809636
- Sanford, R. J. (2003). *Principles of Fracture Mechanics*. The United States of America: Prentice Hall.
- Schreurs, P. G. (2012, September 6). Fracture Mechanics. *Lecture notes - course 4A780*. Eindhoven, Netherlands.
- Shen, H., Yao, W., Qi, W., & Zong, J. (2017). Experimental investigation on damage evolution in cross-ply laminates subjected to quasi-static and fatigue loading. *Composites Part B*, *120*, 10-26. doi:<http://dx.doi.org/10.1016/j.compositesb.2017.02.033>
- Shepard, S. M. (2007). Flash Thermography of Aerospace Composites. *IV Conferencia Panamericana de END*, (pp. 1-7). Buenos Aires.

- Shipsha, A., Burman, M., & Ekh, J. (2018). Failure of cross-ply NCF composites under off-axis compressive loads - An experimental study and a new strength prediction model including fibre bundle waviness. *Composites Part B*, *153*, 49-56.
- Shokrieh, M., Salamat-talab, M., & Heidari-Rarani, M. (2016). Effect of interface fiber angle on the R-curve behavior of E-glass/epoxy DCB specimens. *Theoretical and Applied Fracture Mechanics*, *86*, 153-160.
doi:<http://dx.doi.org/10.1016/j.tafmec.2016.06.006>
- Singh, C. V., & Talreja, R. (2010). Evolution of ply cracks in multidirectional composite laminates. *International Journal of Solids and Structures*, *47*, 1338-1349.
- Sisodia, S. M., Gamstedt, E., Edgren, F., & Varna, J. (2015). Effects of voids on quasi-static and tension fatigue behaviour of carbon-fibre composite laminates. *Journal of Composite Materials*, *49*(17), 2137-2148.
- Soutis, C. (1991). Measurement of the static compressive strength of carbon-fibre/epoxy laminates. *Composites Science and Technology*, *42*, 373-392.
- Soutis, C., & Fleck, N. A. (1990). Static Compression Failure of Carbon Fibre T800/924C Composite Plate with a Single Hole. *Journal of Composite Materials*, *24*, 536-558.
- Stress Concentrations at Holes*. (2022, March 12). Retrieved March 12, 2022, from Fracture Mechanics: <https://www.fracturemechanics.org/hole.html>
- Stress Intensity Factor*. (2022, March 13). Retrieved from Fracture Mechanics: <https://www.fracturemechanics.org/sif.html>
- Stresses At Elliptical Holes*. (2022, March 13). Retrieved from Fracture Mechanics: <https://www.fracturemechanics.org/ellipse.html>
- Sun, C., & Zheng, S. (1996). Delamination Characteristics of Double-Cantilever Beam and End-Notched Flexure Composite Specimens. *Composites Science and Technology*, *56*, 451-459.

- Sun, W., Guan, Z., Li, Z., Zhang, M., & Huang, Y. (2017). Compressive failure analysis of unidirectional carbon/epoxy composite based on micro-mechanical models. *Chinese Journal of Aeronautics*, 30(6), 1907-1918.
- Talreja, R. (1985). Transverse cracking and stiffness reduction in composite laminates. *Journal of Composite Materials*, 19(4), 355-375. doi:10.1177/002199838501900404
- Talreja, R. (2016). Physical modelling of failure in composites. *Philosophical Transactions of Royal Society A*, 374, 1-18.
- Tessema, A., Ravindran, S., & Kidane, A. (2018). Gradual damage evolution and propagation in quasi-isotropic CFRC under quasi-static loading. *Composite Structures*, 185, 186-192. doi:https://doi.org/10.1016/j.compstruct.2017.11.013
- Tessema, A., Ravindran, S., Wohlford, A., & Kidane, A. (2018). In-Situ Observation of Damage Evolution in Quasi-Isotropic CFRP Laminates. 67-72.
- The Elastic Stress Field around a Crack Tip*. (2022, March 13). Retrieved 2022, from Elsevier: https://booksite.elsevier.com/samplechapters/9780123850010/Chapter_3.pdf
- Thermoset Vs. Thermoplastics*. (2017). Retrieved from Modor Plastics: <http://www.modorplastics.com/thermoset-vs-thermoplastics>
- Totry, E., González, C., & Llorca, J. (2009). Failure locus of fiber-reinforced composites under transverse compression and out-of-plane shear. *Composites Science and Technology*, 68(3-4), 829-851.
- Trejo Sandoval, E. (2020). Characterizing the deformation response of a unidirectional non-crimp fabric for the development of computational draping simulation models. *UWSpace*. Retrieved from <http://hdl.handle.net/10012/15974>
- Truong, T. C., Vettori, M., Lomov, S., & Verpoest, I. (2005). Carbon composites based on multi-axial multi-ply stitched preforms. Part 4. Mechanical properties of

composites and damage observation. *Composites Part A: Applied Science and Manufacturing*, 36(9), 1207-1221.
doi:<https://doi.org/10.1016/j.compositesa.2005.02.004>

Tsampas, S. A., Greenhalgh, E. S., Ankersen, J., & Curtis, P. T. (2012). On compressive failure of multidirectional fibre-reinforced composites: A fractographic study. *Composites: Part A*, 43, 454-468.

Vallons, K. (2009). carbon fiber-epoxy NCF composites under various mechanical loading conditions. *PhD dissertation*. Leuven, Belgium: Katholieke Universiteit Leuven.

Varna, J. (2013). Modelling mechanical performance of damaged laminates. *Journal of Composite Materials*, 47(20-21), 2443-2474. doi:10.1177/0021998312469241

Varna, J. (2015). Strategies for stiffness analysis of laminates with microdamage: Combining average stress and crack face displacement based methods. *ZAMM-Journal of Applied Mathematics and Mechanics/Zeitschrift für Angewandte Mathematik und Mechanik*, 95(10), 1081-1097.
doi:<https://doi.org/10.1002/zamm.201400296>

Vogler, T. J., & Kyriakides, S. (2001). On the initiation and growth of kink bands in fiber composites: Part I. Experiments. *International Journal of Solids and Structures*, 38, 2639-2651.

Wang, Y., Burnett, T. L., Chai, Y., Soutis, C., Hogg, P. J., & Withers, P. J. (2017). X-ray computed tomography study of kink bands in unidirectional composites. *Composite Structures*, 160, 917-924.

Wang, Y., Emerson, M. J., Conradsen, K., Dahl, A. B., Dahl, V. A., Maire, E., & Withers, P. J. (2021). Evolution of fibre deflection leading to kink-band formation in unidirectional glass fibre/epoxy composite under axial compression. *Composites Science and Technology*, 213, 1-14.

- Westergaard's Solution for Cracks*. (n.d.). Retrieved from Fracture Mechanics:
<https://www.fracturemechanics.org/westergaard.html>
- Wilhelmsson, D. (2019). Compressive failure of unidirectional NCF composites. *PhD dissertation*. Göteborg, Sweden: Chalmers University of Technology.
- Wilhelmsson, D., Mikkelsen, L. P., Fæster, S., & Asp, L. E. (2019). Influence of in-plane shear on kink-plane orientation in a unidirectional fibre composite. *Composites Part A*, *119*, 283-290.
- Wisnom, M. R. (1990). The effect of fiber misalignment on the compressive strength of unidirectional carbon fiber/epoxy. *Composites*, *21*(5), 403-407.
- Wisnom, M. R. (1993). Analysis of Shear Instability in Compression Due to Fibre Waviness. *Journal of Reinforced Plastics and Composites*, *12*, 1171-1189.
- Wisnom, M. R. (2012). The role of delamination in failure of fibre-reinforced composites. *Philosophical Transactions of the Royal Society A*, *370*(1965), 1850-1870. doi:<https://doi.org/10.1098/rsta.2011.0441>
- Yang, M. (2019, August). Molecular weight and thermal properties of fiber reinforced polyamide-based composites throughout the direct long-fiber reinforced thermoplastic process. *Electronic Thesis and Dissertation Repository*. London, Ontario, Canada: Western University.
- Zeng, Y. (2020). Mechanical Characterization and Computational Modeling of Snap-cure Epoxy. *UWSpace*. Retrieved from <http://hdl.handle.net/10012/16308>
- Zhuang, L. (2018). Failure mechanisms in unidirectional composites under transverse and longitudinal tension. *PhD Dissertation*. Texas A&M University.
- Zhuang, L., Talreja, R., & Varna, J. (2016). Tensile failure of unidirectional composites from a local fracture plane. *Composites Science and Technology*, *133*, 119-127.

Zimmermann, E. A., Launey, M. E., & Ritchie, R. O. (2022, March 12). *Mixed-Mode Fracture of Human Cortical Bone*. Retrieved from <https://www2.lbl.gov/ritchie/Programs/BIO/MixedModeFracture.htm>

Zrida, H., Marklund, E., Ayadi, Z., & Varna, J. (2014). Master curve approach to axial stiffness calculation for non-crimp fabric biaxial composites with out-of-plane waviness. *Composites: Part B*, 64, 214-221.

Appendices

Appendix 1: Stress concentration equations

Kirsch's solution:

$$\sigma_{rr} = \frac{\sigma_{app}}{2} \left(1 - \left(\frac{a}{r} \right)^2 \right) + \frac{\sigma_{app}}{2} \left(1 - 4 \left(\frac{a}{r} \right)^2 + 3 \left(\frac{a}{r} \right)^4 \right) \cos 2\theta \dots (1.1)$$

$$\sigma_{\theta\theta} = \frac{\sigma_{app}}{2} \left(1 - \left(\frac{a}{r} \right)^2 \right) - \frac{\sigma_{app}}{2} \left(1 + 3 \left(\frac{a}{r} \right)^4 \right) \cos 2\theta \dots (1.2)$$

$$\tau_{r\theta} = -\frac{\sigma_{app}}{2} \left(1 + 2 \left(\frac{a}{r} \right)^2 - 3 \left(\frac{a}{r} \right)^4 \right) \sin 2\theta \dots (1.3)$$

Where 'r' is the radial component, 'a' is the radius of hole, ' σ_{app} ' is the applied tensile stress and ' θ ' is the angle of loading.

Inglis's solution:

$$\sigma_{max} = \sigma_{app} \left(1 + 2 \frac{a}{b} \right) \dots (1.4)$$

Where ' σ_{max} ' is the maximum stress at the crack tip, ' σ_{app} ' is the applied tensile stress, 'a' is the major axis of the ellipse and 'b' is the minor axis of the ellipse.

Westergaard's solution:

$$z = x + i y \dots (1.5)$$

$$\varphi = \operatorname{Re}(\bar{Z}) + y \operatorname{Im}(\bar{Z}) \dots (1.6)$$

$$Z(z) = \frac{\sigma_{app}}{\sqrt{1 - \left(\frac{a}{z}\right)^2}} \dots (1.7)$$

Where ' σ_{app} ' is the applied tensile stress, 'a' is the crack length, ' φ ' is the airy function,

' \bar{Z} ' is the integral of $Z(z)$ and 'x' and 'y' are rectangular co-ordinates.

Irwin's modification and near-field equations:

$$z = a + r e^{i\theta} \dots (1.8)$$

$$\sigma_x = \frac{K}{\sqrt{2\pi r}} f_x(\theta) + \sigma_{ox} \dots (1.9)$$

$$\sigma_y = \frac{K}{\sqrt{2\pi r}} f_y(\theta) \dots (1.10)$$

$$\tau_{xy} = \frac{K}{\sqrt{2\pi r}} f_{xy}(\theta) \dots (1.11)$$

Where ' σ_x ', ' σ_y ' and ' τ_{xy} ' are the stresses in x, y and xy planes respectively, 'a' is the crack length, 'K' is the stress intensity factor (in any loading mode) and ' $f_x(\theta)$ ', ' $f_y(\theta)$ ' and ' $f_{xy}(\theta)$ ' are the angular dependency functions in x, y and xy planes respectively. ' σ_{ox} ' is a secondary correction factor, which influences the localized yielding behaviour at the crack tip.

Appendix 2: EPIKOTE™ Resin TRAC 06150 resin data sheet



Technical Data Sheet

Most recent revision date:

3/17/2015

EPIKOTE™ Resin TRAC 06150

(Formerly named EPIKOTE™ Resin 05475)

EPIKURE™ Curing Agent TRAC 06150

(Formerly named EPIKURE™ Curing Agent 05443)

HELOXY™ Additive TRAC 06805

(Formerly named HELOXY™ Additive 112)

Product Description

EPIKOTE™ Resin TRAC 06150 is a medium viscosity epoxy resin.
EPIKURE™ Curing Agent TRAC 06150 is a low viscosity amine hardener.
HELOXY™ Additive TRAC 06805 is a silicone- and wax-free internal mold release agent.

Application Areas/Suggested Uses

Low viscous resin system designed for RTM applications with excellent wetting and adhesion characteristics on glass-, carbon- or aramid-fibers. Benefits of this system are a low viscosity during infusion (2 min at 100°C < 150mPas) and a short curing cycle, which allows an early de-molding (e.g. 5 min at 120°C).

The EPIKOTE™ Resin TRAC 06150 with EPIKURE™ Curing Agent TRAC 06150 system is compatible with the internal mold release agent HELOXY™ Additive TRAC 06805, which can be added in a recommended amount of about 1 – 2 phr.

Typical suggested uses include but are not limited to the production of structural automotive parts such as parts of the frame or chassis, floor panels, bulkheads monocoque structure, and exterior and visible structural parts such as roof tops, pillars, heads and deck lids.

Benefits

- Low viscosity during injection.
- Easy to process due to thermolatent behavior:
 - Long infusion time (90 sec at 120°C)
 - Fast glass transition temperature (T_g) development
 - Short curing cycle (e.g. 5 min at 120°C)
- Excellent fiber wetting properties.
- Excellent thermal and mechanical performance.
- Good surface quality for painted parts.

page 1 of 5

The information provided herein was believed by Hexion Inc. and its affiliated companies ("Hexion") to be accurate at the time of preparation or prepared from sources believed to be reliable, but it is the responsibility of the user to investigate and understand other pertinent sources of information, to comply with all laws and procedures applicable to the safe handling and use of the product and to determine the suitability of the product for its intended use. All products supplied by Hexion are subject to Hexion's terms and conditions of sale. HEXION MAKES NO WARRANTY, EXPRESS OR IMPLIED, CONCERNING THE PRODUCT OR THE MERCHANTABILITY OR FITNESS THEREOF FOR ANY PURPOSE OR CONCERNING THE ACCURACY OF ANY INFORMATION PROVIDED BY HEXION, except that the product shall conform to Hexion's specifications at the time of delivery. Nothing contained herein constitutes any offer for the sale of any product.
© 2015 Hexion Inc. All rights reserved.
® and TM denote trademarks owned or licensed by Hexion Inc.

Vanzler Straße 49
47135 Duisburg-Heiderich
Postfach 130552
47135 Duisburg
Germany
www.hexion.com

03/2015


Technical Data Sheet

Most recent revision date:

3/17/2015

Sales Specifications
EPIKOTE™ Resin TRAC 06150

Property	Unit	Value	Test Method
Viscosity at 25°C	mPa·s	8000 - 10000	DIN 53015
Color Gardner		0 - 3	ISO 4630
Refractive index at 25°C		1.569 - 1.575	DIN 51423

EPIKURE™ Curing Agent TRAC 06150

Property	Unit	Value	Test Method
Viscosity at 25°C	mPa·s	10 - 20	DIN 53015

HELOXY™ Additive TRAC 06805

Property	Unit	Value	Test Method
Viscosity at 30°C	mPa·s	750 ± 450	DIN 53015

Typical Properties
EPIKOTE™ Resin TRAC 06150

Property	Unit	Value	Test Method
Delivery form		liquid	
Density at 20°C	kg/l	1.15 - 1.19	ISO 2811

EPIKURE™ Curing Agent TRAC 06150

Property	Unit	Value	Test Method
Delivery form		liquid	
Density at 20°C	kg/l	0.97	DIN 16945

HELOXY™ Additive TRAC 06805

Property	Unit	Value	Test Method
Delivery form		liquid	
Density at 20°C	kg/l	1.01 ± 1.05	DIN 51755
Appearance		yellow/brown	


Technical Data Sheet

Most recent revision date: 3/17/2015

Processing Details
Mixing ratio

EPIKOTE™ Resin TRAC 06150	100	parts by weight
EPIKURE™ Curing Agent TRAC 06150	24	parts by weight
HELOXY™ Additive TRAC 06805	1-2	parts by weight

Mixing tolerance

The maximum allowable mixing tolerance (resin & hardener) is ± 1 pbw, but it is particularly important to preserve the recommended mixing ratio as accurately as possible. Incorrect dosing of the hardener is not an appropriate approach to accelerate or retard the reaction; rather it will lead to an incomplete cure. The reaction speed can be properly adjusted by changing the processing temperature, as indicated below. Resin and hardener must be mixed very thoroughly. Mix until no clouding is visible, pay special attention to the walls and the bottom of the mixing container.

Material preheating

To optimize the process a preheating of the components is recommended.

EPIKOTE™ Resin TRAC 06150	60-80	°C
EPIKURE™ Curing Agent TRAC 06150	RT-30	°C
HELOXY™ Additive TRAC 06805	25-30	°C

Processing Temperature

The system exhibits good processing in the temperature range between 80 and 140 °C, and full curing can typically be achieved in 5 minutes cure at 120°C. Higher processing temperatures are possible but will shorten the pot life. A rise in temperature of 10 °C reduces the pot life by approx. 50%. Different temperatures during processing have no significant effect on the mechanical properties of the hardened product.

Do not mix large quantities at elevated processing temperatures as this can lead to an uncontrolled exothermic reaction where the mixture may heat up very quickly to more than 200 °C in the mixing container.

Processing Data		Unit	Value
Viscosity of formulation	at 25°C	mPa·s	1200 \pm 100
	at 80°C	mPa·s	30 \pm 5
	at 100°C	mPa·s	13 \pm 3
Pot life	at 25°C	min	120 \pm 10
Gel time	at 80°C	s	330 \pm 30
	at 100°C	s	210 \pm 30
	at 120°C	s	150 \pm 30
	at 140°C	s	90 \pm 30
Viscosity increase after 60s / 120s / 180s	at 80°C	mPa·s	47/63/100
	at 100°C	mPa·s	33/123/1402
	at 120°C	mPa·s	40/865/>100000
	at 140°C	mPa·s	20070/>100000/-

page 3 of 5

The information provided herein was believed by Hexion Inc. and its affiliated companies ("Hexion") to be accurate at the time of preparation or prepared from sources believed to be reliable, but it is the responsibility of the user to investigate and understand other pertinent sources of information, to comply with all laws and procedures applicable to the safe handling and use of the product and to determine the suitability of the product for its intended use. All products supplied by Hexion are subject to Hexion's terms and conditions of sale. HEXION MAKES NO WARRANTY, EXPRESS OR IMPLIED, CONCERNING THE PRODUCT OR THE MERCHANTABILITY OR FITNESS THEREOF FOR ANY PURPOSE OR CONCERNING THE ACCURACY OF ANY INFORMATION PROVIDED BY HEXION, except that the product shall conform to Hexion's specifications at the time of delivery. Nothing contained herein constitutes any offer for the sale of any product. © 2015 Hexion Inc. All rights reserved. ® and TM denote trademarks owned or licensed by Hexion Inc.

 Varzner Straße 49
 47135 Duisburg-Meiderich

 Postfach 132652
 47125 Duisburg

Germany

www.hexion.com

02/2015

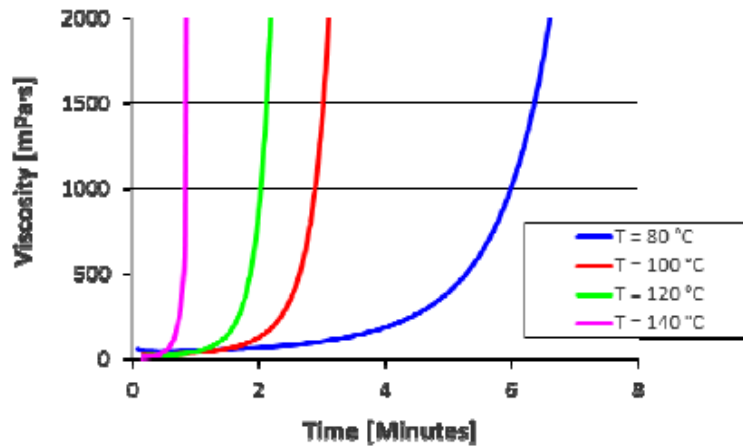


Technical Data Sheet

Most recent revision date:

3/17/2015

Viscosity profiles data of formulation at different temperatures



Typical Properties of the cured, non-reinforced system

Cast by hand; curing cycle: 5 min at 120°C

Properties	Unit	Value	Test Method
T _g , DSC Onset	°C	118 ± 2	DSC (10K/min)
Midpoint	°C	124 ± 2	
Thermal expansion coefficient	ppm/K	< 75	ISO 11359-2
Tensile test at RT			DIN EN ISO 527-1
Tensile strength	MPa	85 ± 2	
Tensile modulus	MPa	2900 ± 100	
Elongation at break	%	6 - 8	
Bending test at RT			DIN EN ISO 178
Flexural strength	MPa	130 ± 5	
Flexural modulus	MPa	3000 ± 100	
Charpy impact at RT	mJ/mm ²	24 ± 2	ISO 179
Fracture performance at RT			ISO 17281
Fracture toughness K _{1C}	MPa√m	0.75 ± 0.05	
Fracture energy G _{1C}	J/m ²	225 ± 5	
Water uptake (7d at 23°C)	%	< 0.4	DIN EN ISO 62
Total shrinkage at RT	Vol. %	< 4	Calculated DIN 16945
Hardness at RT	Shore D	85 - 86	DIN 53505-D
Density at 23°C	kg/l	1.151 - 1.155	DIN 53479 A

page 4 of 5

The information provided herein was believed by Hexion Inc. and its affiliated companies ("Hexion") to be accurate at the time of preparation or prepared from sources believed to be reliable, but it is the responsibility of the user to investigate and understand other pertinent sources of information, to comply with all laws and procedures applicable to the safe handling and use of the product and to determine the suitability of the product for its intended use. All products supplied by Hexion are subject to Hexion's terms and conditions of sale. HEXION MAKES NO WARRANTY, EXPRESS OR IMPLIED, CONCERNING THE PRODUCT OR THE MERCHANTABILITY OR FITNESS THEREOF FOR ANY PURPOSE OR CONCERNING THE ACCURACY OF ANY INFORMATION PROVIDED BY HEXION, except that the product shall conform to Hexion's specifications at the time of delivery. Nothing contained herein constitutes any offer for the sale of any product. © 2015 Hexion Inc. All rights reserved. ® and TM denote trademarks owned or licensed by Hexion Inc.

Vanziner Straße 49
47135 Duisburg-Hedderich
Postfach 120552
47125 Duisburg
Germany
www.hexion.com

03/2015


Technical Data Sheet

Most recent revision date: 3/17/2015

Safety, Storage & Handling

Please refer to the MSDS for the most current Safety and Handling information.

EPIKOTE™ Resin TRAC 06150 should be stored at room temperature in its carefully sealed original containers. Under these conditions the shelf life is a minimum of three years from date of certification.

EPIKURE™ Curing Agent TRAC 06150 should be stored at room temperature in its carefully sealed original containers, so that moisture is excluded. Under these conditions the shelf life is a minimum of two years from date of certification. Care should be taken to avoid storage environments resulting in moisture contamination. Exposure to moisture will cause an increase in viscosity and reactivity, the degree of increase depending on the amount of moisture, which has been absorbed.

HELOXY™ Additive TRAC 06805 should be stored at room temperature in its carefully sealed original containers, so that moisture is excluded. Under these conditions the shelf life is a minimum of 6 months.

HELOXY™ Additive TRAC 06805 should not be stored at temperatures above 30°C. Before use it is necessary to homogenize the material by shaking or stirring.

Occasionally, it is possible that the resin or the hardener crystallize at temperatures below 15°C. The crystallization is visible as a clouding or solidification of the content of the container. Before processing, the crystallization must be removed by warming up. Slow warming up to 50 - 60°C in a water bath or oven and stirring or shaking will clarify the contents in the container without any loss of quality. Use only completely clear products. Before warming up, open containers slightly to permit equalization of pressure. Caution during warm up! Do not warm up over open flame! While stirring up use safety equipment (gloves, eyeglasses, respirator equipment).

Contact Information

For further Technical Inquiries on the properties and performance of this matrix system in reinforced composites, please contact us at our Customer Service Center +1 888 443 9466 / Hexion4information@Hexion.com

Appendix 3: ZOLTEK™ PX35 unidirectional fabric data sheet

Technical Datasheet

ZOLTEK™ PX35 Uni-Directional Fabrics



Stitch-Bonded Uni-Directional Carbon Fabrics

DESCRIPTION

ZOLTEK PX35 Stitch-Bonded Uni-Directional Carbon Fabrics are produced from our ZOLTEK PX35 50K Continuous Tow Carbon Fiber. Unique fiber spreading techniques are utilized to obtain a wide range of UD fabric weights for a varied set of composite part applications. Quick composite part build-up is cost effectively achieved with our diverse weight range of low-cost carbon fabric products.



MATERIAL OVERVIEW	UD150	UD200	UD300	UD400	UD500	UD600	UD900V
0° Carbon ZOLTEK PX35 50K	158	200	309	403	500	600	865
90° Glass 34 dtex	10	10	10	10	10	10	—
Polyester Veil	—	—	—	—	—	—	30
Polyester Stitch 76 dtex	6	6	6	6	6	6	5
Total Fabric Weight	182 g/m ² 5.37 oz/yd ²	224 g/m ² 6.61 oz/yd ²	333 g/m ² 9.82 oz/yd ²	419 g/m ² 12.36 oz/yd ²	516 g/m ² 15.22 oz/yd ²	624 g/m ² 18.40 oz/yd ²	900 g/m ² 26.54 oz/yd ²

Average Values Shown

*Epoxy resin binder available upon customer request.

FABRIC CONSTRUCTION	UD150	UD200	UD300	UD400	UD500	UD600	UD900V
Stitch Length	A variety of stitch lengths are available to meet application requirements.						
Stitch Pattern	A variety of stitch patterns are available to meet application requirements.						
Cured Thickness/Ply	.21 mm	.25 mm	.37 mm	.46 mm	.57 mm	.69 mm	1.00 mm
Roll Width	30 cm - 61 cm - 122 cm						122 cm
Roll Length	100 m				50 m		30 m

Average Values Shown

The properties listed in this datasheet do not constitute any warranty or guarantee of values. This information should only be used for the purposes of material selection. Please contact us for more details.

ZOLTEK™ PX35



ZOLTEK Corporation | 3101 McKelvey Road | Bridgeton, MO 63044
P: 314-291-5110 | F: 314-291-8536 | www.zoltek.com

Technical Datasheet

ZOLTEK™ PX35 Uni-Directional Fabrics



Stitch-Bonded Uni-Directional Carbon Fabrics

COMPOSITE PROPERTIES	SI	US	METHOD
Tensile Strength	1,400 MPa	203 ksi	DIN EN ISO 527
Tensile Modulus	1.19 GPa	17.2 msi	DIN EN ISO 527
Compressive Strength	980 MPa	142 ksi	DIN EN ISO 14126
Compressive Modulus	1.18 GPa	17.5 msi	DIN EN ISO 14126
Flexural Strength	1,290 MPa	187 ksi	DIN EN ISO 14125
Flexural Modulus	1.12 GPa	16.2 msi	DIN EN ISO 14125

Typical Fiber Volume Fraction (FVF) is 55%.
Standard Epoxy Resin System

The properties listed in this datasheet do not constitute any warranty or guarantee of values. This information should only be used for the purposes of material selection. Please contact us for more details.

TYPICAL PACKAGING

Wound on cardboard cone, sealed in polyethylene bag, and placed in cardboard box. Rolls stacked horizontally on pallets when shipping.

+ Requirements other than standard widths and roll lengths should be specified by purchase order.

CERTIFICATION

ZOLTEK PX35 Fabrics are manufactured in accordance with ZOLTEK's written and published data. A Certificate of Conformance is provided with each shipment.

SAFETY

Obtain, read, and understand the Material Safety Data Sheet (SDS) before use of this or any other ZOLTEK product.

APPROVAL

DNV-GL has granted approval to ZOLTEK PX35 Uni-Directional Fabrics for use in wind energy applications.



DNV·GL

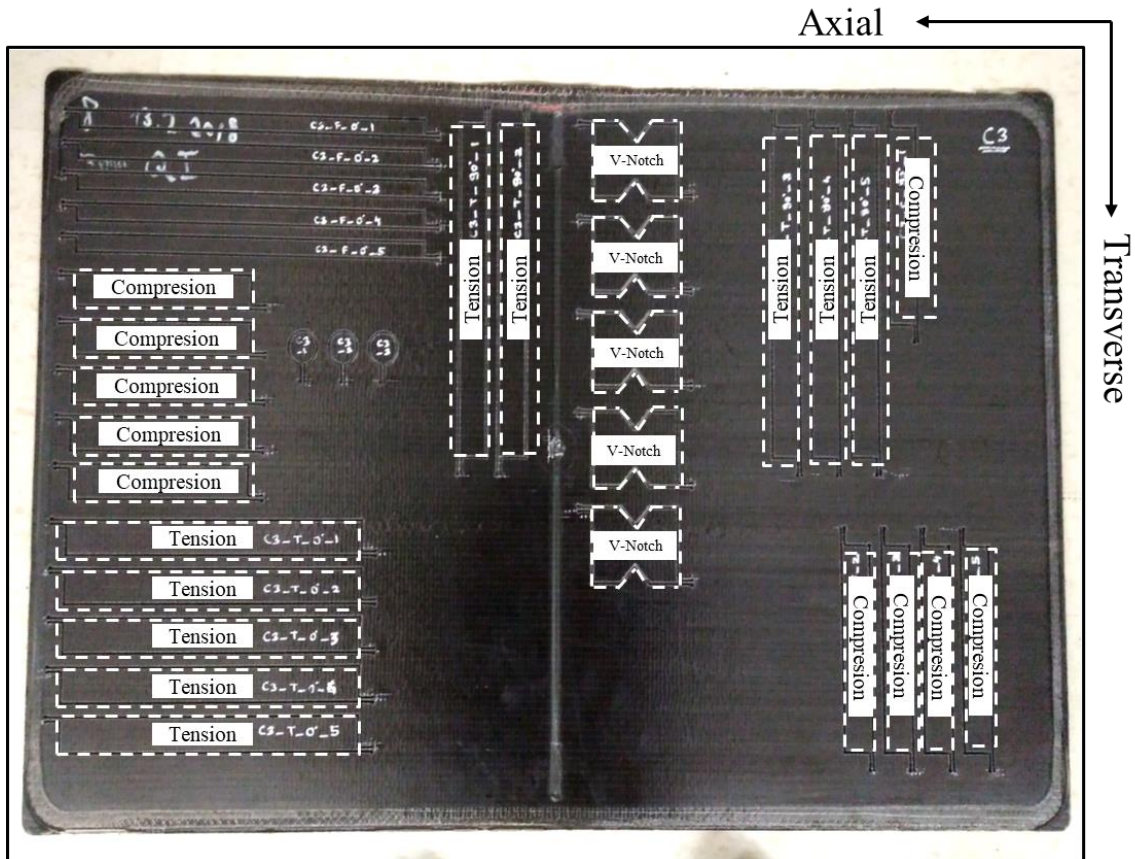
Approval No. WP 1030011 HH

ZOLTEK™ PX35



ZOLTEK Corporation | 3101 McKelvey Road | Bridgeton, MO 63044
P: 314-291-5110 | F: 314-291-8536 | www.zoltek.com

Appendix 4: Plaque of NCF composites manufactured using HP-RTM process with specimen cutting position



Appendix 5: Alternate data reduction methods for Mode-I fracture toughness

One of the data reduction methods for calculation of Mode-I interlaminar fracture toughness in ASTM D5528 is Modified Bending Theory (MBT). The expression for fracture toughness by standard beam theory is:

$$G_I = \frac{3P\delta}{2ba}$$

Where:

P = load (N)

δ = load point displacement (mm)

b = width (mm)

a = crack length (mm)

However, this expression does not account for possible rotation at the delamination front and hence overestimates the fracture toughness. This expression was corrected by considering a slightly longer crack length through inclusion of Δ , which is x-intercept of least squares plot of cube root of compliance as a function of crack length. The MBT expression, hence, is:

$$G_I = \frac{3P\delta}{2b(a + \Delta)}$$

Another alternative for G_I calculation in ASTM D5528 is Compliance Calibration (CC) method. In this method, a plot of logarithm of compliance versus logarithm of crack lengths is plotted. The slope (n) of this plot is determined and used in the expression:

$$G_I = \frac{nP\delta}{2ba}$$

In case of Mode-I fracture toughness testing, the loads required for crack extension are very low (in the order of few 100 N). In the cases where load cells of higher capacities

are used, the load data contains a high amount of signal-to-noise ratio. A direct, closed-form load-independent equation (de Verdiere, Skordos, May, & Walton, 2012; Isakov, May, Paul, & Nishi, 2019) has hence been developed in the literature:

$$G_I = \frac{9EI\delta^2}{4ba^4}$$

Where:

E = Young's modulus (N/mm²)

I = area moment of inertia (mm⁴)

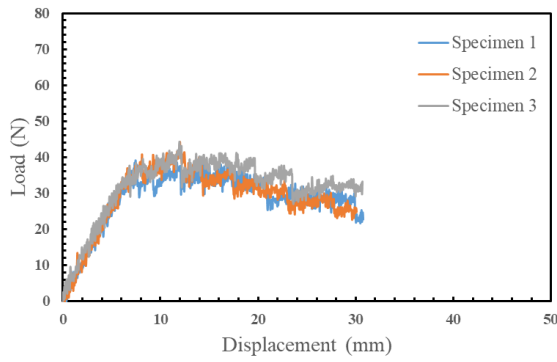
Other symbols stand for the same parameters as mentioned before.

The calculated fracture toughness values by any of the data reduction methods do not differ from each other by more than 3.1%, as is reported in the ASTM D5528.

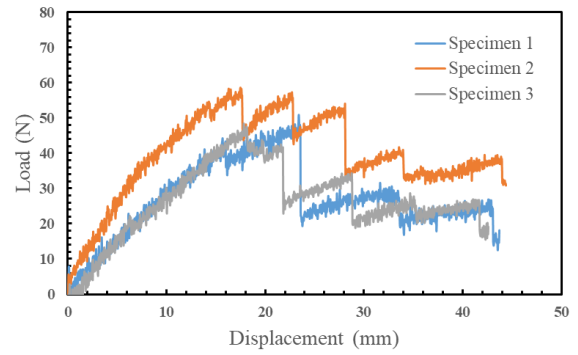
Appendix 6: Engineering properties of NCF carbon fiber epoxy composites under quasi-static loads

	UD lamina ([0] ₇ /[0] ₁₁)	UD lamina ([90] ₇ /[90] ₁₁)	[0/±45/90] _s	[90/±45/0] _s	[±45/0 ₂] _s	[±45/90 ₂] _s
E_t (GPa)	121 (±7)	8 (±0.3)	42 (±0.3)	42 (±0.5)	62 (±3)	18 (±0.4)
σ_t (MPa)	1637 (±168)	60 (±4)	546 (±18)	532 (±29)	934 (±1)	135 (±5)
ε_t (%)	0.66 (±0.07)	0.66 (±0.07)	1.30 (±0.10)	1.30 (±0.10)	1.80 (±0.55)	1.80 (±0.55)
ν_{xy}	0.37 (±0.01)	----	0.35 (±0.04)	----	0.71 (±0.01)	----
E_c (GPa)	122 (±2)	9 (±0.8)	37 (±3)	31 (±1)	59 (±1)	18 (±1)
σ_c (MPa)	1001 (±97)	145 (±4)	384 (±48)	265 (±27)	399 (±35)	179 (±0)
ε_c (%)	0.80 (±0.09)	2.42 (±0.33)	1.10 (±0.21)	1.00 (±0.17)	0.72 (±0.14)	1.13 (±0.00)
G_{xy} (GPa)	3.55 (±0.14)	----	----	----	----	----
τ_{xy} (MPa)	90 (±2)	----	----	----	----	----
γ_{xy} (%)	8.88 (±1.90)	----	----	----	----	----

Appendix 7: Unfiltered load-displacement curves under Mode-I loads

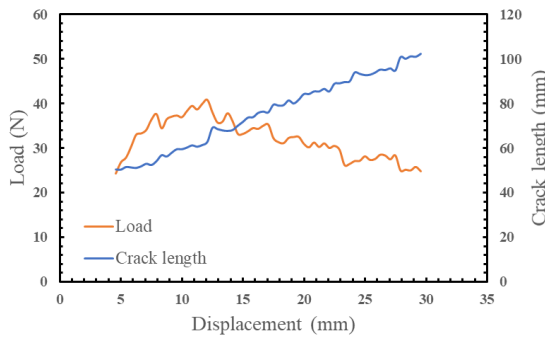


Unidirectional lamina

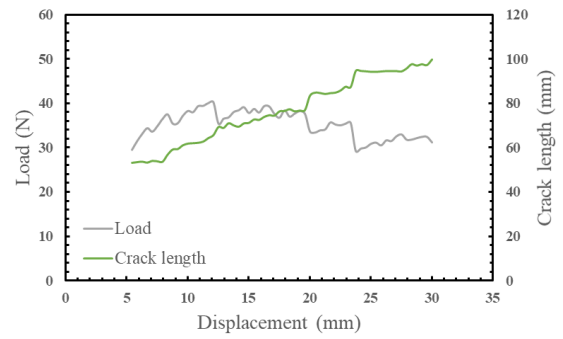


Cross-ply laminate

Appendix 8: Mode-I crack growth characteristics in unidirectional lamina

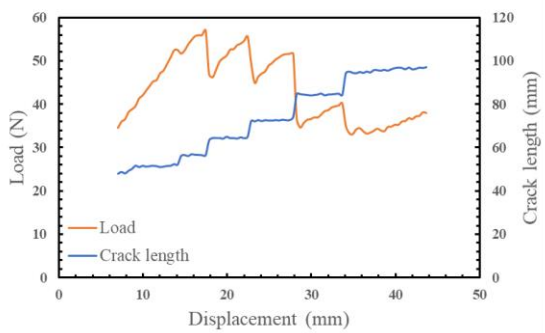


Specimen (a)

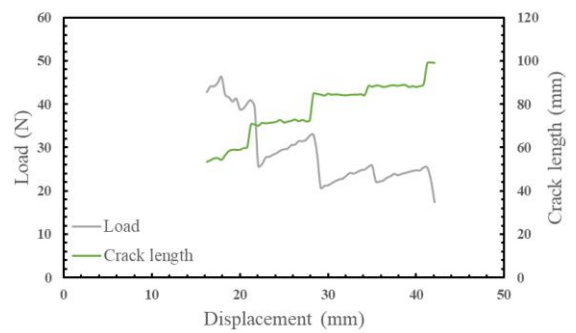


Specimen (b)

Appendix 9: Mode-I crack growth characteristics in cross-ply laminates

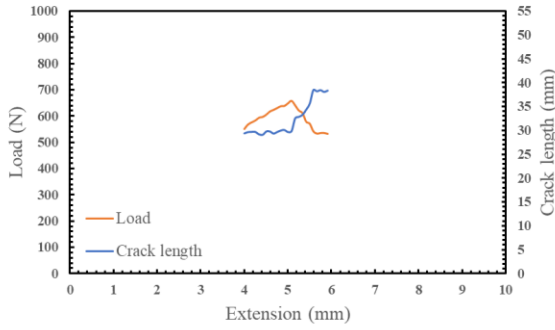


Specimen (a)

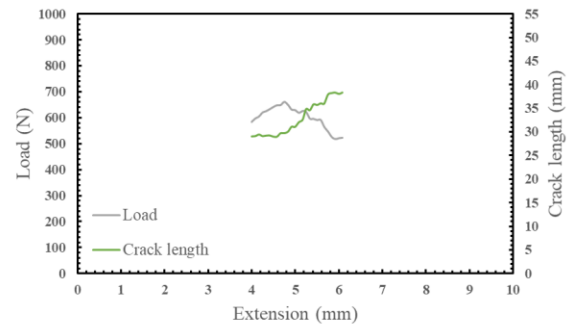


Specimen (b)

Appendix 10: Mode-II crack growth characteristics in unidirectional lamina

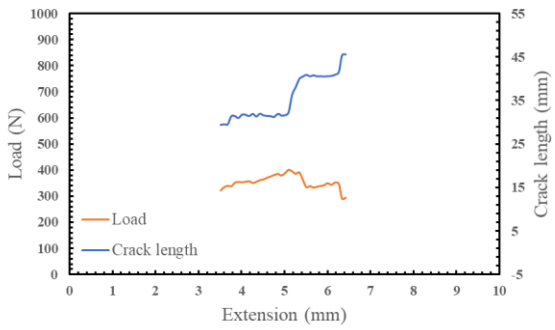


Specimen (a)

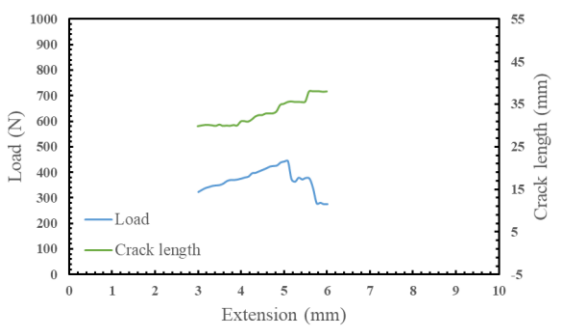


Specimen (b)

Appendix 11: Mode-II crack growth characteristics in cross-ply laminates

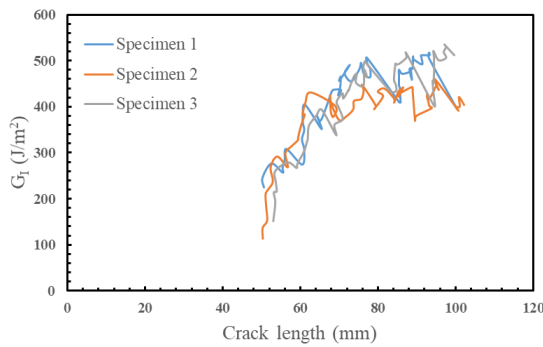


Specimen (a)

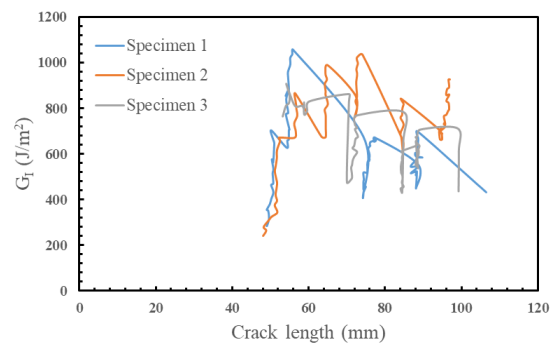


Specimen (b)

Appendix 12: R-curves under Mode-I opening loads

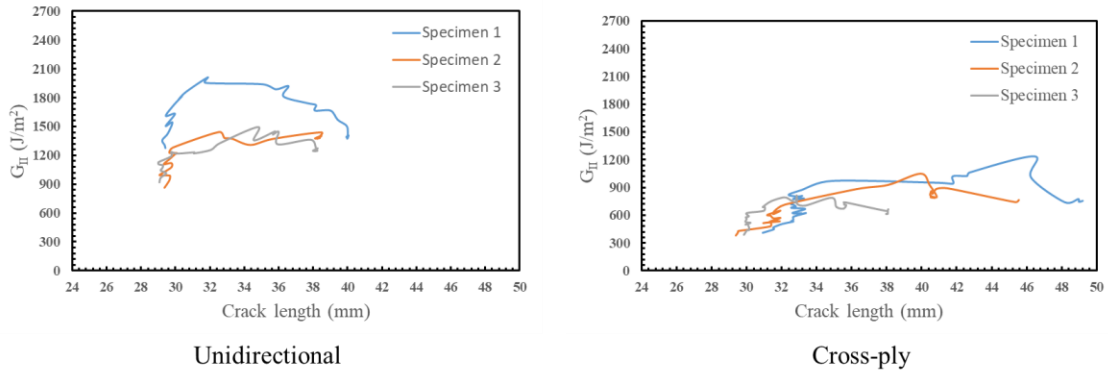


Unidirectional



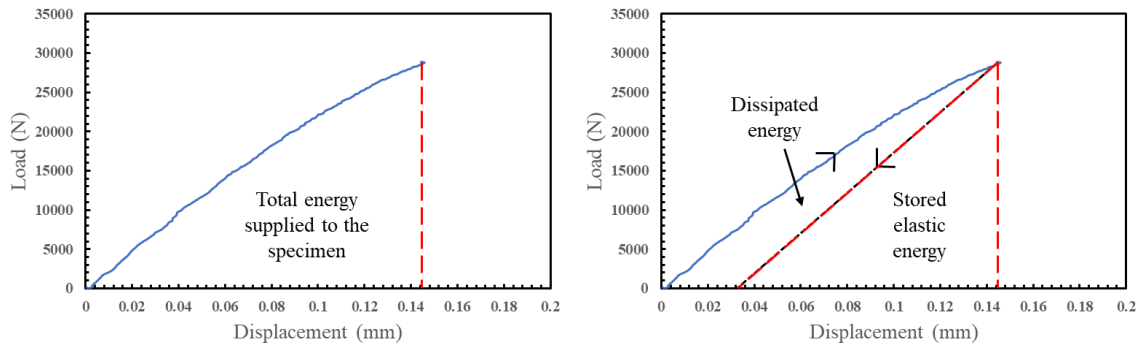
Cross-ply

Appendix 13: R-curves under Mode-II shearing loads



Appendix 14: Energy balance for damage in composites

The energies stored and dissipated in the composites upon application of mechanical loads can be determined from the load-displacement curves. Let us consider the mechanical response of and the associated energy balance in $[0/\pm 45/90]_s$ laminate under an axial compressive load as an example.



Energy balance in $[0/\pm 45/90]_s$ laminate under axial compression

The total energy supplied to a specimen is determined by calculating the area under the load-displacement curve. The total energy can be resolved into two components: 1. The energy permanently dissipated and lost 2. The recoverable energy stored elastically in the material. The total energy is mathematically expressed as a summation of the two aforementioned energies.

Determination of stored elastic energy at a particular displacement during the test requires unloading data at that point. In the load-displacement curves above, it is assumed that the unloading curve traces a path parallel to the initial elastic region back to zero load. The area enclosed in the triangle formed by X-axis and the two red dashed lines in the figure on the right is the elastic energy stored in the material.

The energy dissipated is a subtraction of stored elastic energy from the total energy. This is the energy which is either lost to the surroundings in forms such as heat or is utilized in the creation of permanent damage in the system. The lost energy is assumed to be negligible in this study.

In the $[0/\pm 45/90]_s$ laminate under axial compression, the dissipated energy is primarily utilized in the creation of a single matrix shear crack passing through the off-axis plies and a delamination crack along $0/+45$ interface. Any other secondary damage mechanisms are ignored. Furthermore, visual inspections confirm that the cracks span the entire width. The geometrical parameters of the specimens are also known.

Above data is sufficient to compute the amounts of energies spent in creation of matrix shear crack and then predict the extent of delamination. A matrix shear crack is a crack present at certain angle to the specimen cross section. Hence, the area of the matrix shear crack will be a product of width of the specimen and total thickness of the off-axis plies through which the crack is present, divided by sine of the angle of crack inclination. The area of delamination crack is simply length of the crack multiplied by the width of the specimen.

The damage area is then multiplied by the critical strain energy release rate of that particular damage mode to determine the energy expended in creation of that damage mode.

Appendix 15: Energies supplied, stored elastically and dissipated in multidirectional composites under compression

Laminate	Total energy supplied (J)	Stored elastic energy (J)	Energy dissipated (J)
$[0/\pm 45/90]_s$	2.127	1.577	0.550
$[90/\pm 45/0]_s$	1.214	0.771	0.443
$[\pm 45/0_2]_s$	1.211	0.987	0.224
$[\pm 45/90_2]_s$	0.704	0.584	0.121

Scholarly contributions

Journal publications:

Rouf, K., **Suratkar, A.**, Imbert-Boyd, J., Wood, J., Worswick, M., & Montesano, J. (2021). Effect of Strain Rate on the Transverse Tension and Compression Behavior of a Unidirectional Non-Crimp Fabric Carbon Fiber/Snap-Cure Epoxy Composite. *Materials*, *14*, 1-18. doi: <https://doi.org/10.3390/ma14237314>

Conference appearances:

Suratkar, A., Montesano, J., Wood, J. (2021, November). Mode I and Mode II fracture toughness measurement for Non-Crimp Fabric carbon fiber reinforced epoxy composites. Oral presentation at 21st Annual SPE Automotive Composites Conference & Exhibition, Novi, Michigan, United States of America.

Suratkar, A., Montesano, J., Wood, J. (2021, September). Damage Evolution in non-crimp fabric carbon fiber/epoxy multi-directional laminates under quasi-static tension. Oral presentation at and publication in the digital proceedings of 36th American Society of Composites Technical Virtual Conference, College Station, Texas, United States of America.

Suratkar, A., Fan, Y., Montesano, J., Wood, J. (2019, September). Energy absorption mechanisms in impacted non-crimp fabric CFRPs. Oral presentation at 19th Annual SPE Automotive Composites Conference & Exhibition, Novi, Michigan, United States of America.

Suratkar, A., Fan, Y., Montesano, J., Wood, J. (2019, June). Mechanisms of Fracture in Non-Crimp Fabric Carbon Fiber Reinforced Epoxy Composites. Oral presentation at Canadian Society of Mechanical Engineers Conference, London Ontario, Canada.

Suratkar, A., Fan, Y., Montesano, J., Wood, J. (2019, September). Damage Characterization of Unidirectional Non-Crimp Fabric Carbon Fiber Epoxy Composites Subject to Impact Loads. Poster presentation at 19th Annual SPE Automotive Composites Conference & Exhibition, Novi, Michigan, United States of America.

Suratkar, A., Fan, Y., Montesano, J., Wood, J. (2018, September). Quasi-Static Mechanical Characterization of Non-crimp Carbon Fiber Reinforced Epoxy Laminates Manufactured using HP-RTM Process. Poster presentation at 18th Annual SPE Automotive Composites Conference & Exhibition, Novi, Michigan, United States of America.

Curriculum Vitae

AADITYA SURATKAR

PhD candidate, Mechanical and Materials engineering department

Overview of key skills

- Mechanical characterization of polymer composites
- In-situ damage assessment in thermoset carbon composites
- Fiber/matrix interfacial strength characterization of composites
- Chemical synthesis of novel polymer composite systems like self-healing composites and “living materials”
- Can effectively communicate in several major languages, including English, German and Mandarin
- Experience with leadership of multi-cultural teams

Education

WESTERN UNIVERSITY, CANADA

Doctor of Philosophy (Ph.D.)

2018 – 2022

Mechanical and Materials engineering

- PhD project focused on mechanical characterization and damage evolution at quasi-static rates in Non-Crimp Fabric carbon fiber/epoxy composites for structural application in light weight vehicles.
- The project, funded and driven by NSERC, major OEM and raw material suppliers in automotive industry, is conducted in a team consisting of several PIs, PostDoc fellows, PhD candidates and MSc students from Western University and University of Waterloo.
- Research presented in four international conferences with audience from Americas, Europe, Middle East, Africa and Asia-Pacific. Several journal publications currently under review.

TU DELFT, THE NETHERLANDS

Master of Science (M.Sc., Hons.)

2015 - 2017

Chemical product engineering

- Successfully reduced the elastic modulus of rigid worm-like micelles by 79% and cross-linked them to form a biomimetic semi-flexible hydrogel. The research resulted in a publication in *Macromolecules*, a peer reviewed 5.914 impact factor scientific journal.
- Conducted a first-ever study on recoveries of dielectric strengths of self-healing polymers over multiple breakdown and healing cycles.

THADOMAL SHAHANI ENGINEERING COLLEGE (TSEC), MUMBAI UNIVERSITY, INDIA

Bachelor of Engineering (B.E.)

2011 - 2015

Chemical engineering

- Demonstrated a theoretical 54% reduction in distillation utility cost using pinch technology.
- Proposed strategies to recycle and reuse process water, together with techno-economic feasibility, from product lines at Rubber Chemicals department during summer internship at LANXESS AG plant in Gujarat, India.

Work experience

FRAUNHOFER I.C.T., GERMANY

Research intern

April, 2017 - August, 2017

Research assistant

November, 2017 - January, 2018

Thermoplastics processing group

- Characterized the influence of change in processing temperature on fiber-matrix adhesion on resultant compression strengths in GF/PP thermoplastics.
- Investigated crystallization kinetics in self-reinforced PLA composites

Major conference presentations and publications

- **Suratkar, A., Montesano, J., Wood, J.** (2021, November). Mode I and Mode II fracture toughness measurement for Non-Crimp Fabric carbon fiber reinforced epoxy composites. Oral presentation at 21st Annual SPE Automotive Composites Conference & Exhibition, Novi, Michigan, United States of America.
- **Suratkar, A., Montesano, J., Wood, J.** (2021, September). Damage Evolution in non-crimp fabric carbon fiber/epoxy multi-directional laminates under quasi-static tension. Oral presentation at and publication in the digital proceedings of 36th American Society of Composites Technical Virtual Conference, College Station, Texas, United States of America.
- **Suratkar, A., Fan, Y., Montesano, J., Wood, J.** (2019, June). Mechanisms of Fracture in Non-Crimp Fabric Carbon Fiber Reinforced Epoxy Composites. Oral presentation at Canadian Society of Mechanical Engineers Conference, London Ontario, Canada.
- **Zhang, K., Suratkar, A., Vedaraman, S., Lakshminarayanan, V., Jennings, L., Glazer, P., Van Esch, J., Mendes, E.** (2018). Two Robust Strategies toward Hydrogels from Quenched Block Copolymer Nanofibrillar Micelles. *Macromolecules*, 51(15), 5788-5797. <https://doi.org/10.1021/acs.macromol.8bo1158>

Achievements and scholarships

- Awarded Honours certificate by Applied Science Department of TU Delft in 2017.
- Ranked 2nd and 1st in department of chemical engineering at University of Mumbai and TSEC respectively in class of 2015.
- Selected as Department Ambassador and inducted in Hall of Fame at TSEC as an appreciation to consistent academic performance, sincerity, and discipline in 2015.
- Awarded a four-week fellowship course at Goethe Institut, Duesseldorf in January 2015 by Goethe Institut, Mumbai for fluency in German language.
- Awarded Sir Ratan Tata scholarship in 2015, worth INR 59700, for academic excellence in academic year 2013-14.

Volunteering experience

- Co-organized poster sessions at the annual composites symposium, jointly held by ICRC, Canada and IRTG, Germany in May 2021 virtually in London Ontario. Approximately 65 researchers from composite research groups from Ontario and Quebec in Canada and Baden-Wuerttemberg in Germany were in attendance. 24 researchers presented their work in four poster sessions.
- Co-founded "Chinese corner", a Mandarin speaking club, together with Chinese Student Association at Rotterdam University. I was in-charge on conducting monthly meetings, each of which had about 10 participants (native Chinese and learners of Mandarin language), from November 2016 to April 2017.

Languages

- Marathi Mothers tongue
- Hindi Advanced
- English Advanced
- German Advanced (**Certifications:** GZC1, ZDfB)
- Mandarin Intermediate (Pursuing HSK5)
- Dutch Intermediate
- Sanskrit Basic

Other interests

- Learning languages
- Aviation enthusiast
- Molecular gastronomy